

AN INVESTIGATION OF THE STRENGTH
OF CONCRETE MASONRY SHEAR WALL STRUCTURES

By

KRISHNAIYER BALACHANDRAN

A DISSERTATION PRESENTED TO THE GRADUATE COUNCIL OF
THE UNIVERSITY OF FLORIDA
IN PARTIAL FULFILLMENT OF THE REQUIREMENTS FOR THE
DEGREE OF DOCTOR OF PHILOSOPHY

UNIVERSITY OF FLORIDA

1974

To my parents

ACKNOWLEDGMENTS

The author wishes to express his sincere gratitude to Dr. M. W. Self for his patience, guidance, and encouragement, without which this dissertation would not have been possible.

Special thanks are due to Prof. Herbert A. Sawyer, Jr., for sparing some of his equipment and literature and, also, for serving on the supervisory committee. Appreciation is extended to Dr. C. S. Hartley for serving on his supervisory committee.

Sincere thanks are due to Dr. Martin A. Eisenberg for the help he has provided in introducing the author to the Finite Element Method. Without his professional guidance, helpful suggestions and long hours of discussion, the author's task would have been more difficult.

The author wishes to express his gratitude to all those who assisted him along the way: Graduate students K. Fuller and M. Chanchalani; and friends M. Krishnamurthy, S. M. Ulagaraj, J. N. Sharma, A. M. Garde and H. A. Cole, Jr.

Thanks are due to Mr. L. F. Hopkins and W. Whitehead for their help on the equipment in the Civil Engineering Laboratory.

Acknowledgment is due to the Concrete Promotion Council of Florida for their financial support for part of the experimental program; to the National Concrete Masonry Association and the National Bureau of Standards for providing the model concrete blocks; and, to the Northeast Regional Data Center for its support.

Special thanks go to Mrs. C. Combs for her concerned work when typing the final copy.

Finally, a special note of deep appreciation is due to his wife, Lalitha, for her encouragement, love and understanding during the difficult time of being the wife of a student.

TABLE OF CONTENTS

	Page
ACKNOWLEDGMENTS.....	iii
LIST OF TABLES.....	viii
LIST OF FIGURES.....	ix
KEY TO SYMBOLS.....	xv
ABSTRACT.....	xxi
 CHAPTER	
1. INTRODUCTION.....	1
1.1 History.....	1
1.2 General Remarks.....	2
1.3 Previous Investigations.....	6
1.3.1 Strength of Mortar Joints.....	6
1.3.2 Racking Tests.....	10
1.3.3 Circular Shear Specimens.....	12
1.3.4 Square Shear Specimens.....	13
1.3.5 Horizontally and Vertically Loaded Wall Without Frame.....	16
1.3.6 Test on Small Masonry Assemblages.	17
1.3.7 Reinforced Concrete Masonry Walls in Shear.....	20
1.3.8 Effect of Wall Openings.....	22
1.3.9 Shear in Concrete Masonry Piers...	25
1.3.10 Strength of Masonry under Combined Compression and Shear..	30
1.4 Objectives and Scope of Present Investigation.....	33
2. EQUIPMENT, MATERIALS AND TESTING TECHNIQUES....	35
2.1 Testing Machines and Other Equipment.....	35
2.2 Concrete Blocks.....	36
2.3 Mortar.....	39
2.4 Model Concrete Blocks.....	41
2.5 Model Reinforcement.....	43
2.6 Model Mortar.....	43
2.7 Model Grout Mixes.....	46
2.8 Mortar Mix for Spandrel.....	51

Table of Contents (Continued)

CHAPTER	Page
3. STRENGTH OF MORTAR JOINTS UNDER COMBINED STRESSES.....	52
3.1 Scope.....	52
3.2 Test Specimens.....	53
3.3 Strength of Mortar Joints under Compression and Shear.....	53
3.4 Strength of Mortar Joints under Compression and Bending.....	63
3.5 Combined Compression, Bending, and Shear..	69
4. MODEL TESTS OF CONCRETE MASONRY PIERS.....	70
4.1 Selection of Model.....	70
4.2 Selection of Model Materials.....	83
4.3 Fabrication of Model.....	86
4.4 Test Setup.....	89
4.5 Test Parameters.....	91
4.6 Tests on Grouted Piers.....	91
4.7 Tests on Nongrouted Piers.....	101
5. ANALYSIS OF TEST RESULTS.....	102
5.1 Grouted Piers.....	102
5.2 Nongrouted Piers.....	105
5.3 Equations for Predicting the Diagonal Tensile Strength of Masonry.....	108
5.3.1 Grouted Piers.....	108
5.3.2 Nongrouted Piers.....	111
6. NONLINEAR FINITE ELEMENT ANALYSIS.....	122
6.1 General Remarks.....	122
6.2 Finite Element Linear Analysis.....	123
6.3 Finite Element Nonlinear Analysis.....	125
6.3.1 General Remarks.....	125
6.3.2 General Physical Approach.....	126
6.4 Variable Stiffness Methods.....	127
6.5 Initial Stress Method.....	130
6.6 Initial Strain Method.....	131
6.7 Previous Investigations.....	132
6.8 Objective and Scope of Present Investigation.....	138
7. DESCRIPTION OF ANALYTICAL MODEL.....	139
7.1 Choice of Finite Elements.....	139
7.2 Formulation of Element Stiffness Matrix...	142

Table of Contents (Continued)

CHAPTER	Page
7. Description of Analytical Model (Continued)....	
7.3 Material Properties and Failure Criteria..	147
7.3.1 Uniaxial Stress-Strain Curves.....	147
7.3.2 Representation of Properties of Masonry Element.....	147
7.3.3 Plastic Yielding in Compression....	152
7.3.4 Biaxial Strength of a Masonry Component.....	153
7.3.5 Crushing of Masonry.....	155
7.3.6 Cracking.....	155
7.3.7 Bond Failure at the Interface between Mortar and Block.....	159
7.3.8 Yielding of Reinforcement.....	164
8. ANALYSIS AND EXAMPLES.....	165
8.1 Method of Solution.....	165
8.2 Computational Procedure.....	167
8.3 Computer Program.....	172
8.4 Examples of Nonlinear Analysis.....	175
8.4.1 Square Concrete Panel under Diagonal Compression.....	175
8.4.2 Hollow Concrete Masonry Panels under Diagonal Compression.....	182
8.4.3 Grouted Masonry Piers.....	188
8.4.4 Nongrouted Masonry Piers.....	198
9. CONCLUSIONS.....	203
9.1 Conclusions.....	203
9.2 Recommendations for Further Study.....	207
APPENDIX A (ALGORITHM FOR SOLUTION OF EQUATIONS).....	208
APPENDIX B (COMPUTER PROGRAM OUTPUT).....	213
REFERENCES.....	221
BIOGRAPHICAL SKETCH.....	227

LIST OF TABLES

TABLE	Page
2.1 PROPERTIES OF MODEL MORTAR AND GROUT.....	48
3.1 PROPERTIES OF MORTAR.....	54
3.2 STRENGTH OF MORTAR JOINTS UNDER COMPRESSION AND SHEAR.....	58
3.3 STRENGTH OF 1:1:4.5 MORTAR JOINTS UNDER COMPRESSION AND SHEAR.....	59
3.4 STRENGTH OF MORTAR JOINTS UNDER COMPRESSION AND BENDING.....	62
3.5 MORTAR JOINTS UNDER COMBINED COMPRESSION, BENDING, AND SHEAR.....	67
5.1 TEST RESULTS OF GROUTED PIERS.....	103
5.2 TEST RESULTS OF NONGROUTED PIERS.....	109
5.3 ANALYSIS OF RESULTS OF TESTS ON NONGROUTED PIERS.....	115
8.1 MATERIAL PROPERTIES USED IN ANALYSIS OF PR 3....	190
8.2 MATERIAL PROPERTIES USED IN ANALYSIS OF PR 7....	195
8.3 MATERIAL PROPERTIES USED IN ANALYSIS OF PR 9....	197

LIST OF FIGURES

FIGURE	Page
1.1 Shear wall with boundary elements.....	5
1.2 Elements of shear wall with openings.....	5
1.3 Type of test specimens used by Zelger.....	8
1.4 Test specimen adopted by Haller.....	8
1.5 Arrangement of racking test and the force distribution on the specimen.....	11
1.6 Test for diagonal tensile strength of brickwork and stress distribution.....	11
1.7 Typical X-cracks in a wall damaged by an earthquake.....	14
1.8 Fringe patterns obtained in a photoelastic analysis of a model of a wall with an opening and a square panel under diagonal compression.....	14
1.9 Diagonal tension test on a square panel.....	15
1.10 Test setup (schematic) adopted by Meli and Reyes for testing mortar joints under compression and shear.....	15
1.11 Types of test specimens adopted by Meli and Reyes for diagonal compression tests.....	19
1.12 Test panels adopted by Converse.....	19
1.13 Continuous opening in a shear wall.....	23
1.14 Staggered opening in a shear wall.....	23
1.15 Forces acting on a pier element in a wall with opening.....	26
1.16 Test setup adopted by Schneider for full scale test on piers.....	26

List of Figures (Continued)

FIGURE	Page
2.1 Splitting tests on concrete block.....	38
2.2 Sieve analysis of sand for masonry mortar.....	40
2.3 Model concrete block.....	42
2.4 Model reinforcement (0.147" dia.).....	42
2.5 Stress-strain curve for model concrete block...	44
2.6 Stress-strain curve for model reinforcement....	45
2.7 Stress-strain curve for model mortar.....	47
2.8 Stress-strain curve for model grout.....	49
2.9 Stress-strain curve for spandrel mortar.....	50
3.1 Setup for studying the strength of mortar under pure shear.....	55
3.2 Test setup for finding the strength of mortar joints under combined compression and shear..	56
3.3 Shear failure through mortar joint.....	56
3.4 Effect of precompression on the shearing strength of mortar joints.....	60
3.5 Cross-section of a mortar joint.....	64
3.6 Effect of precompression on the flexural tensile strength of mortar joints.....	65
3.7 Test setups used for obtaining combined stresses on mortar joints.....	66
3.8 Interaction of bending and shear under constant precompression.....	68
4.1 Photoelastic model configurations chosen by Schneider.....	71
4.2 Finite element idealization for a shear wall with openings.....	73

List of Figures (Continued)

FIGURE		Page
4.3	Finite element idealization for a multiple pier shear wall.....	74
4.4	Finite element idealization for a pier with openings and walls on either side..	75
4.5	Finite element idealization for the test specimen adopted by Schneider.....	76
4.6	Isoshear lines for the pier shaded as shown above.....	77
4.7	Isoshear lines for the pier shaded as shown above.....	78
4.8	Isoshear lines for the pier shaded as shown above.....	79
4.9	Isoshear lines for the pier shaded as shown above.....	80
4.10	Isoshear lines for the pier shaded as shown above.....	81
4.11	Isoshear lines for the pier shaded as shown above.....	82
4.12	Schematic test setup for finding the shearing strength of a pier.....	84
4.13	Details of pier model.....	88
4.14	Model test on pier.....	90
4.15	Failure pattern of PR 4 strong mortar, weak grout.....	92
4.16	Failure pattern of PR 3 strong mortar, medium grout.....	92
4.17	Failure pattern of PR 5 strong mortar, strong grout.....	93
4.18	Failure pattern of PR 9 weak mortar, weak grout.....	93
4.19	Failure pattern of PR 10 weak mortar, medium grout.....	94

List of Figures (Continued)

FIGURE	Page
4.20 Failure pattern of PR 7 weak mortar, strong grout.....	94
4.21 Typical load-deflection curves for grouted piers.....	95
4.22 Failure pattern of PR 13 weak mortar, precompression 50 psi.....	96
4.23 Failure pattern of PR 23 weak mortar, precompression 125 psi.....	96
4.24 Failure pattern of PR 17 weak mortar, precompression 200 psi.....	97
4.25 Failure pattern of PR 19 strong mortar, precompression 50 psi.....	97
4.26 Failure pattern of PR 21 strong mortar, precompression 125 psi.....	98
4.27 Failure pattern of PR 20 strong mortar, precompression 200 psi.....	98
4.28 Failure pattern of hollow pier PR 1 (strong mortar).....	99
4.29 Failure pattern of hollow pier PR 6 (weak mortar).....	100
5.1 Relation between average shear stress and square root of prism strength for grouted piers.....	104
5.2 Comparison of results of grouted piers with corresponding prism strengths.....	106
5.3 Area used to compute shear stress for hollow piers.....	107
5.4 Effect of precompression on shearing strength of nongrouted piers.....	110
5.5 Idealization for a pier loaded in diagonal compression.....	112
5.6 Test results of nongrouted pier specimens.....	113
5.7 Failure pattern of hollow square panel subject to diagonal compression.....	118

List of Figures (Continued)

FIGURE	Page
5.8 Assumed state of stress at the center of pier.....	119
6.1 Effect of nonlinear material properties.....	128
6.2 Iterative solution techniques for nonlinear analysis.....	128
6.3 Material idealization and selected results of analysis of RC panels by Cervenka and Gerstle.....	133
6.4 Failure envelope adopted by Franklin.....	135
6.5 Schematic diagram to illustrate crack propagation (initial stress method using variable stiffness within an increment).....	137
6.6 Schematic diagram to illustrate crack propagation (initial stress method using constant stiffness within an increment).....	137
7.1 Solution of a cantilever beam by elements with varying degrees of freedom.....	141
7.2 Quadratic rectangular element.....	141
7.3 Uniaxial stress-strain curves.....	148
7.4 Components of a reinforced grouted element.....	150
7.5 Rotation of coordinates.....	150
7.6 Liu's failure envelope for concrete under biaxial compression.....	154
7.7 Assumed failure envelope for block, mortar, and grout.....	154
7.8 Cracking at an integration point.....	157
7.9 Bond strength criterion.....	157
7.10 Normal stresses acting on interface of inclined mortar joints.....	162
8.1 Schematic diagram illustrating the nonlinear analysis adopted.....	166

List of Figures (Continued)

FIGURE	Page
8.2 General flow chart of the program.....	173
8.3 Flow diagram for the failure criteria.....	174
8.4 Crack pattern of square concrete panel at 195,000 lbs.....	176
8.5 Crack pattern of square concrete panel at 196,000 lbs.....	178
8.6 Crack pattern of square concrete panel at 197,000 lbs.....	179
8.7 Crack pattern of square concrete panel at 198,000 lbs.....	180
8.8 Crack pattern of square concrete panel at 199,000 lbs.....	181
8.9 Experimentally observed failure modes in hollow concrete masonry panels.....	183
8.10 Predicted failure pattern for panel SM.....	184
8.11 Predicted failure pattern for panel MS.....	186
8.12 Predicted failure pattern for panel MW.....	187
8.13 Finite element idealization for pier PR 3.....	189
8.14 Predicted crack pattern for PR 3.....	192
8.15 Analytical and experimental load-deflection curves for grouted piers.....	193
8.16 Predicted failure pattern for PR 7.....	196
8.17 Predicted failure pattern for PR 9.....	199
8.18 Predicted failure pattern for PR 6.....	200
8.19 Predicted failure pattern for PR 19.....	201
B.1 Finite element idealization for panel SM.....	215

KEY TO SYMBOLS

- A sectional area of split in the indirect tension test on concrete block; area of cross-section of pier.
- A_B cross-sectional area of block.
- A_G area of cross-section of grout.
- A_S area of cross-section of steel reinforcement.
- a distance from the point of inflection to the spandrel restraint; length of a grouted finite element.
- a_j location of integration point 'j' in the Gauss quadrature formula.
- {B} matrix relating element strains to nodal displacements.
- {B₁} matrix of stiffness coefficients which relates the unknown displacements in column 1 with those of column 2.
- C initial bond strength between brick and mortar.
- {C₁} matrix of stiffness coefficients which relates the the unknown displacements in column 1 with those of column 3.
- c adhesion between mortar and block.
- D diameter of specimen; overall pier depth.
- [D₁] square matrix of stiffness coefficients which relates the unknown displacements of column 1 among themselves.
- [D_{cb}] global constitutive matrix at the point of occurrence of compression-shear debonding.
- [D_{cb0}] local constitutive matrix at the point of occurrence of compression-shear debonding.

Key to Symbols (Continued)

$[D_{cr}]$	rigidity matrix for cracked point in the global frame of reference.
$[D_{cro}]$	material stiffness matrix for cracked component in the local principal coordinate system.
$[D_{ep}]$	elasto-plastic matrix.
$[D_{tb}]$	global constitutive matrix at the point of occurrence of shear-tension debonding.
d	width of specimen.
E	Young's modulus of steel reinforcement.
E_B	initial tangent modulus of elasticity of block.
E_G	initial tangent modulus of elasticity of grout.
E_S	Young's modulus of steel reinforcement.
E_{eq}	equivalent modulus of elasticity of a composite element.
F	applied load; plasticity factor.
$\{F\}$	element nodal forces.
$\{F_1\}$	RHS vectors for unknowns in column 1.
f	material stresses; function of stress and strain.
f_a	external precompression on mortar joints, psi.
f_b	bending stress on a mortar joint in a state of combined compression, bending, and shear, psi.
f_{bo}	modulus of rupture of mortar joint, psi.
f_c'	ultimate uniaxial compressive strength of concrete.
f_{dt}	diagonal tensile strength of masonry.
f_m'	prism strength.
f_{max}	maximum principal stress.
f_n	normal stress on a cross-section.

Key to Symbols (Continued)

f_{pr}	external precompressive stress on a pier.
f_s	average shear stress on a cross-section.
f_{so}	apparent shear strength of mortar joint under combined compression and shear, psi.
f_t	tensile strength of a material.
f_y	precompression applied to brickwork.
f_{y1}	
f_{y2}	
H	horizontal component of the ultimate load on pier.
H_i	weighting coefficients adopted in the Gauss quadrature formula.
h	height of a specimen.
$[J]$	Jacobian matrix used for obtaining strain transformation matrix for an isoparametric element.
K_1, K_2	structure stiffnesses.
$[K]$	global stiffness matrix.
$[k]$	element stiffness matrix.
l	length of a specimen.
M	spandrel moment.
$\{N\}$	interpolation functions.
n	number of integration points used in the Gauss quadrature formula.
P	applied load on a specimen.
P_u	ultimate load on a specimen.
$\{p\}$	matrix of body forces in an element.
$\{Q\}$	matrix of equivalent nodal forces corresponding to "initial stresses".

Key to Symbols (Continued)

$\{R\}$	external nodal point forces.
R_i	total applied load during 'i'th load increment.
S	elastic section modulus.
T	applied horizontal load in racking test.
$\{T_e\}$	strain transformation matrix.
$\{T_o\}$	stress transformation matrix.
t	thickness of a specimen; net thickness of a wall.
U_i	component of nodal force in the direction of 'u' displacement.
$\{u\}$	matrix of displacements in the x-direction.
V	base shear; vertical component of applied load.
V_i	component of nodal force in the direction of 'v' displacement.
V_{PI}	load shared by pipe columns.
v_m'	shear strength of masonry.
v_u	ultimate shear strength.
w	unit weight of concrete, pcf.
X	component of body force in an element in the x-direction.
X_1	horizontal distance from center of pier to point of application of load.
$\{X_1\}$	number of unknowns in column 1.
X_n	x-coordinate of node 'n' of an element.
x	x-coordinate of any point in an element.
Y	component of body force in an element in the y-direction.
y	vertical distance of a cross-section of pier from the point of application of load; y-coordinate of any point in an element.

Key to Symbols (Continued)

α	ratio of principal stress in orthogonal direction to principal stress in direction considered; direction of maximum principal stress at an integration point; inclination of mortar joints to global frame of reference.
β	shear retention factor.
γ	shear strain.
$\{\Delta R\}$	unbalanced nodal forces
$\{\Delta \sigma_i\}$	incremental nodal displacements at node 'i'.
$\{\Delta \epsilon'\}$	incremental strains.
$\{\Delta \epsilon\}$	elastic incremental strains in the "initial stress" method.
$\{\Delta \sigma'\}$	incremental stresses; true increment of stress possible for the given strain in the "initial stress" method.
$\{\Delta \sigma\}$	elastic incremental stresses in the "initial stress" method.
$\{\Delta \sigma''\}$	initial stresses to be supported by equivalent nodal forces
$\{\delta\}$	nodal displacements.
ϵ	uniaxial strain.
$\{\epsilon\}$	vector of strains at a point.
ϵ_{cu}	ultimate uniaxial compressive strain of a material.
$\{\epsilon_0\}$	vector of initial strains.
η_i	local y-coordinate of node 'i'.
μ	coefficient of friction between brick (block) and mortar.
ν	Poisson's ratio of a material.
ξ_i	local x-coordinate of node 'i'.
σ	uniaxial stress at a point.

Key to Symbols (Continued)

- $\{s\}$ vector of stresses at a point.
- $\bar{\sigma}, \sigma_y$ uniaxial yield stress.
- σ_n normal stress at interface between block and mortar.
- σ_o ultimate strength of concrete plate in uniaxial compression, psi.
- $\{\sigma_o\}$ vector of residual stresses.
- σ_p peak stress in biaxial compression, psi.
- σ_t tensile strength of a material.
- ζ shear stress; shear stress at the interface between block and mortar.
- ζ_{lim} limiting bond shear strength of mortar.

Abstract of Dissertation Presented to the Graduate Council
of the University of Florida in Partial Fulfillment of the
Requirements for the Degree of Doctor of Philosophy

AN INVESTIGATION OF THE STRENGTH
OF CONCRETE MASONRY SHEAR WALL STRUCTURES

By

Krishnaiyer Balachandran

August, 1974

Chairman: Dr. Morris W. Self

Major Department: Civil Engineering

The main objective of this investigation is to obtain empirical equations to predict the shear capacity of nonreinforced concrete masonry elements. An analytical investigation using a nonlinear finite element analysis and an experimental investigation were carried out for this purpose.

First, an experimental program was initiated to obtain equations for predicting the strength of mortar joints under combined compression, shear, and bending. The test specimens were standard three-block prisms with three-eighths-inch mortar joints. Precompression up to 300 psi was applied. Based on test results, a circular interaction curve is proposed for predicting the strength of mortar joints under combined stresses.

In the second phase of the experimental program, the shear strength of concrete masonry piers made with one-fourth-scale model blocks was investigated. The main variables were the strengths of grout and mortar and the magnitude of external precompression. A relationship between the shearing strength of a grouted pier and the corresponding prism strength was established. Equations are proposed for predicting the shearing strength of a nongrouted concrete masonry pier.

A nonlinear finite element analysis, using the isoparametric approach and higher order rectangular elements, was developed to predict the behavior and collapse of concrete masonry elements. An incremental loading procedure was adopted and failure was investigated at integration points due to yielding, cracking, or crushing of the masonry component. Also, criteria were developed to predict the debonding of the mortar joints. The "initial stress" approach was adopted to redistribute the released stresses, due to cracking, to the surrounding elements. The initial stiffness was used throughout each iterative cycle as well as through all the load increments. Predictions of failure patterns, collapse load, and deformations are compared to experimental results.

CHAPTER 1

INTRODUCTION

1.1 History: Masonry construction is perhaps the oldest building system employed by man as evidenced by the historic remains of ancient temples in India and Egypt. These early works evolved more from art than science and are characterized by their massiveness and quality craftsmanship. This traditional masonry construction prevailed throughout the United States in the nineteenth century and was culminated by the construction of the Monadnock Building in Chicago, Illinois, completed in 1891. This 16-story skyscraper has exterior bearing walls varying in thickness from 12 inches at the top story to 6 feet at the base.

Late in the nineteenth century, the concept of the structural frame in structural steel or reinforced concrete replaced masonry bearing wall construction. Masonry became primarily an architectural product used in nonbearing partitions and as a facing.

Expanded research in building methods and materials early in the twentieth century, particularly with respect to structural concrete, has resulted in renewed interest in load-bearing masonry. Although a considerable amount of masonry research has occurred since 1932 (43), there

exists little correlation among the various studies conducted by governmental, promotional, and university research agencies. Each study has of economic necessity been constrained within narrow bounds placed on the variables. For this reason, recommendations based upon this research have been purposely conservative. Much reliance has been placed upon the results of the voluminous research and experience with concrete and reinforced concrete; and research, design, and construction procedures for reinforced masonry have advantageously followed those developed for reinforced concrete. However, there are important differences in the behavior of masonry and concrete that must be taken into consideration.

1.2 General Remarks: Concrete masonry walls are broadly classified as either load-bearing or nonload-bearing and further described in various ways such as either nonreinforced, solid unit, or hollow unit.

The general behavior of high-rise, load-bearing structures under gravity and lateral loads is the combined action of floors, bearing walls, and shear walls. Floors transmit horizontal forces by diaphragm action from the exterior walls to the shear walls, which in most cases are also the bearing walls. The floor system must be sufficiently rigid to serve as a diaphragm, and connections must be adequate to transfer these forces to the shear walls which carry them to the foundation. The height to which the buildings can be

constructed depends upon the strength of the masonry materials, the spacing of intersecting walls and floors, their connection to each other, and the shape of the structure.

The design procedure includes an investigation of the following (41)(20).

1) Bearing capacity: bearing stresses will generally govern required block strength and wall thicknesses.

2) Stability against overturning: overturning resistance to lateral loads depends upon the shape and mass of the building. Shear walls that are also load-bearing walls are the most effective structural elements for developing resistance to overturning.

3) Shear resistance of walls: lateral load is transmitted through the floors to those shear walls parallel to the assumed direction of the lateral load. The percentage of total lateral load carried by a shear wall is proportional to this "relative rigidity" with respect to other participating shear walls.

4) Flexural resistance of walls: lateral bending of walls can be produced by wind loads on exterior walls, by eccentricity of loading, and by insufficiently rigid floor diaphragms and shear walls.

5) Floor-wall connections: finally, because the strength and stability of the high-rise building depend upon the interaction of the connecting floor and wall elements, connections must be adequate.

As mentioned previously, shear walls are designed to resist the effects of lateral forces acting on buildings. The lateral forces are primarily due to wind or earthquake. The performance requirements for shear walls under wind loads are different than that for earthquakes (3). Walls designed for wind forces have to meet both strength and stiffness requirements. Walls designed for earthquakes must also satisfy requirements of ductility and energy absorption, damping characteristics and damage control, during several cycles of inelastic deformation (1).

The behavior of shear walls is complicated by the influence of boundary elements and multiple openings (14) (36). Figures 1.1 and 1.2 [taken from reference (3)] present some typical examples. Lateral loads are usually introduced into shear walls through floor slabs framing into either one side or both sides of the walls. As a result, the lateral loads tend to be distributed across the width of the wall. Transverse walls or columns are often located at the extreme edges of the walls. They act with the wall, and usually contain most of the flexural reinforcement resisting the moment due to the lateral forces.

When a wall contains large openings, it can be considered to be made up of a system of piers and spandrels. Each individual pier or spandrel is, in effect, a shear wall element, with a shear span approximately equal to one-half of its height or length, respectively. In addition to shear,

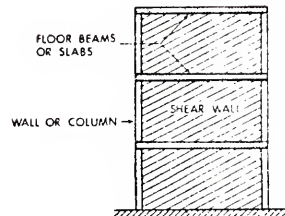


Fig. 1.1. Shear wall with boundary elements.

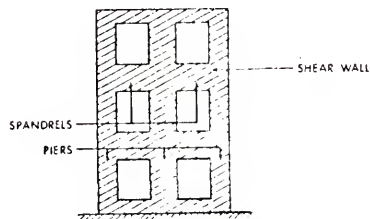


Fig. 1.2. Elements of shear wall with openings.

piers will also generally have tension or compression caused by gravity and overturning forces as well as shrinkage, creep, and differential settlement.

It is noted by the Joint ASCE-ACI Task Committee 426 on Shear and Diagonal Tension that the shear strength of a wall is of interest only for shear span to depth ratios less than 2, or for walls with a flanged cross-section (3).

1.3 Previous Investigations:

1.3.1 Strength of Mortar Joints: compared with the vast number of tests reported on concentrically loaded walls with the load applied vertically, little is known about the strength of masonry walls with the load applied at different inclinations to the horizontal joints. However, some test results are reported. Benjamin and Williams (5) carried out tests on shear couplets of two bricks bound together with a mortar joint. Three different mortar types were tested with watered, stiff mud, side-cut, vacuum-treated clay bricks. The test results showed little or no influence of brick and mortar compressive strengths on the couplet bond strengths in tension and shear. The test results showed that the relationship between the shear stress, f_s (shear force divided by wall area), and the normal stress, f_n , could be expressed in the form:

$$f_s = C + \mu f_n \quad (1.1)$$

where μ is the coefficient of friction between mortar and brick and C is the initial bond strength, a constant. Benjamin and Williams obtained a value of $C = 150$ psi and $\mu = 0.73$. They also concluded that, up to a compressive stress of approximately 650 psi, the shear strength increases with the compressive stress. For higher compressive stresses, the apparent shear stress still increases, although the joint has already failed in shear. The additional strength is claimed to be due to friction.

Zelger (44) has reported tests on masonry specimens of the type shown in Figure 1.3. Zelger obtained $C = 2$ kg/sq cm and $\mu = 0.5$ in his tests. Yorulmaz and Sozen (44) tested masonry specimens of model bricks 0.53" x 0.86" x 1.87" in size. The results obtained from test specimens of the type in Figure 1.3 gave $C = 150$ psi and $\mu = 0.46$.

Haller (22) adopting the test setup shown in Figure 1.4, arrived at the following empirical relationships:

$$f_s = 35\sqrt{f_n} + 280 - 540 \text{ psi} \quad (1.2)$$

$$f_n \leq 200 \text{ psi}$$

for normal quality masonry consisting of cored bricks (3300 psi to 6500 psi) and cement-lime-sand mortar (1225 psi).

If the Haller formula is approximated to linear relationship, the following equation is obtained:

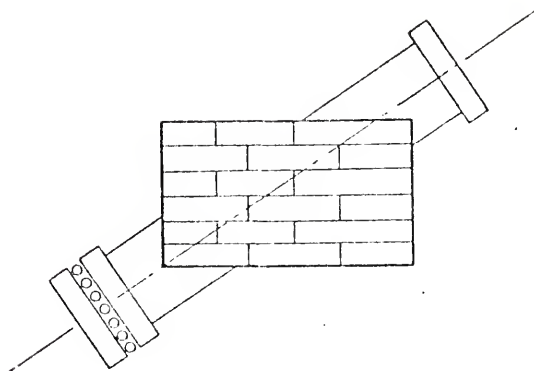


Fig. 1.3. Type of test specimens used by Zelger.

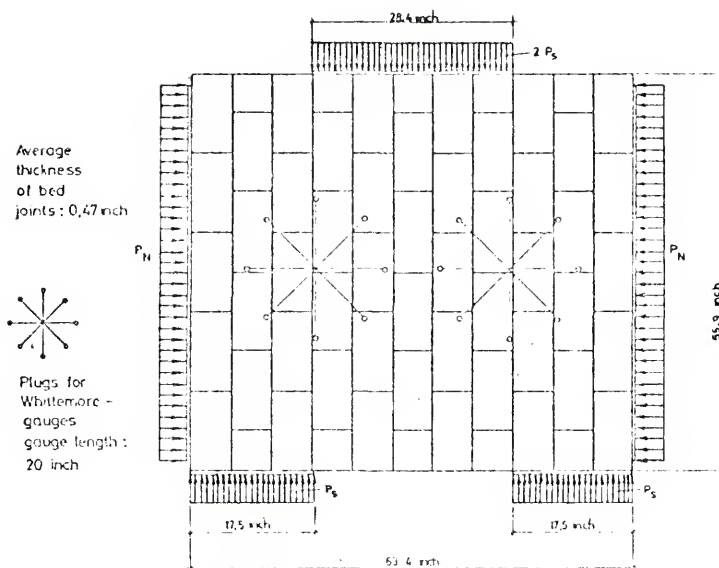


Fig. 1.4. Test specimen adopted by Haller.

$$f_s = 50 + 0.88 f_n \quad (1.3)$$

$$f_n \leq 200 \text{ psi}$$

The tests of the type shown in Figure 1.3 give the most representative values for shear strengths of the mortar joints in masonry, since disturbances caused by the testing machine platens, etc., are much less likely to occur in this type of test compared with the couplet type tests.

From the limited number of tests mentioned, it seems reasonable to assume that the bond or shear failure of a mortar joint in brick masonry follows Equation (1.1) in a range of approximately 2% to 15% of the compressive strength of the masonry. C is of the order of 2% to 3% of the compressive strength of masonry. However, since the couplet tests indicate that the compressive strength of the mortar has no influence on the bond strength, the shear strength should be tested when high stresses are employed.

For compressive stresses lower than approximately 2% of the compressive strength of the masonry, and for pure tensile stresses, the shear strength falls below that calculated from Equation (1.1), as revealed by couplet tests and model masonry tests. The pure tensile bond strength is greatly influenced by workmanship and wetness of the bricks. A suction rate of 20 g/min or less seems to give maximum bond, although saturated bricks produce close to maximum bond.

For high compressive stresses, the apparent shear strength again is lower than calculated from Equation (1.1).

Hedstrom (24) reports load tests of concrete masonry walls with constant wall dimensions but with mortar bed joints in 90°, 45°, and 0° inclination to the axial load, which was applied parallel to the longer side of the walls. The tensile bond strength obtained with the two types of mortar was tested on masonry prisms of two blocks in bending. A plot of bond shear strength vs. compressive strength yielded $C = 48.5$ psi and $\mu = 0.84$ for M-type mortar and $C = 24$ psi and $\mu = 0.92$ for S-type mortar. The figures are supported by too few tests to be conclusive.

1.3.2 Racking Tests: the present standard racking test described in ASTM E 72-68, Method of Conducting Strength Tests of Panels for Building Construction, provides only a relative measure of the shearing or diagonal tensile resistance of a wall. Results of this test are consequently valid only for comparison purposes and are not suggested for determination of design values.

In this method of test (Figure 1.5), horizontal movement of the wall specimen (8' x 8'), due to the horizontal racking load at the top of one end, is prevented by a stop block at the bottom of the other end. To counteract rotation of the specimen due to this overturning couple, tie rods are used near the loaded edge of the wall specimen. Under racking load these rods superimpose an indeterminate

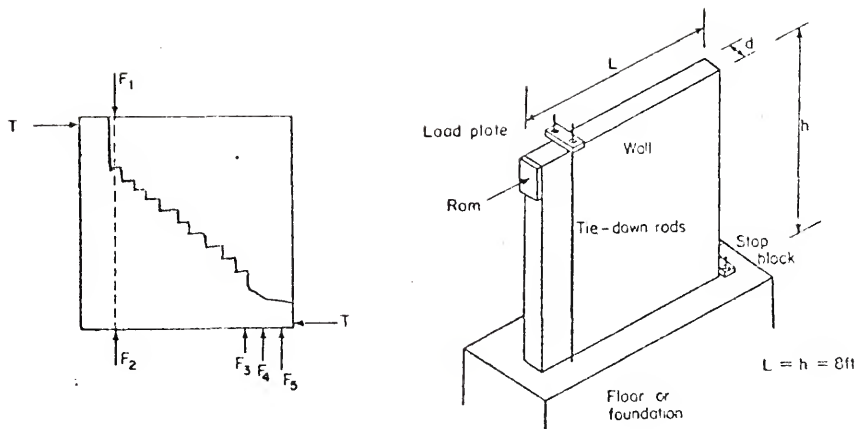


Fig. 1.5. Arrangement of racking test and the force distribution on the specimen.

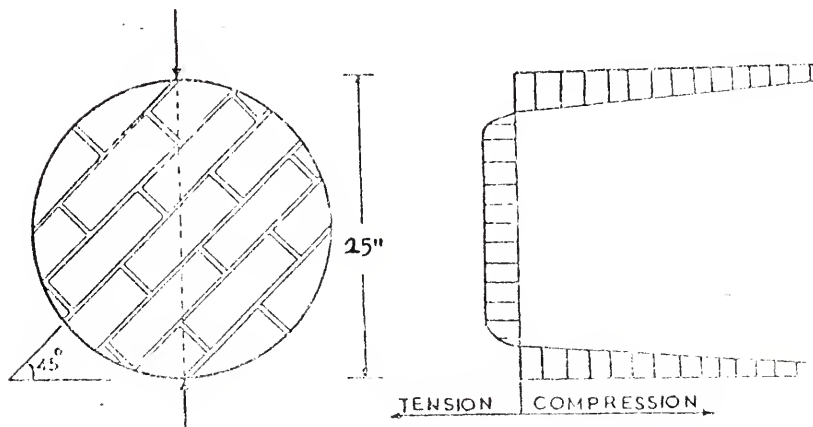


Fig. 1.6. Test for diagonal tensile strength of brickwork and stress distribution.

compressive force which suppresses the critical diagonal tensile stresses and increases the load required to rack the specimen. A typical mode of failure is indicated. The obtained apparent shear strength as calculated from $f_s = T/ld$ is usually of the order of 25 psi to 300 psi under laboratory conditions.

For concrete masonry walls, the racking strength was reported by Fishburn (18) to be 25 psi to 50 psi for masonry walls having a compressive strength of 390 psi to 470 psi giving a racking strength of about 7% to 10% of compressive strength.

1.3.3 Circular Shear Specimens (28): in these tests (Figure 1.6), a 15" diameter specimen is tested in compression with the line of load at 45° to the bed joints. As shown in Figure 1.6, the diametrical stresses are largely tensile over the central 80% of the specimen. The tensile stress is approximately constant for about 60% of the diameter and may be calculated by the following equation:

$$f_t = \frac{2P}{\pi Dt} \quad (1.4)$$

where P equals load at rupture, in pounds, D equals the diameter of the specimen, in inches, and t equals the thickness of the specimen, in inches.

1.3.4 Square Shear Specimens (6)(16): in examining the damage done during earthquakes, it was noted that cracks in shear walls were frequently of a diagonal nature, so frequently that they were called typical "X cracks" (Figure 1.7). With this as a starting point, the theory was early recognized that the force of quake working against the static resistance of a building would produce a racking effect; this in turn would be resisted by the diagonal strength of the wall member. It was found that the "X" cracking developed in a diagonal tension test.

Photoelastic analysis through the use of polarized stress panels was used to demonstrate the validity of this theory (Figure 1.8). The stress distribution in the wall panel was shown to be the same as in the diagonal test panel. It was then decided that the proper test would consist of breaking, by diagonal loading, 4' x 4' panels incorporating desired variables (Figure 1.9). In this method, the test results are susceptible to stress analysis. In addition, they are more reproducible and thus more reliable for comparison and design data purposes.

The square specimen is placed in the testing frame so as to be loaded in compression along a diagonal, thus producing a diagonal tension failure with the specimen splitting apart along the loaded diagonal. The shear strength,

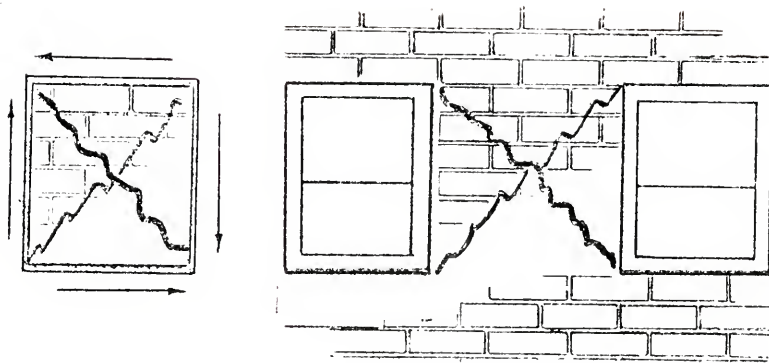


Fig. 1.7. Typical X-cracks in a wall damaged by an earthquake.

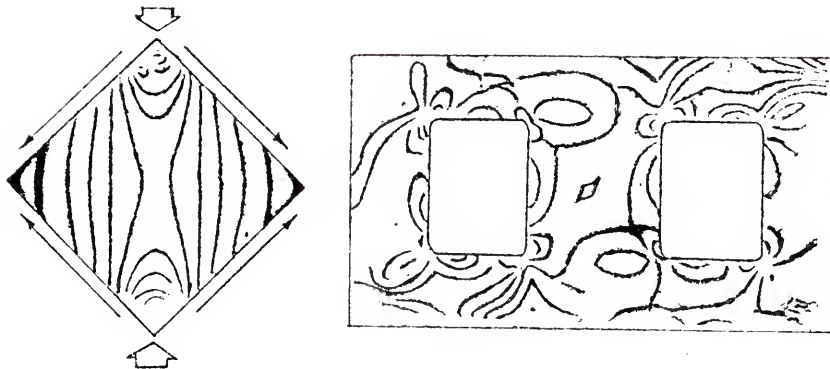


Fig. 1.8. Fringe patterns obtained in a photoelastic analysis of a model of a wall with an opening and a square panel under diagonal compression.

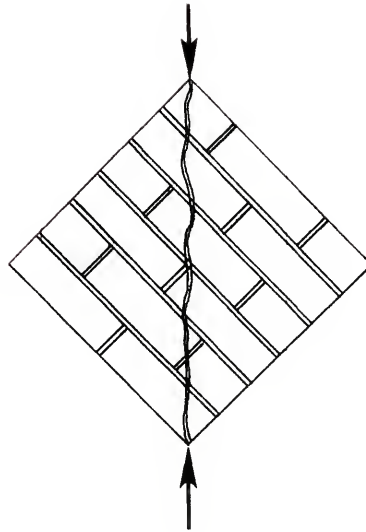


Fig. 1.9. Diagonal tension test on a square panel.

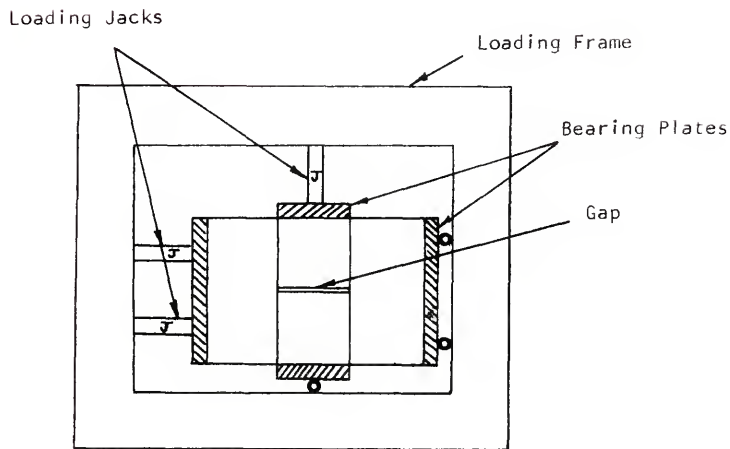


Fig. 1.10. Test setup (schematic) adopted by Meli and Reyes for testing mortar joints under compression and shear.

v_m' , is determined from the equation (6) (27):

$$v_m' = \frac{0.707 F}{tl} \quad (1.5)$$

where F equals the diagonal compressive force or load, in pounds, t equals the thickness of wall specimen, in inches, and l equals the length of a side of a square specimen, in inches.

1.3.5 Horizontally and Vertically Loaded Wall Without Frame: the load carrying capacity of a wall subjected to a horizontal load at one of the upper corners is governed mainly by the shear and tensile strength of the bedjoints at the foundation of the wall (44). By precompression, for example, by dead load from slabs and walls above, the strength is increased in a manner similar to that described for masonry specimens loaded with an inclined load.

Murthy and Hendry (44) report "1/6-modal" tests on three bay, one-story, shear walls, 0.669" thick, about 16" in height and length. The bricks had an average strength of 4421 psi and the cement-lime-sand mortar about 1200 psi. The horizontal shear strength was tested for various additional loads up to 180 psi, and the following relationship was established:

$$f_s = 30 + 0.5 f_n \quad (1.6)$$

$$f_n \leq 180 \text{ psi}$$

Benjamin and Williams (5) tested model walls, without frames and without vertical loads, and found apparent shear strengths of 15 psi to 30 psi.

1.3.6 Test on Small Masonry Assemblages: at the University of Mexico, Meli and Reyes (39) conducted tests on small assemblages for investigating the mechanical properties of masonry. Three tests were found to be the most useful: a small prism subjected to axial compression, a wallette under diagonal compression, and a three unit assemblage subjected to shearing of the joints. Results of the prism test were related with the behavior of masonry walls under vertical loads. The remaining two tests were related with the behavior of walls under lateral loads. Tests were performed on a large number of specimens built with commonly used types of masonry units and mortars.

Based on test results, it was found that the prism with height/thickness ratio of 4.0 gave satisfactory and uniform index to the resistance to axial load of masonry.

Figure 1.10 shows the schematic test setup adopted for the shearing tests on joints with precompression. The results were expressed in the form of Equation (1.1) with $C = 1.8 \text{ kg/sq cm}$ and $\mu = 0.8$ for concrete blocks with different types of mortar whose strengths varied from 151 kg/sq cm to 43 kg/sq cm. Coefficient of friction was found to be a very uniform property for the different types of bricks and concrete blocks adopted. The values were approximately

0.7 in all the cases. However, the value of adhesion varied depending on the type of brick and mortar. At low levels of confinement, the results varied; however, uniformity in results was obtained with high level of precompression.

Figure 1.11 shows the different types of specimens adopted for the diagonal compression tests. For each series of specimens shown in Figure 1.11, four different types of mortars and seven types of masonry units were used. For each combination of materials, there were three specimens of each type. The object of the series of the tests was to study the effect of the variation of the height/width ratio (h/l) of the panel and number of joints in the specimen on the resistance of the assemblage. The results showed that each type of specimen had a definite mode of failure independent of the type of mortar used. In general, the failure occurred by shearing along the joints for long specimens and by diagonal tension for specimens with high h/l ratio. The type of failure was not always perfectly defined. In many cases, the crack crossed the joints and the blocks partially. Qualitatively, it could be said that when the failure was by diagonal tension, the resistance was relatively uniform for similar specimens and did not depend much on the type of mortar used. On the contrary, when the failure was by shear, the dispersion of results was very high. It was found that the resistance increased with increase in h/l ratio.

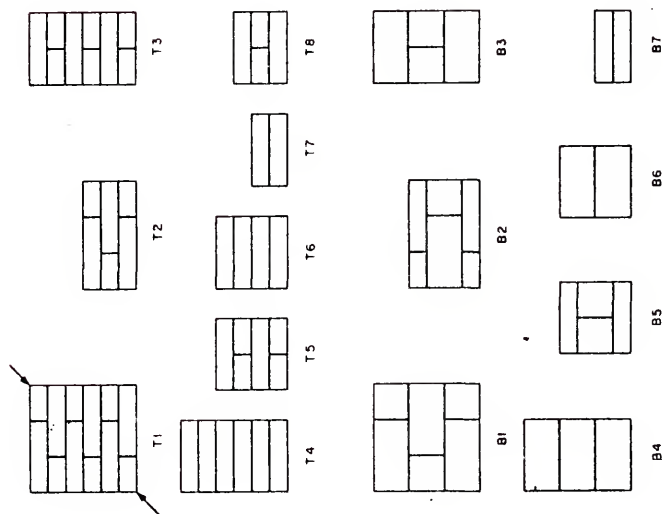
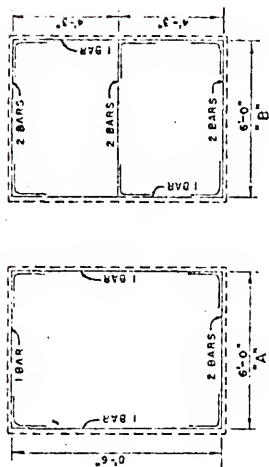
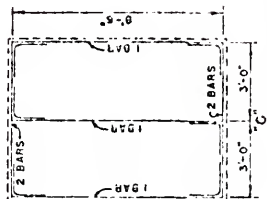


Fig. 1.11. Types of test specimens adopted by Meli and Reyes for diagonal compression tests.



NOTE: ALL BARS $\frac{1}{2}$ " ROUND
DEFLECTED BARS OF
STRUCTURAL GRADE STEEL
BARS IN CORNERS ARE
APPROXIMATELY 33" LONG
BENT 90° IN CENTER



STEEL ARRANGEMENT
WALLS IN SHEAR
SERIES 'H'

TESTS ON REINFORCED MASONRY
PORTLAND CEMENT ASSOCIATION
LOS ANGELES CALIFORNIA
NOVEMBER 1945

Fig. 1.12. Test panels adopted by Converse.

However, the effect of this increment was of very little influence when the failure was by diagonal tension and very much noticeable when the failure was by shearing along the joints. It might be due to the fact that the h/l ratio controls the value of compression normal to the joints that causes the effect of friction to be developed.

All the specimens considered in this investigation were nongrouted. It was found that the strength in diagonal tension was equal to the square root of the compressive strength of the prism when the stresses were expressed in kg/sq cm.

For the shear failure along the joints, a relation similar to that of Polyakov (42) was proposed:

$$f_s = 0.8 / (1 - 0.9 \mu h/l) \quad (1.7)$$

1.3.7 Reinforced Concrete Masonry Walls in Shear: Figure 1.12 shows the steel arrangement of reinforced concrete masonry walls tested by Converse (12). The basic mode of failure was one of diagonal tension. Walls under group 'B' showed an increase in strength of 38% over group 'A'. It suggested that the increase in strength was nearly proportional to the areas of additional steel, irrespective of position. Due to the difference in number of bars, no direct comparison could be made of the relative effect of vertical and horizontal steel, but indications were that they were equally effective.

Scrivener (48) confirmed the previous findings in his tests. The objectives of his tests were to determine:

1) the pattern of behavior as the percentage of reinforcing was increased, 2) the relative effectiveness of vertical and horizontal reinforcing, and 3) the difference between the behavior of walls where the vertical steel was peripheral and where the steel was distributed over the length of the wall. The following conclusions were drawn from these series of tests:

1) Vertical and horizontal reinforcing are equally effective in producing satisfactory crack behavior and failure loads.

2) Walls with evenly distributed reinforcing have a later onset of severe cracking than walls where the reinforcement is concentrated in the wall periphery.

3) With a low percentage of reinforcing, failure occurs soon after the onset of severe cracking. With higher percentages of reinforcing, the failure load is much greater than the load causing severe cracking.

4) Higher failure loads were obtained with walls with higher percentages of reinforcing up to 0.3% of the gross cross-sectional area of the wall. Above this percentage, additional reinforcing had little effect on the failure load. From the walls with the optimum (0.3%) or higher percentage of reinforcing, the ultimate horizontal shear stress

(ultimate load divided by the gross cross-sectional area of the wall) was found to be 170 psi.

Confirmation of the last conclusion can be had from the test results of Schneider (45), who found a maximum effective quantity of reinforcement of 0.2%. In his tests, a racking load only was applied, but sufficient peripheral vertical reinforcement was placed in the walls to prevent this steel being stressed beyond its yield point when subjected to the tensile forces induced by the maximum overturning moment. Schneider's walls failed in shear with the typical diagonal cracking. The difference between Schneider's and Scrivener's test walls lies in the boundary conditions on the vertical sides. Schneider also found that, workmanship and reinforcement remaining the same, the shear resistance of stack and running bond and stack bond masonry block walls was about the same.

1.3.8 Effect of Wall Openings: openings in shear walls are mainly due to doors, corridors and mechanical duct space. When the opening is relatively small and spaced, at least a distance equal to the size of the opening in each direction, its influence on the behavior of the structure is negligible (29). Figure 1.13 shows an elevation of a typical shear wall in an apartment building using an 8" concrete, flat plate slab construction. The opening shown at the center indicates the corridor at each floor. In

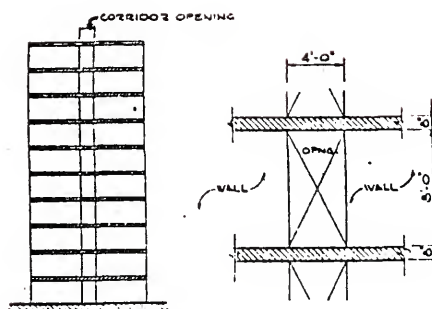


Fig. 1.13. Continuous opening in a shear wall.

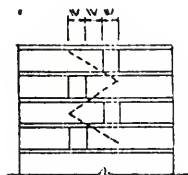


Fig. 1.14. Staggered opening in a shear wall.

apartment buildings, the opening would normally be from top of the floor to bottom of the floor above. In apartment buildings where the architectural planning frequently permits the shear wall to extend from one face of the building to the other, openings such as shown in Figure 1.13 limit the full utilization of the entire shear wall as a unit. The connecting slab at each opening is relatively very flexible. As a result, the shear wall acts as two individual shear walls on either side of the corridor opening. Although for medium height buildings, this inefficiency does not seriously affect the economy of the entire structure, for heights above 40 stories, its effect on overall economy becomes significant. As a solution to this problem, Khan (29) proposes staggering of such openings at alternate floors in order to maintain the structural continuity of the entire shear wall. Figure 1.14 illustrates the proposed arrangement.

In office buildings the requirement for mechanical duct space under the floor slab makes the problem of openings different from that in the apartment buildings. A hung ceiling is almost always necessary. The door opening size generally allows a 2 ft to 5 ft connecting beam over each opening. The proper analysis and design of the connecting beam is important because the beam not only connects the adjacent parts of a shear wall for monolithic action, but also redistributes loads in different parts of

the shear wall. Girijavallabhan (21), on the basis of an analysis using the Finite Element Method, found that one of the most influencing factors on the distribution of stresses and deformations in the shear wall was the stiffness of the lintel beam. He varied the depth of the lintel beam and studied the influence of the variation on the overall behavior of the shear wall.

Kokinopoulos (30) conducted a photoelastic analysis on models of single story walls with openings to study the effect of size of opening on the stress distribution in walls. Schneider (46) conducted full scale tests on piers in a shear wall with openings. This is the only experimental investigation on this problem which utilized full scale tests. This investigation is described in the next subsection.

1.3.9 Shear in Concrete Masonry Piers: this investigation was carried out to estimate the capacity of concrete masonry piers, functioning within the confines of a shear wall in a building, to resist lateral load effects. To simulate as nearly as possible conditions that occur in an actual wall, such as degree of restraint, amount of reinforcing, manner of vertical load imposition, and magnitude of secondary stresses, the pier was considered along with the wall around it (Figure 1.15). The fully restrained configuration was either 10' 8" or 11' 4" high. The cantilever pier was either

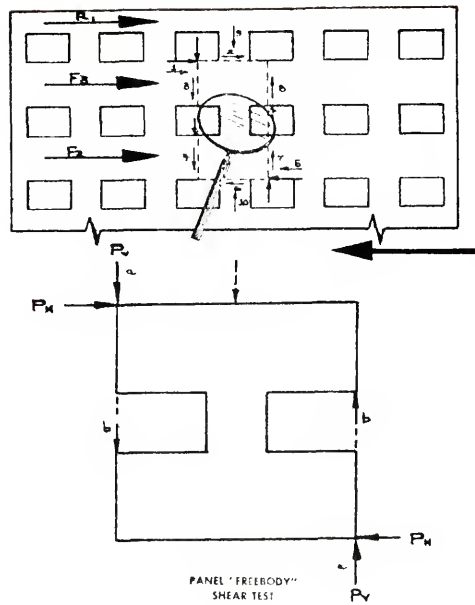


Fig. 1.15. Forces acting on a pier element in a wall with opening.

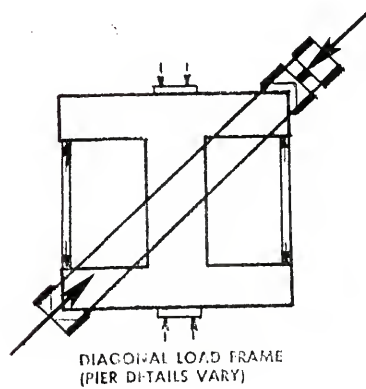


Fig. 1.16. Test setup adopted by Schneider for full scale tests on piers.

7' 4" high and 8' 0" wide or 10' 0" high and 10' 8" wide. Also tested was a set of 48" square concrete masonry assemblies. A diagonal loading frame was used to apply the loading (Figure 1.16). Pipe columns were used to maintain the geometry of the openings.

The important variables considered were:

- 1) a/D ratio, where a is the distance from the point of inflection to the spandrel restraint, and D , the overall pier depth.
- 2) Amount of web reinforcement (both horizontal and vertical).
- 3) Amount of jamb reinforcement.
- 4) External axial compressive stress.
- 5) Nongrouted panel behavior.

The average strength of blocks used varied from 1338 psi to 2962 psi. The 28-day mortar strength varied from 2487 psi to 5116 psi. The strength of grout prisms varied from 1789 psi to 3414 psi. Reinforcing steel conforming to ASTM A 15, had a yield strength of 55,000 psi and ultimate tensile strength of 80,000 psi.

The following are the main findings of this investigation:

- 1) The shear strength increased with a decrease in the a/D ratio, and this rate of increase jumped sharply below an a/D ratio of 0.5:1.

The very consistency of the test results throughout the range of a/D ratios selected for analysis suggested the

following relationships for average ultimate shear stress of a pier contained within a shear wall, where web reinforcement is not provided:

<u>M/VD (a/D)</u>	<u>ULTIMATE MASONRY SHEAR STRESS, v_u, psi</u>
<u>Fixed Pier Elements:</u>	
0.10:1 ≤ M/VD ≤ 0.50:1	V/tD = 310 - 350 M/VD
0.50:1 ≤ M/VD ≤ 1.50:1	V/tD = 152.5 - 35 M/VD
1.50:1 ≤ M/VD	V/tD = 100 psi
<u>Cantilever Pier Elements:</u>	
1.0:1 ≤ M/VD ≤ 3:1	V/tD = 95 - 15 M/VD
3.0:1 ≤ M/VD	V/tD = 50 psi

where M equals spandrel moment, V equals base shear, D equals overall pier depth, a equals distance from the point of inflection in the span of the pier to the fixed end, and t equals net thickness of wall.

2) The presence of adequate horizontal web reinforcement materially increased the shear resistance of the pier.

The following relationships between the M/VD ratio and ultimate shear stress were proposed for piers with horizontal web reinforcement.

ULTIMATE MASONRY SHEAR STRESS
WITH ADEQUATE WEB REINFORCEMENT,
 v_u , psi

M/VD (a/D)

Fixed Pier Elements:

$0.10:1 \leq M/VD \leq 0.50:1$	$V/tD = 347.5 - 225 M/VD$
$0.50:1 \leq M/VD \leq 1.50:1$	$V/tD = 290 - 110 M/VD$
$1.50:1 \leq M/VD \leq 2.00:1$	$V/tD = 200 - 50 M/VD$
$2.00:1 \leq M/VD$	$V/tD = 100 \text{ psi}$

3) Vertical steel did not seem to function effectively as web reinforcement.

4) Assuming that enough jamb steel was present to resist the end moments, any further increase did not alter the pier resistance appreciably.

5) The existence of a bedjoint fracture at a foundation did not seem to impair the ability of the panel to resist lateral loads. However, if a bedjoint crack occurred at the center of a square panel, where tensile stresses are maximum, its shear resistance was drastically reduced.

6) The energy absorbing ability of an adequately reinforced masonry pier was well demonstrated. As the shape of the load deflection curves indicated, these piers were able to absorb a great deal of inelastic strain energy without collapsing or even spalling seriously.

7) Concrete masonry, if properly reinforced, exhibits a tendency toward a ductile behavior throughout the loading

sequence. It can sustain significant proportions of the ultimate load well into the inelastic regions (beyond the first significant crack) while undergoing rather large lateral deflections. It also exhibits effective dampening characteristics, especially after cracking.

8) On the basis of defining ductility as the ratio of the total deflection experienced to the deflection at the first shear crack, which was assumed to be the inception of inelastic deformation, the ductility factor exceeded two, which is considered a desirable level.

1.3.10 Strength of Masonry under Combined Compression and Shear: Sinha and Hendry (50) propose that brickwork subjected to combined compression and shear exhibits two distinct types of failure:

1) Shear failure at the brick/mortar interface. The shear strength consists of initial bond shear and the resistance, proportional to the normal stress, due to friction between brick and mortar.

2) Diagonal tensile cracking through bricks and mortar governed by constant maximum tensile stress or strain.

On the basis of tests on circular shear specimens, Sinha and Hendry found the diagonal tensile strength of brickwork to be:

$$f_t = 2.0 \sqrt{f'_m} \quad (1.8)$$

Let f_y equal precompression applied to brickwork and f_s equal shear stress. If it is assumed that failure is determined at a certain stage by the criterion of maximum tensile stress, then:

$$f_t = \sqrt{f_y^2/4 + f_s^2} - \frac{f_y}{2} = \text{constant} \quad (1.9)$$

For failure:

$$f_s \geq \mu f_y$$

It is assumed that the above condition will be fulfilled by two values of f_y : f_{y1} and f_{y2} . Between the precompressive stresses f_{y1} and f_{y2} failure of the structure will occur by attaining maximum tensile strength. Below and above this range, failure will be governed by shear at the brick/mortar interface. Precompression above f_{y2} will suppress the inherent failure due to diagonal tension and modify its value. At very high precompression values, the failure of the brickwork will take place in compression.

Since $f_s = C + \mu f_y$, where C is the initial bond shear strength between brick and mortar,

$$f_t = \sqrt{f_{y1}^2/4 + (C + \mu f_{y1})^2} - f_{y1}/2 \quad (1.10)$$

When $f_s = \mu f_{y2}$,

$$f_t = \sqrt{f_{y1}^2/4 + (\mu f_{y2})^2} - f_{y2}/2 \quad (1.11)$$

Knowing f_t , C and μ , f_{y1} and f_{y2} can be calculated. Thus, the ultimate shear strength may be calculated from the following formulae:

$$f_s = C + \mu f_y \quad (1.12)$$

for $\mu f_y \leq f_{y1}$, and,

$$f_t = \sqrt{f_y^2/4 + f_s^2} - f_y/2 \quad (1.13)$$

for $f_{y1} \leq f_y \leq f_{y2}$, and,

$$f = \mu f_y \quad (1.14)$$

for $f_{y2} \leq f_y \leq$ compressive strength of brickwork.

However, in a recent study, Smith et al. (51) have concluded that the diagonal tensile strength of brickwork is approximately equal to the tensile strength of brickwork or mortar, whichever is weaker. This conclusion was based on an analysis of a masonry circular shear specimen using the Finite Element Method supported by experimental data.

1.4 Objectives and Scope of Present Investigation: A survey of the available literature revealed a need for more elaborate research on shear strength of concrete masonry walls with openings. To meet this objective, an experimental and an analytical investigation is attempted in this dissertation. In the experimental investigation, it was decided to adopt the test specimen proposed by Schneider (46). Thus, the main objective of the experimental investigation was to obtain empirical equations to predict the shear capacity of grouted and nongrouted piers without reinforcement. Since the effect of various types of configurations and reinforcement had already been established, it was decided to restrict the investigation to one particular configuration. The main variables considered for grouted piers were the grout and mortar strengths; for the nongrouted piers, the effect of external precompression normal to bedjoints was treated as the main test parameter for different types of mortar adopted.

Since the strength of mortar joints is a main factor determining the behavior of a nongrouted masonry element, an extensive study was initiated to obtain equations for predicting the strength of mortar joints under combined compression, bending and shear. This investigation is described in Chapter 3.

A full-scale testing of piers was not possible because of limitations of capacity of testing machines, space, and cost. The present investigation on piers was restricted to 1/4-size models. Chapters 4 and 5 describe the model tests on piers.

While investigating a complex phenomenon such as the behavior of masonry, if a suitable analytical model could be proposed, it would facilitate understanding the stress distribution in the structure more thoroughly. Such a model was attempted using the Finite Element Method. The model chosen was capable of predicting the different failure modes associated with masonry and a nonlinear finite element analysis was adopted accordingly to determine the ultimate load and failure pattern. The analytical results were compared with experimental ones. The analytical investigation is described in Chapters 6 through 8.

CHAPTER 2

EQUIPMENT, MATERIALS AND TESTING TECHNIQUES

2.1 Testing Machines and Other Equipment: The Civil Engineering Laboratory is equipped with a hydraulic press of 300,000 lb capacity and a mechanical press of 160,000 lb capacity. The clearance of these two machines allowed good observations of all sides of the specimen being tested. For testing the model reinforcement, the 10,000 lb capacity, Instron Machine, Model TTC, in the department of Metallurgical Engineering was used. The machine was provided with suitable gripping devices for clamping small test specimens and an automatic recorder for plotting the load-extension curves.

The investigation on the strength of mortar joints was carried out in the 300,000 lb hydraulic press. The higher clearance and lower load ranges required for the model tests determined the use of the 160,000 lb mechanical press for testing model piers.

Sieves, mechanical shakers, and balances were available for analysis of sand.

An electric rotary mixer of 5 cu ft capacity was used in mixing mortars for building 3-block prisms used for determining the strength of mortar joints under combined stresses.

The same mixer was also used for mixing cement-sand mortar for making spandrels for piers. A standard flow table, standard molds for mortar cubes, paper molds for mortar cylinders, and different size rods were used for mortar and grout control.

A large moist room was used for storage of mortar cubes and cylinders, and sufficient storage room was available for the masonry prisms and model specimens.

A 6" diameter brass disc (normally used for capping concrete cylinders), together with four 1/4" x 1/4" brass bars, formed a mold for the sulfur caps of the model concrete blocks and prisms.

Dial gages with a least count of 0.001" were used for measuring deflection. They were mounted on magnetic stands for easy removal.

The electrical strain gages used were BLH's SR-4 fixed on the test surface with Duco cement. The strain indicator was a portable Baldwin Type N. The strain gages were wired to the indicator through a switch selector.

2.2 Concrete Blocks: The concrete blocks used for the first investigation had nominal dimensions of 8" x 8" x 16". The net area of a block based on the average of five specimens was 61.4 sq in. Selected blocks were capped with sulfur and tested according to ASTM C-90 and C-140. The average compressive strength based on net area was 6500 psi. The initial rate of absorption (IRA) of the block, according to

ASTM C-67, is measured as the amount of water initially absorbed by a dry unit when it is partially immersed in water to a depth of $1/8$ " for a period of one minute. IRA is measured in grams per minute per 30 square inches. The test was conducted in the following manner.

Four steel bars, $1/4$ " x $1/4$ " in cross-section and 4" long, were provided with needles $1/8$ " high. A steel pan, which area was much larger than the gross area of the concrete block, was chosen and placed on a level surface. The steel bars were positioned on the pan in such a manner that the concrete block could rest on them. Water was allowed to stand in the pan till the needle points were just immersed. The previously weighed block was placed in position over the steel bars, and the water supply was continued to cope with the absorption of the block. After one minute, the block was removed, the immersed surface wiped, and the block reweighed. The initial rate of absorption of the blocks varied between 12 g to 17 g/min/30 sq in.

An indirect tension test was conducted to find the tensile strength of the block (49). Two test methods were devised for splitting hollow concrete block. The first method, shown in Figures 2.1(a) and 2.1(b), was arranged so that the block could be split twice. The load was applied through hexagonal bars with $3/4$ " flats, first through one cell and then through the other cell of the block. The second method, shown in Figure 2.1(c), was arranged to load



Fig. 2.1. Splitting tests on concrete block.

both cells simultaneously. Round bars of 1-3/8" diameter were used to distribute the load in this test. Usually only one split occurred as is shown in Figure 2.1(d). The results of the tests are given in reference (49). The indirect tensile strength of the block was calculated using the relation:

$$f_t = \frac{2P}{\pi A} \quad (2.1)$$

where P is the splitting load and A the sectional area of split. In the range of the block strengths tested, it appears that the split tensile strength is approximately five times the square root of the compressive strength as determined by the standard block compression test. For the blocks used in this investigation, the indirect tensile strength was found to be 405 psi.

2.3 Mortar: The cements and sand were provided by local suppliers in Gainesville, Florida. The cements were manufactured by Florida Portland Cement. Portland Cement Type I and Masonry Cement were used in the mortar mixes in accordance with ASTM C-270-68. The granulometry of the sand is shown in Figure 2.2. For the first investigation, two types of mortars were used. The following are their proportions by volume.

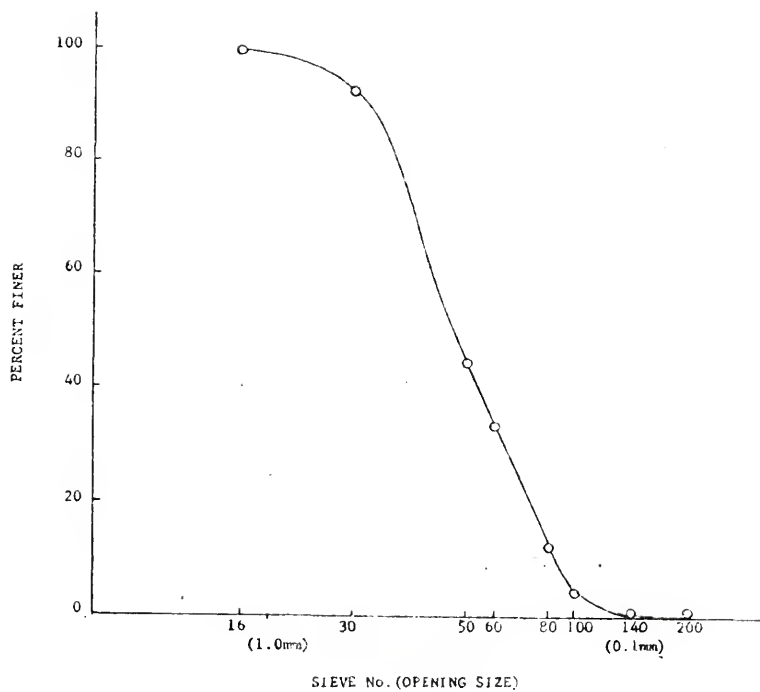


Fig. 2.2. Sieve analysis of sand for masonry mortar.

	<u>PC</u>	<u>MC</u>	<u>Sand</u>
Type I	1	1	4.5
Type II	1	1	6

An initial rate of flow of about 100% was adopted. Two-inch cubes were molded and tested according to ASTM C-270. The average compressive strength of Type I mortar was 1948 psi and that of Type II 917 psi.

2.4 Model Concrete Blocks: The model concrete blocks were provided by the National Concrete Masonry Association, Arlington, Virginia. They were modelled to be one-fourth the size of the full block of nominal dimensions 8" x 8" x 16". Thus, the model block had nominal dimensions of 2" x 2" x 4". A typical block is shown in Figure 2.3. The average length of the block was 3.9", width 1.9", and height 1.85". The net area, based on an average of six specimens, was 4.16 sq in. The model blocks, capped with 0.15" thick sulfur capping, were tested in axial compression. The average of thirteen tests yielded a compressive strength of 2688 psi based on net area. The coefficient of variation was 20.15%.

The absorption of the model block was 11.98%. It was difficult to measure the initial rate of absorption for the model blocks because 1) their rate of absorption was quite high, and 2) a suitable depth of immersion of surface could not be defined for models.

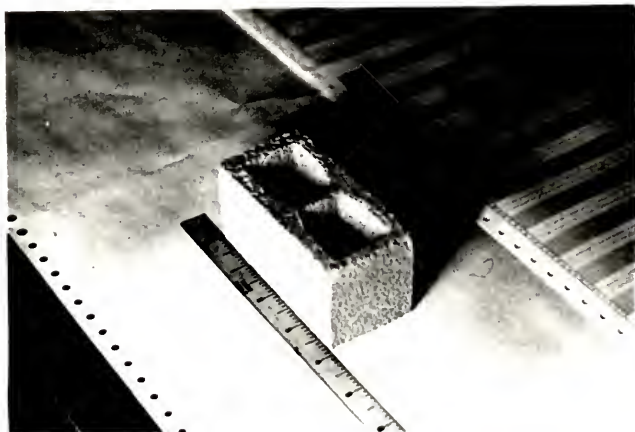


Fig. 2.3. Model concrete block



Fig. 2.4. Model reinforcement (0.147" dia.).

The tensile strength of the block could not be determined by an indirect tension test because of the uncertainties involved in choosing the size of splitting bars for models. Also, a suitable testing machine was not available. A value equal to five times the square root of the compressive strength of the block was assumed.

In order to obtain the stress-strain curve in compression, two SR-4 gages were mounted centrally, one on each longitudinal side. The gage length was 0.2". The stress-strain curve obtained is shown in Figure 2.5.

2.5 Model Reinforcement: Number 2 bars of 40 ksi grade steel were used for main reinforcement in spandrel beams of model piers. For vertical and shear reinforcements, 0.147" diameter, high strength Duro-Wall bars were used. A typical bar is shown in Figure 2.4. The bar had minute depressions 0.3" long and alternate projections 0.1" long. The yield and ultimate strengths of the bar were, respectively, 68 ksi and 75 ksi. A typical stress-strain curve is shown in Figure 2.6.

2.6 Model Mortar: Based on trial mixes, the proper grade of sand for modelling Type I and Type II mortars was arrived at. The sand, of gradation shown in Figure 2.2, was sieved through a set of sieves (nos. 8, 16, 30, 50, 100, and 200, in that order). Trial mixes were made with the sands retained on sieves nos. 50, 100, and 200. It was found

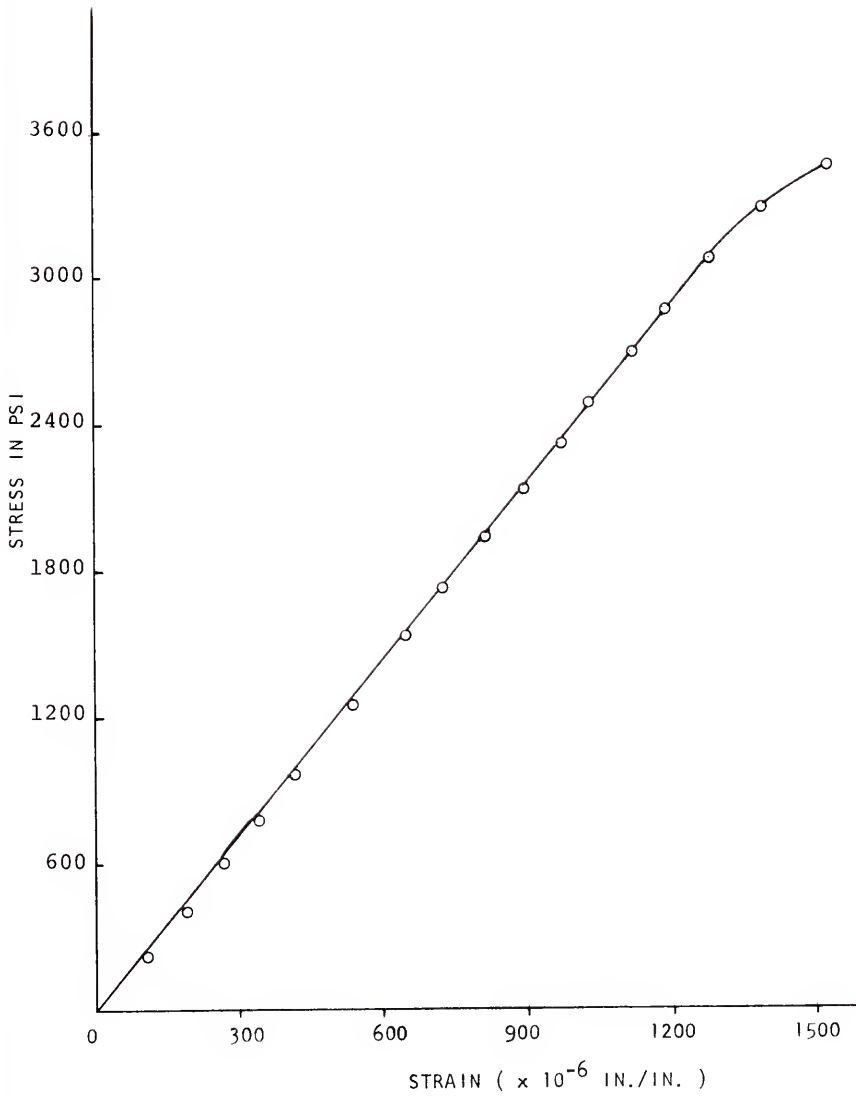


Fig. 2.5. Stress-strain curve for model concrete block.

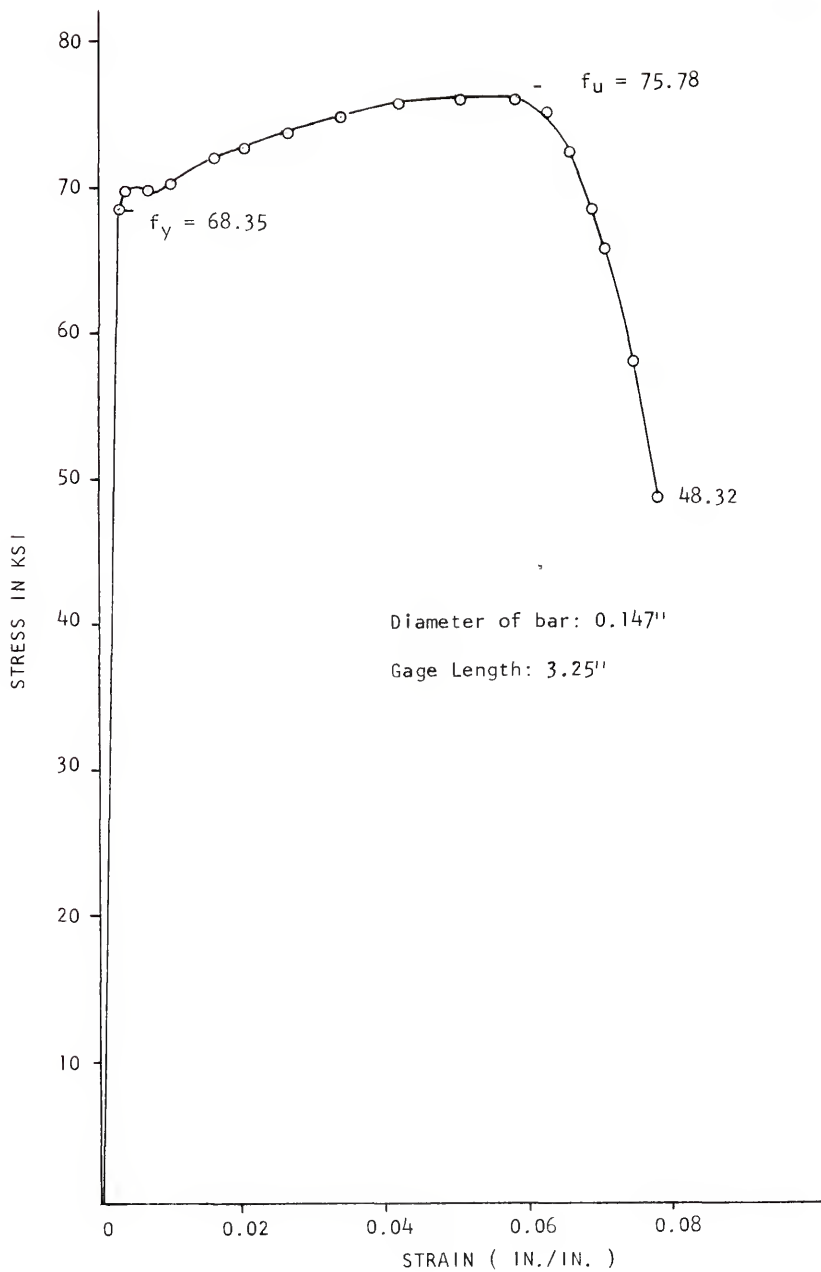


Fig. 2.6. Stress-strain curve for model reinforcement.

that for the same water-cement ratio and proportions of ingredients, the strengths of mortar obtained, using the sand retained in no. 100 sieve, compared favorably with those of Type I or Type II, as the case may be. Hence, this grade was chosen as the model sand. No attempt was made to model cements. An initial flow of 120% was adopted. Compressive strength of the mortar was determined by testing standard 2" cubes. The tensile strength was obtained by splitting cylinders 3" in diameter and 6" long. The model mortar properties are summarized in Table 2.1. Plates, 5.75" x 5.75" x 0.625", made of the different types of mortar and cured in air, were tested in uniaxial compression. The plate compression strength was used in the analytical investigation described in Chapter 8. The stress-strain curves for the two types of mortars obtained on the basis of tests on 3" x 6" cylinders are given in Figure 2.7.

2.7 Model Grout Mixes: No gravel could be used in model grout because of difficulties in obtaining proper compaction due to the small size of the cells. Hence, the model grout consisted of only cement and sand. Standard 2" cubes molded in standard molds and cured in air were used for measuring the compressive strength of the grout. Due to the uneven surfaces obtained for cubes molded by using the concrete blocks as molds, the test results on those cubes were not satisfactory. Plates, 5.75" x 5.75" x 0.625", were tested in uniaxial compression. Their compressive strengths were

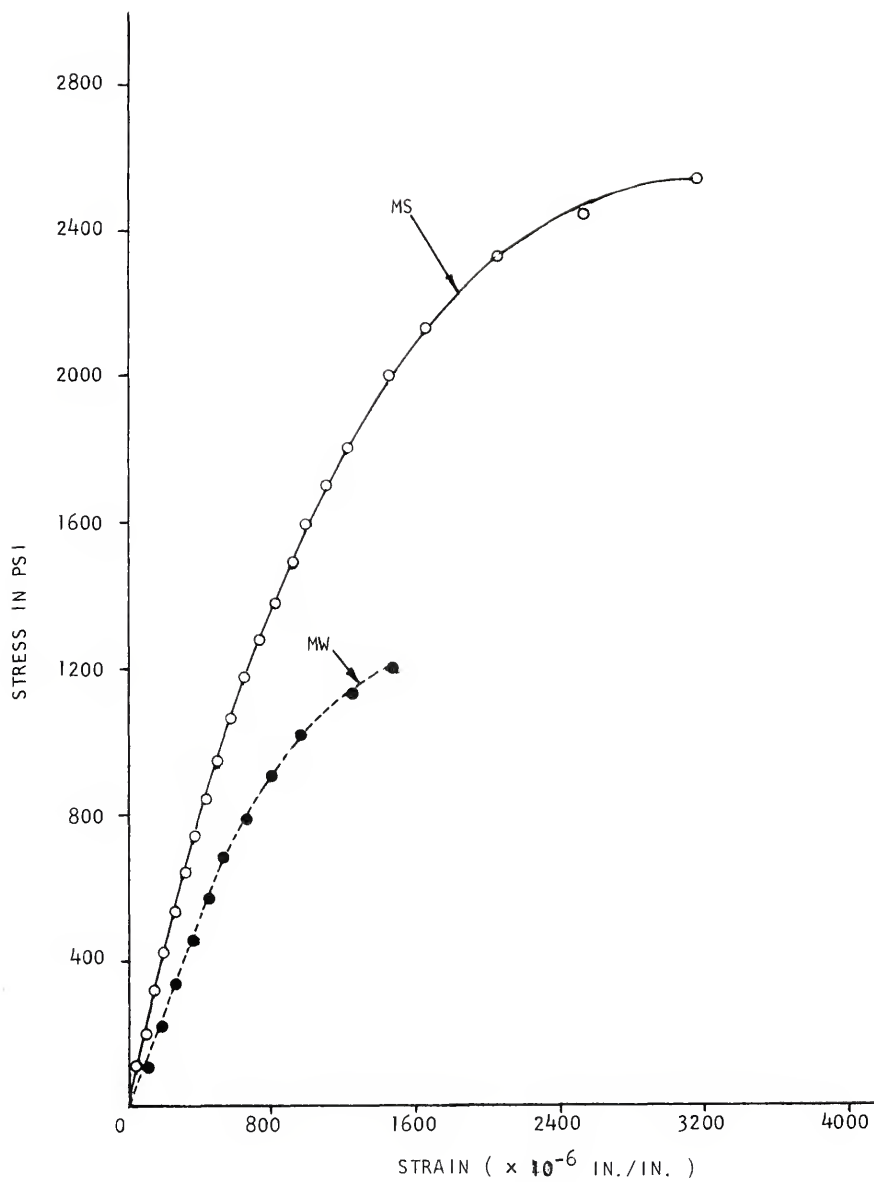


Fig. 2.7. Stress-strain curve for model mortar.

TABLE 2.1
 PROPERTIES OF MODEL MORTAR AND GROUT

	Type	Proportions by Volume			Initial Rate of Flow %	28-day Strength		
		PC	MC	Sand		Plate psi	Cube Comp. psi	Split Cylr. psi
Mortar:	MS	1	1	4.5*	120	656	1695	200
	MW	1	1	6 *	120	485	905	135
Grout:	GW	1		5 +		450	570	75
	GM	1		4 +		760	800	205
	GS	1		3 **		1000	1850	322

Note: * Gradation of sand: passing through sieve no. 50 but retained on sieve no. 100.

+ Gradation of sand: passing through sieve no. 30 but retained on sieve no. 50.

** Gradation of sand: as shown in Figure 2.2.

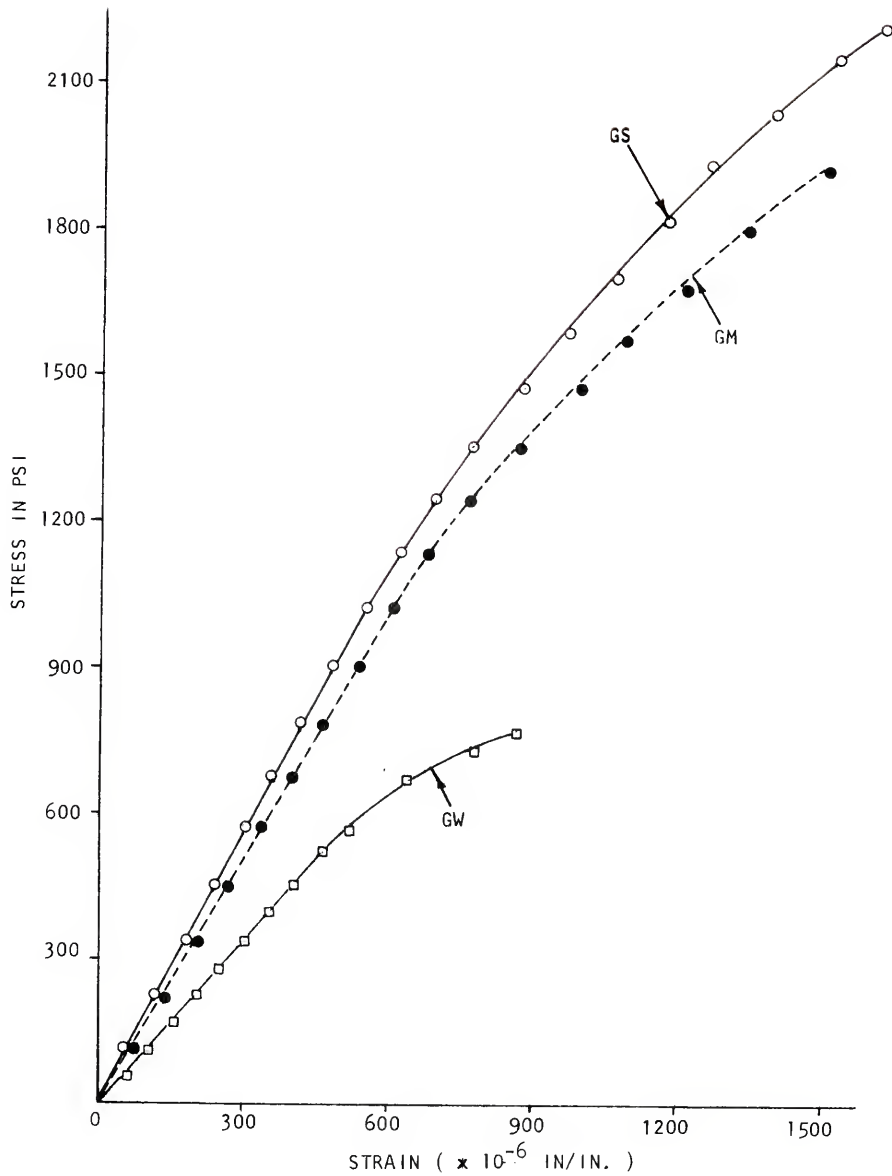


Fig. 2.8. Stress-strain curve for model grout.

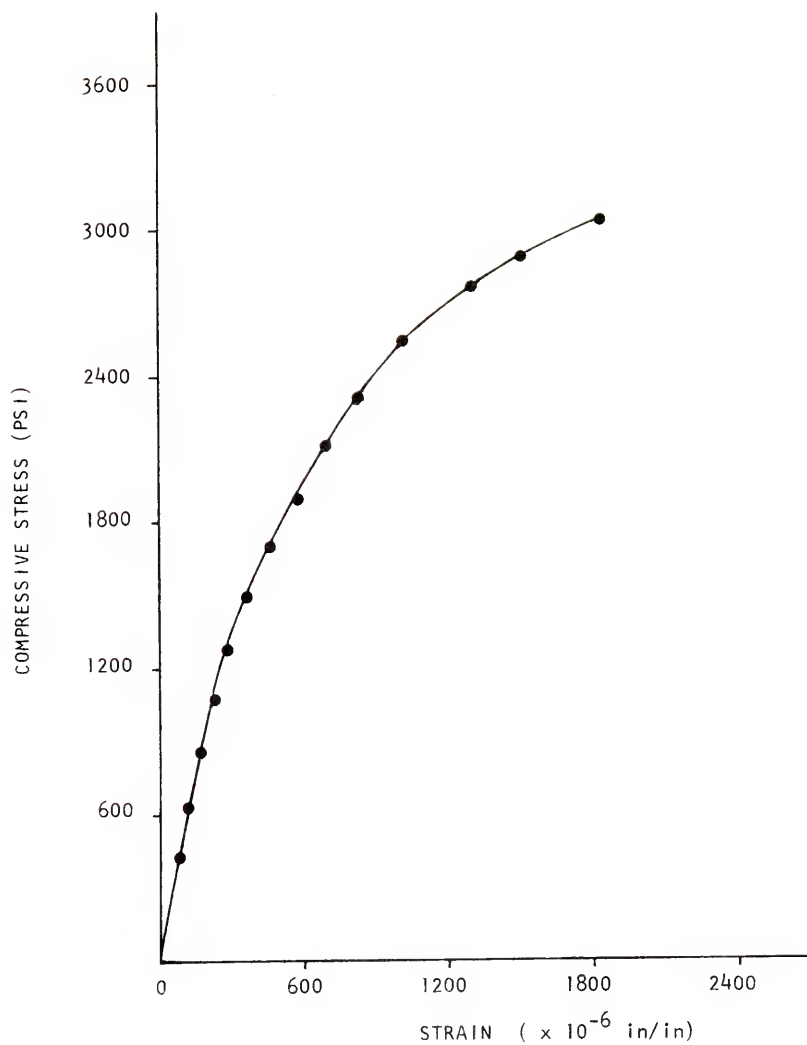


Fig. 2.9. Stress-strain curve for spandrel mortar.

required for use in analysis later. The indirect tensile strength was obtained by splitting cylinders 3" in diameter and 6" long. The properties of grout mixes adopted are summarized in Table 2.1. For grout types GW and GM, the sand used was of such a grade it passed through sieve no. 30, but was retained on sieve no. 50. For type GS, the sand used for mortars Type I and Type II was adopted. Initially, the required amount of water was determined by trial for each type so that the grout could easily be poured in the cells without separation of its components. The stress-strain curves obtained using 3" x 6" cylinders are shown in Figure 2.8.

2.8 Mortar Mix for Spandrel: A mortar mix of the following proportions by weight was used in forming the spandrel of the pier specimen used in model tests described in Chapter 4: Portland Cement:Sand (river sand used in concrete mixes) = 1:3. A water-cement ratio of 0.55 by weight was adopted. The compressive strength of the mix was 3830 psi and the tensile strength 400 psi. Compression tests on a plate of 5.75" x 5.75" x 0.625" yielded 2300 psi. The stress-strain curve obtained by testing 3" x 6" cylinders under uniaxial compression is shown in Figure 2.9.

CHAPTER 3

STRENGTH OF MORTAR JOINTS UNDER COMBINED STRESSES

3.1 Scope: This study was designed to investigate the influence of precompression upon the shear and flexural tensile strengths of mortar joints in concrete block walls. First, the strength of the joint is studied under a state of pure shear. Secondly, this is followed by a study of pure bending. In the third phase, the strength of the joint is studied under combined bending and shear for a known amount of precompression. Combining the above, the study is directed toward obtaining interaction diagrams that can be used to predict behavior under combined loading.

The structural bond between mortar and units is an important factor in the structural behavior of masonry walls where the masonry is subjected to forces which produce tensile and/or shearing stresses in the joints. Factors which seem to influence the bond of masonry mortars are (13)(25): 1) composition, 2) suction rate (IRA), 3) initial moisture content of the block, 4) compressive strength, 5) air content, 6) initial flow of mortar, and 7) curing of specimens. Shear bond may be considerably increased by the presence of compressive stress normal to the shearing force.

In the present investigation, only the mortar composition and strength were considered as variables. Other factors such as suction rate, initial flow, block characteristics and curing procedures were standardized and held constant.

3.2 Test Specimens: Test specimens were standard 3-block prisms with 3/8" mortar joints. All specimens were air-cured under laboratory conditions. The initial rate of absorption of the blocks varied between 12g to 17 g/min/30 sq in. The net area of a block, based on the average of five specimens, was 61.4 sq in. Since the blocks were fully bedded, this value was taken as the area of a mortar joint. Type M mortar was used with two compositions. The properties of mortars used are summarized in Table 3.1.

3.3 Strength of Mortar Joints under Compression and Shear: A simple method was developed for applying shear to the joints while a constant uniform compressive stress was maintained across the joints. The specimens were supported and loaded in such a way that the joints were at the points of contraflexure. The testing arrangement adopted by Base (4) was used with certain modifications. The test setup adopted is shown schematically in Figure 3.1 and positioned in the hydraulic press in Figure 3.2. The axial force across the section was applied through steel rods and was varied by tightening nuts at the threaded ends. The amount

TABLE 3.1
PROPERTIES OF MORTAR

Specimens	Mortar Type	Proportion by Volume			Initial Rate of Flow %	28-day Strength	
		PC	MC	Sand		Cube Comp. psi	Split Cylr. psi
PSM 1-12	II	1	1	6	90	864	172
PSM 13-25	II	1	1	6	103	932	198
PSM 26-37	I	1	1	4.5	96	2138	290
PSM 39-41	II	1	1	6	110	956	-
PSM 42-44	I	1	1	4.5	100	1758	-

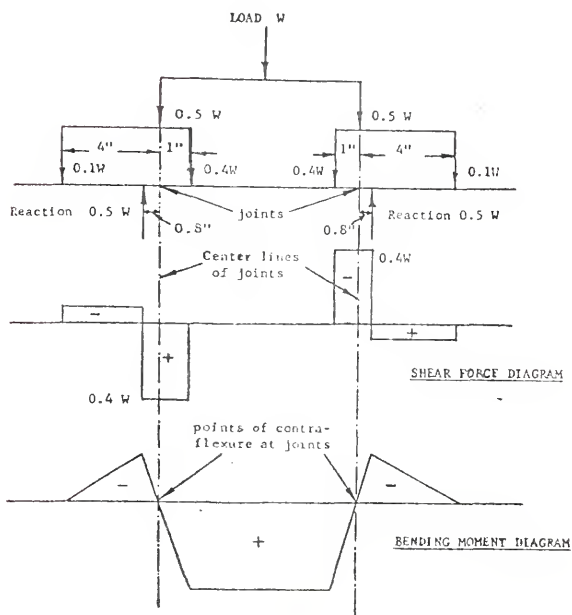
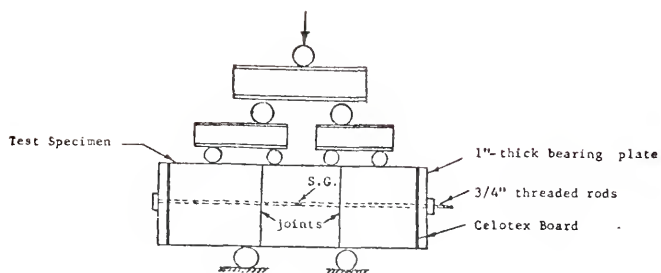


Fig. 3.1. Setup for studying the strength of mortar under pure shear.



Fig. 3.2. Test setup for finding the strength of mortar joints under combined compression and shear.



Fig. 3.3. Shear failure through mortar joint.

of prestress developed in the rods is found by measuring the strains with electrical strain gages. On each rod, two strain gages were mounted diametrically opposite to each other and connected in series to compensate for bending effects.

Table 3.2 presents the summary of test results for the low strength mortar and Table 3.3 for the high strength mortar. For the low strength mortar, at precompressions up to 220 psi, bond failures were observed; but at a precompression of 300 psi, shear failure through the mortar frequently occurred. Figure 3.3 shows an example of shear failure through the joint. However, for the high strength mortar (within the range of precompression adopted), the failure pattern was always one of bond. Testing beyond the range of precompression (300 psi for the high strength mortar) was not possible due to flexural failure of the concrete block.

Figure 3.4 shows the plot between precompression and the shearing strength of mortar joints. It is evident that the effect of precompression is to increase the shearing strength of the joint considerably. It can also be observed that a higher strength mortar does not appreciably increase the shear strength. This statement cannot be generalized because, within the range of precompression applied thus far in this investigation, bond failures were usually observed. It is quite possible to have an increased

TABLE 3.2
STRENGTH OF MORTAR JOINTS UNDER COMPRESSION AND SHEAR

Specimen	Age (days)	Precom- pression (psi)	Mortar Strength (psi)	Failure Load (lbs)	Shear Strength (psi)	Mean (psi)	Coefficient of Variation (%)
PSM 5	64	0	881	3,000	19.5	19.5	-
PSM 7	106	100	890	13,850	90.0		
PSM 8	96	100	890	17,950	117.0	115	17
PSM 18	37	100	954	21,000	137.0		
PSM 1	90	220 ⁺	871	24,400	159.0		
PSM 3	90	220 ⁺	871	17,100	111.0*		
PSM 2	91	220 ⁺	871	28,200	184.0	175	7.7
PSM 16	37	220	954	28,850	188.0		
PSM 17	44	220	954	25,900	169.0		
PSM 4	89	300 ⁺	871	26,400	172.0		
PSM 10	114	300	890	32,700	213.0	201	9.6
PSM 15	37	300	954	33,000	215.0		
PSM 23	83	300	993	31,500	205.0		
PSM 14	29	350	932	36,700	239.0	249	5.7
PSM 13	35	350	954	39,800	259.0		

⁺ Only two rods were stressed for applying the precompression.

* This value not considered while calculating the mean.

TABLE 3.3
STRENGTH OF 1:1:4.5 MORTAR JOINTS UNDER COMPRESSION AND SHEAR

Specimen	Age (days)	Precom- pression (psi)	Mortar Strength (psi)	Failure Load (lbs)	Shear Strength (psi)	Mean (psi)	Coefficient of Variation (%)
PSM 26	28	0	2138	7,575	49	47	6.0
PSM 27	28	0	2138	6,875	45		
PSM 28	28	100	2138	21,000	137		
PSM 29	30	100	2138	19,500	127	129	6.2
PSM 36	31	100	2138	18,800	122		
PSM 30	30	220	2138	30,000	195		
PSM 31	30	220	2138	28,000	182	193	5.2
PSM 37	31	220	2138	31,000	202		
PSM 32	30	300	2138	38,800	253	244	5.5
PSM 33	30	300	2138	36,000	234		

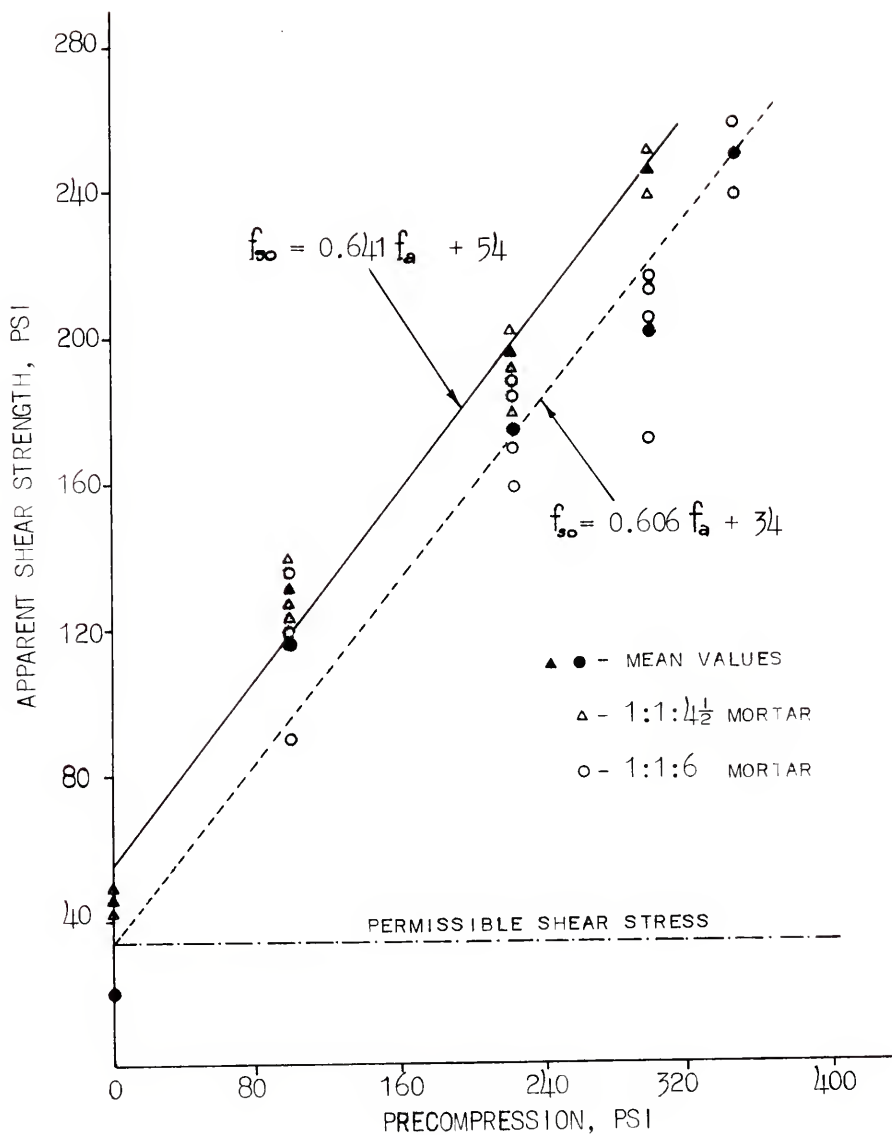


Fig. 3.4. Effect of precompression on the shearing strength of mortar joints.

shear strength due to increase in strength of mortar at higher precompressions, because the failure would likely be due to shear failure of the mortar.

Using the method of least squares, the best-fit curve for the observed data was found to plot as straight lines with the following equations:

$$f_{so} = 0.606 f_a + 34 \quad (3.1)$$

for 1:1:6 mortar, and,

$$f_{so} = 0.641 f_a + 54 \quad (3.2)$$

for 1:1:4.5 mortar.

The above equations may be used for predicting the shearing strength of mortar joints with a precompression up to 300 psi for Type M mortar when blocks having an IRA of 12 g to 17 g/min/30 sq in are used.

The specifications (2) limit the allowable shearing stress to 34 psi for Type M mortar, irrespective of the strength of mortar or level of precompression. Test results to date indicate clearly that the specifications are conservative.

TABLE 3.4
STRENGTH OF MORTAR JOINTS UNDER COMPRESSION AND BENDING

Specimen	Age (days)	Precompression (psi)	Mortar Strength (psi)	Failure B.M. (lb in)	Modulus of Rupture (psi)
PSM 5	95	0	890	3,150	27
PSM 17	37	0	954	2,150	18
PSM 25	83	150	993	26,000	222
PSM 21	43	300	954	45,000	385
PSM 24	44	300	954	48,000	410
PSM 27	28	0	2138	5,470	47
PSM 34	31	150	2138	34,000	291
PSM 35	31	300	2138	66,000	564

3.4 Strength of Mortar Joints under Compression and

Bending: The test setup shown in Figure 3.1 was modified to produce bending in the specimen with flexural stresses acting normal to the bedjoints. The load corresponding to the first crack was taken as the failure load since beyond the initial failure, the load could have been shared by the prestressing rods. Table 3.4 presents the results of the tests. The maximum bending moment corresponding to the failure load, when divided by the section modulus of the joint, yielded the value of modulus of rupture shown in Table 3.4. Adopting the cross-section of mortar joint shown in Figure 3.5, the value of section modulus corresponding to the extreme fiber was obtained as 117 cu in. The results are plotted in Figure 3.6. Failure at the joint was precipitated by a break in bond between the mortar and the blocks.

The modulus of rupture appears to increase linearly with precompression. In addition, the influence of precompression upon the modulus of rupture is significant with high strength mortar. The following empirical relations are proposed:

$$f_{bo} = 1.250 f_a + 27 \quad (3.3)$$

for 1:1:6 mortar, and,

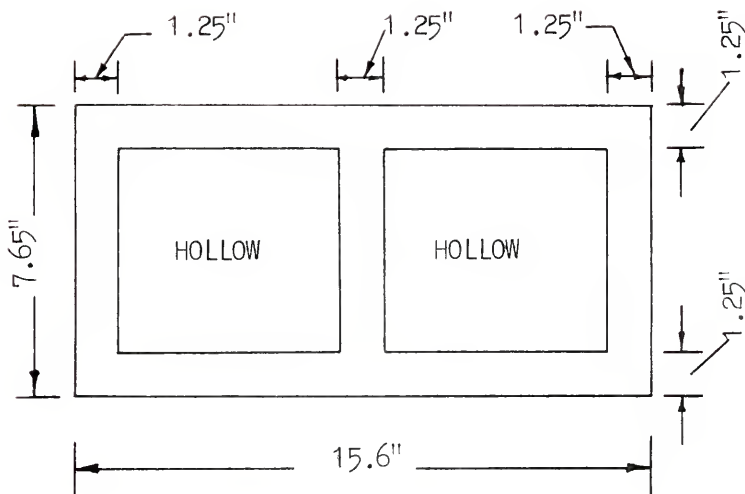


Fig. 3.5. Cross-section of a mortar joint.

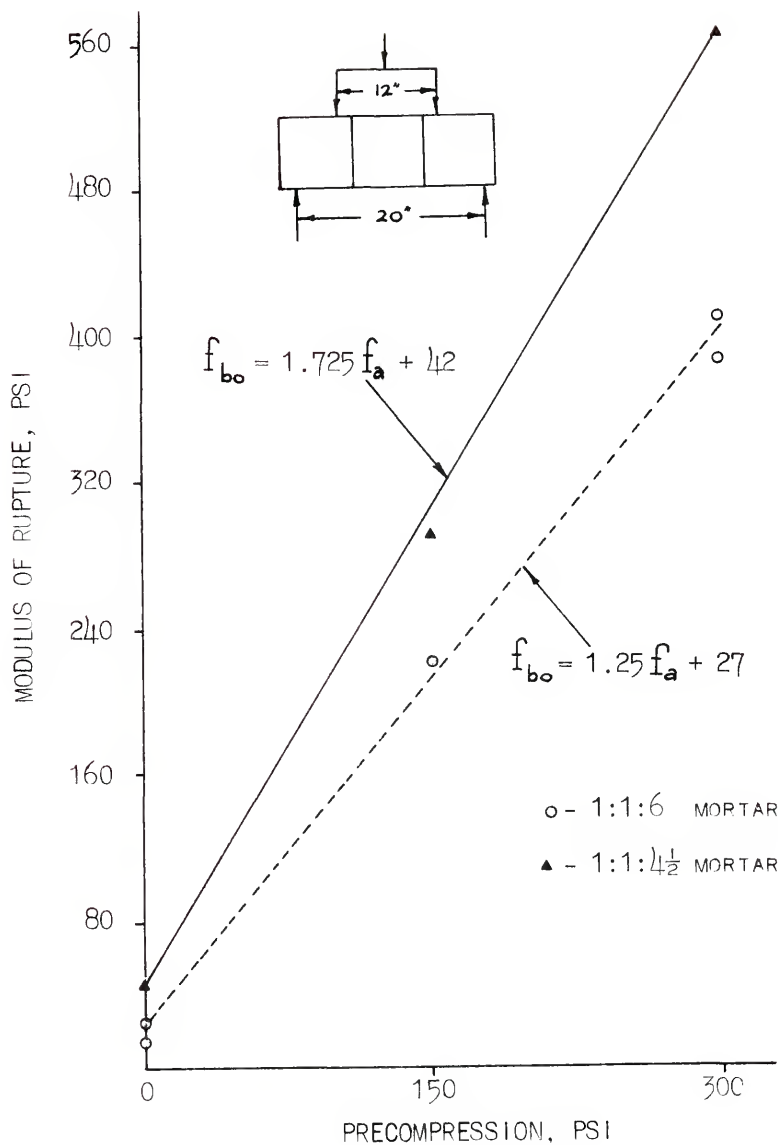


Fig. 3.6. Effect of precompression on the flexural tensile strength of mortar joints.

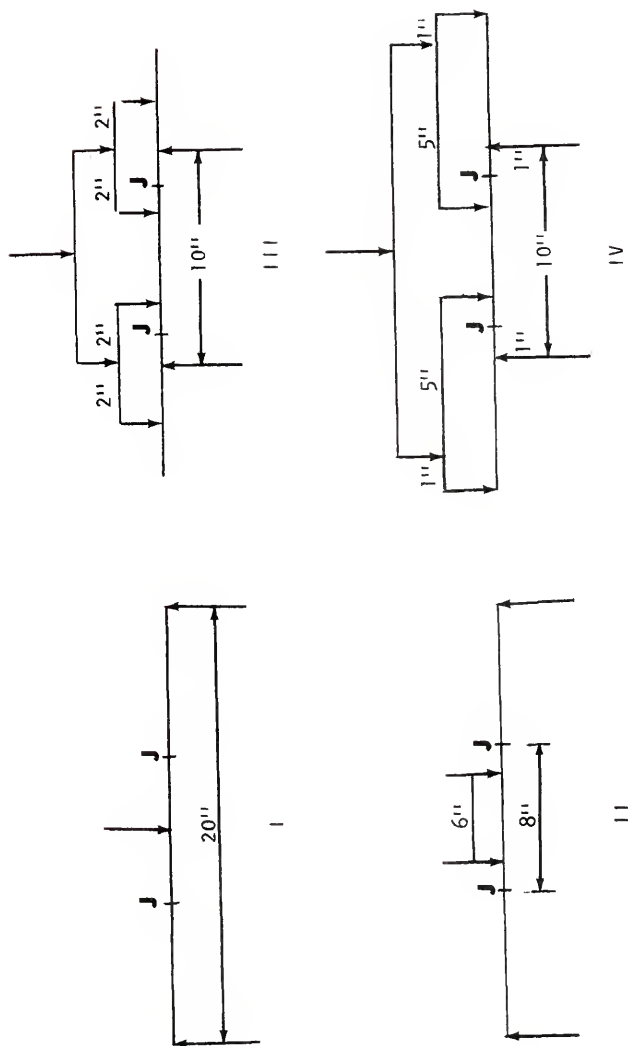


Fig. 3.7. Test setups used for obtaining combined stresses on mortar joints.

TABLE 3.5

MORTAR JOINTS UNDER COMBINED COMPRESSION, BENDING, AND SHEAR

Specimen	Age (days)	Axial Stress (psi)	Cube Strength (psi)	Test Setup	Failure Load (lbs)	f_s (psi)	f_b (psi)	f_{so} (psi)	f_{bo} (psi)	$\frac{f_s}{f_{so}}$	$\frac{f_b}{f_{bo}}$
PSM 19	43	300	964	I	12,600	103	323	200	397	0.515	0.821
PSM 40	27	300	956	II	13,800	113	354	200	397	0.561	0.890
PSM 39	27	300	956	III	46,000	188	99	200	397	0.936	0.248
PSM 41	28	300	956	IV	26,000	36	352	200	397	0.177	0.887
PSM 43	28	300	1758	II	17,000	139	436	244	564	0.567	0.774
PSM 44	28	300	1758	III	57,500	234	123	244	564	0.960	0.218
PSM 42	28	300	1758	IV	32,000	43	432	244	564	0.178	0.770

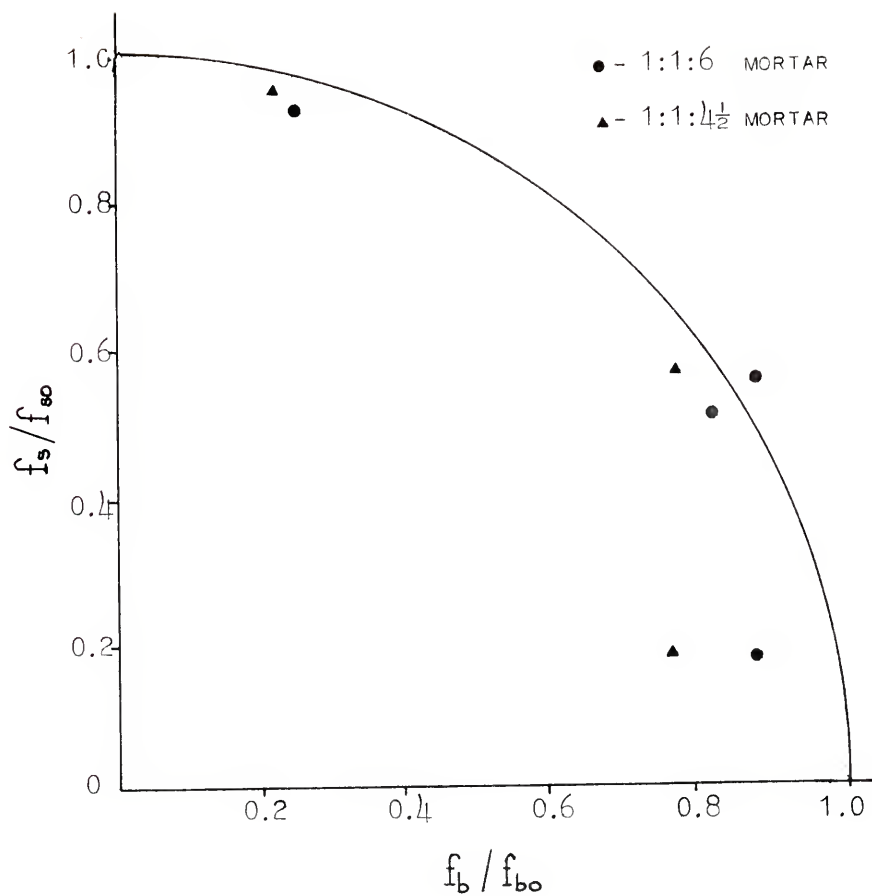


Fig. 3.8. Interaction of bending and shear under constant precompression.

$$f_{bo} = 1.725 f_a + 42 \quad (3.4)$$

for 1:1:4.5 mortar.

Here, also, the specifications are conservative in limiting the allowable stress to 23 psi.

3.5 Combined Compression, Bending, and Shear: Various test arrangements were devised to produce several combinations of bending and shear under a constant precompression of 300 psi. These testing arrangements are shown schematically in Figure 3.7, and the results are summarized in Table 3.5. Knowing the mean value of modulus of rupture at a precompression of 300 psi (f_{bo}), also the shear strength (f_{so}) without flexure, and the combined bending and shearing stresses (f_b and f_s), the values of f_b/f_{bo} and f_s/f_{so} can be calculated and plotted to provide the unit interaction curve shown in Figure 3.8. It is anticipated that this curve is one from a family of curves that will be generated by varying the precompression in an expanded program of testing. Thus, the flexural and shearing stresses in a mortar joint under combined loading can be assumed to follow the equation:

$$\left(\frac{f_s}{f_{so}}\right)^2 + \left(\frac{f_b}{f_{bo}}\right)^2 = 1 \quad (3.5)$$

CHAPTER 4

MODEL TESTS OF CONCRETE MASONRY PIERS

4.1 Selection of Model: The problem under investigation consists of determining the stress distribution in a concrete masonry shear wall, particularly in the region between openings called piers. Even if models were used, it is not economical to fabricate a model for a multiple story wall with a large number of openings. Schneider (46) conducted a photoelastic analysis on plastic models with configurations as shown in Figure 4.1. The loads were applied either diagonally or horizontally for all configurations except in the case of multiple pier models where the load was applied in a manner simulating the way in which a roof diaphragm would load a shear wall. A similarity in fringe patterns was found to exist between the model walls containing several piers and a diagonally loaded single pier. Accordingly, the test specimen was chosen as described in subsection 1.3.9 of Chapter 1.

In this investigation, a linear plane stress finite element analysis is adopted in lieu of a photoelastic analysis to verify the above findings and also to check the effect of pipe columns that have been used to maintain the geometry of the openings. The configurations chosen

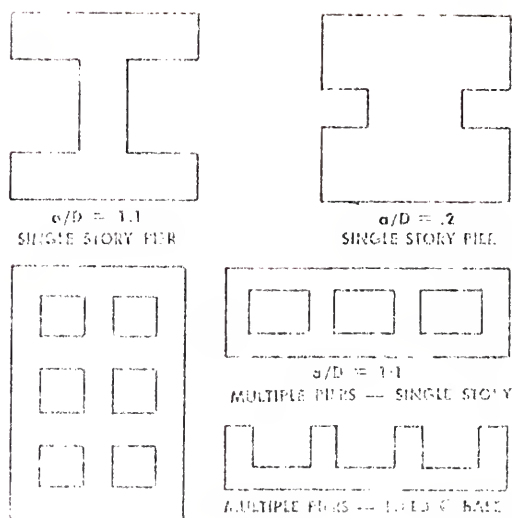


Fig. 4.1. Photoelastic model configurations chosen by Schneider.

for analysis and the finite element idealization are shown in Figures 4.2 through 4.5. Figure 4.4 shows the pier in a story with openings and walls on either side of it, but loaded diagonally; Figure 4.5 shows the configuration adopted by Schneider. In this case, the pipe columns are idealized as an equivalent rectangular element. The equivalent modulus of elasticity of the element is calculated by equating the axial rigidities of the actual pipe column with that of the idealized element. In a photoelastic analysis, the fringe patterns represent the lines joining the points of constant maximum shear stress, also called isoshear lines. In the analysis, maximum shear stresses are computed at centroids of all elements. The contour lines for these values represent the isoshear lines. The isoshear lines are plotted for all the piers investigated and these are shown in Figures 4.6 through 4.11. It is evident that the fringe patterns in all the above cases are very similar and this confirms the method of loading adopted in a single pier to simulate the actual loading conditions a pier in a wall is subjected to.

To check the effect of substituting pipe columns for end piers (Figure 4.4), the modulus of elasticity of the pipe column elements was arbitrarily increased by 100%. However, the corresponding changes in the maximum stresses in the pier were less than 1% of the previous values.

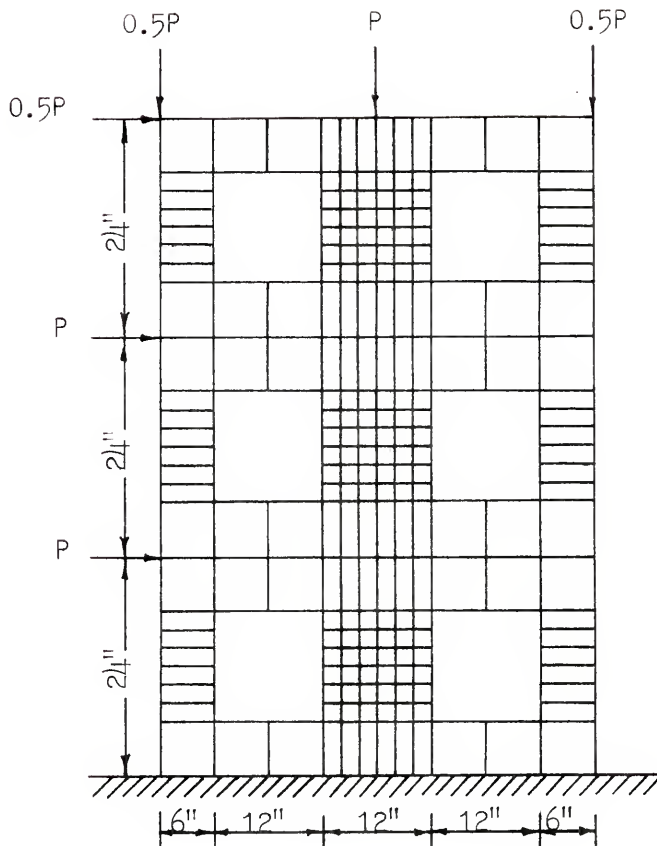


Fig. 4.2. Finite element idealization for a shear wall with openings.

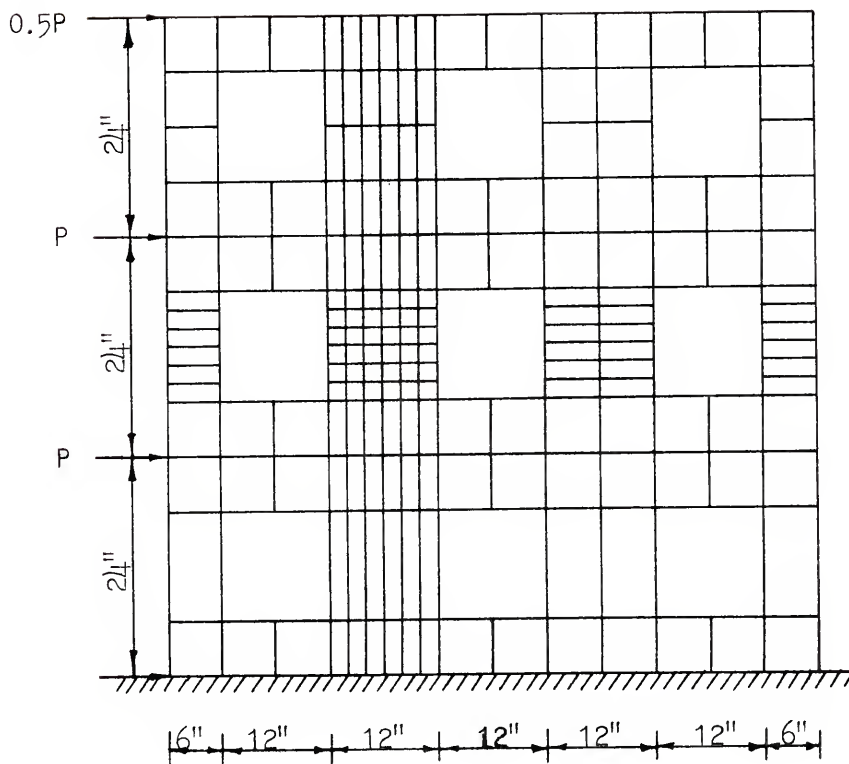


Fig. 4.3. Finite element idealization for a multiple pier shear wall.

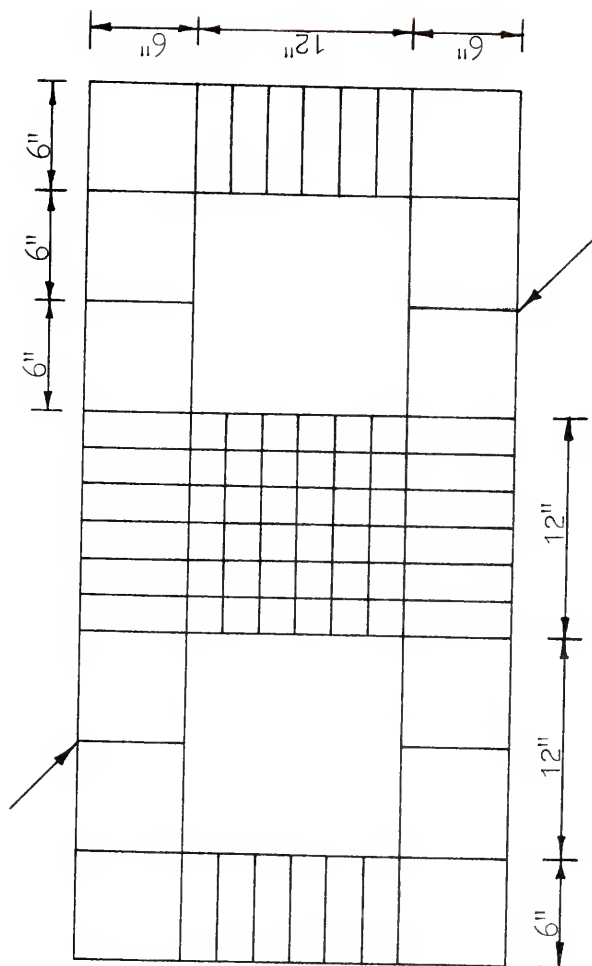


Fig. 4.4. Finite element idealization for a pier with openings and walls on either side.

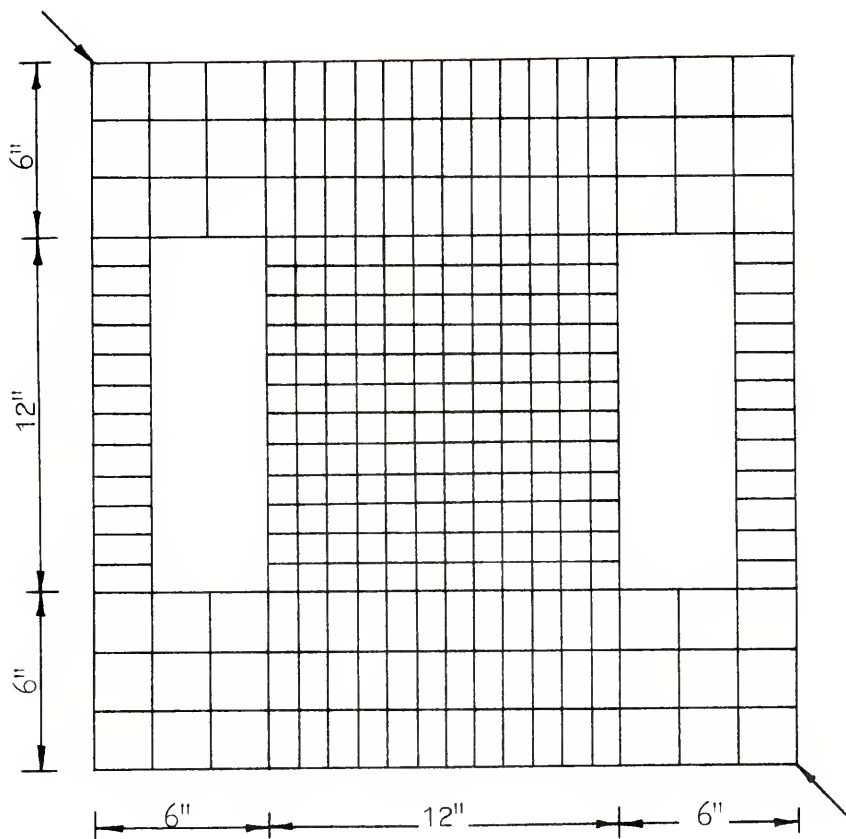


Fig. 4.5. Finite element idealization for the test specimen adopted by Schneider.

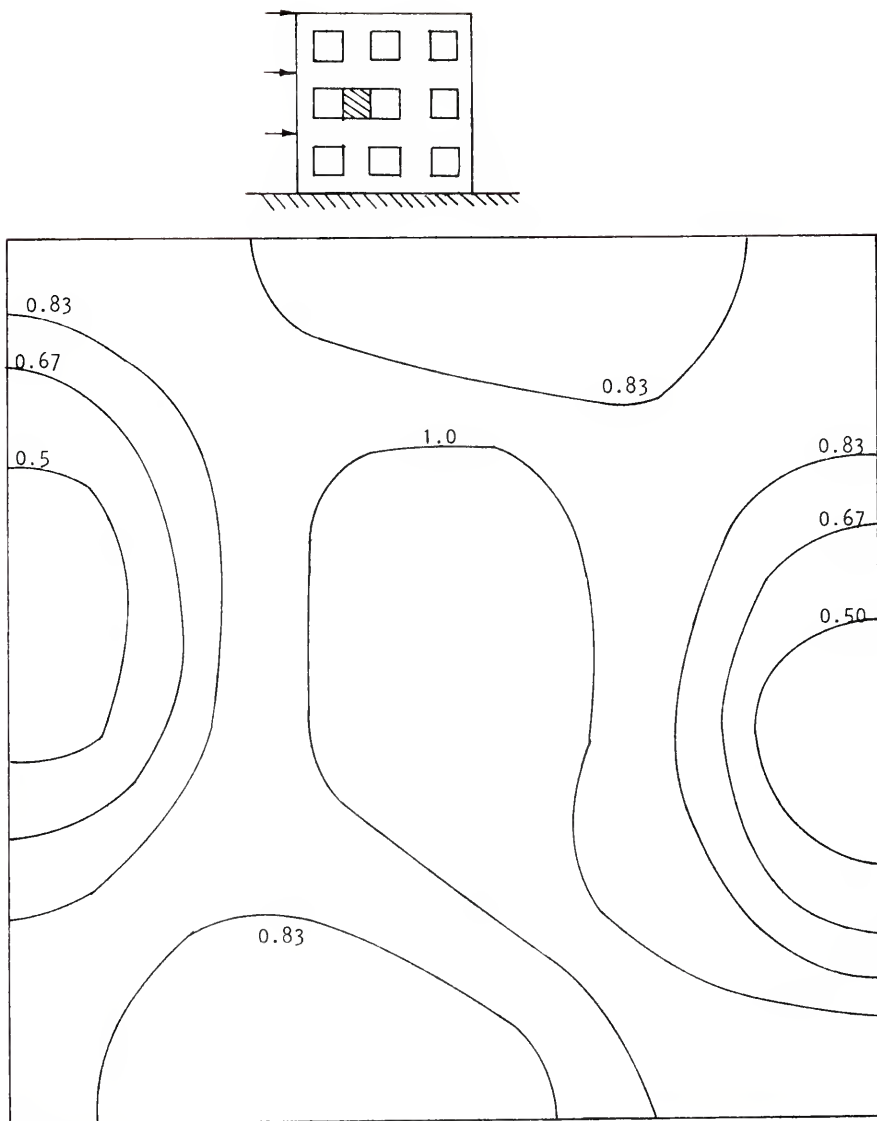


Fig. 4.6. Isoshear lines for the pier shaded as shown above.

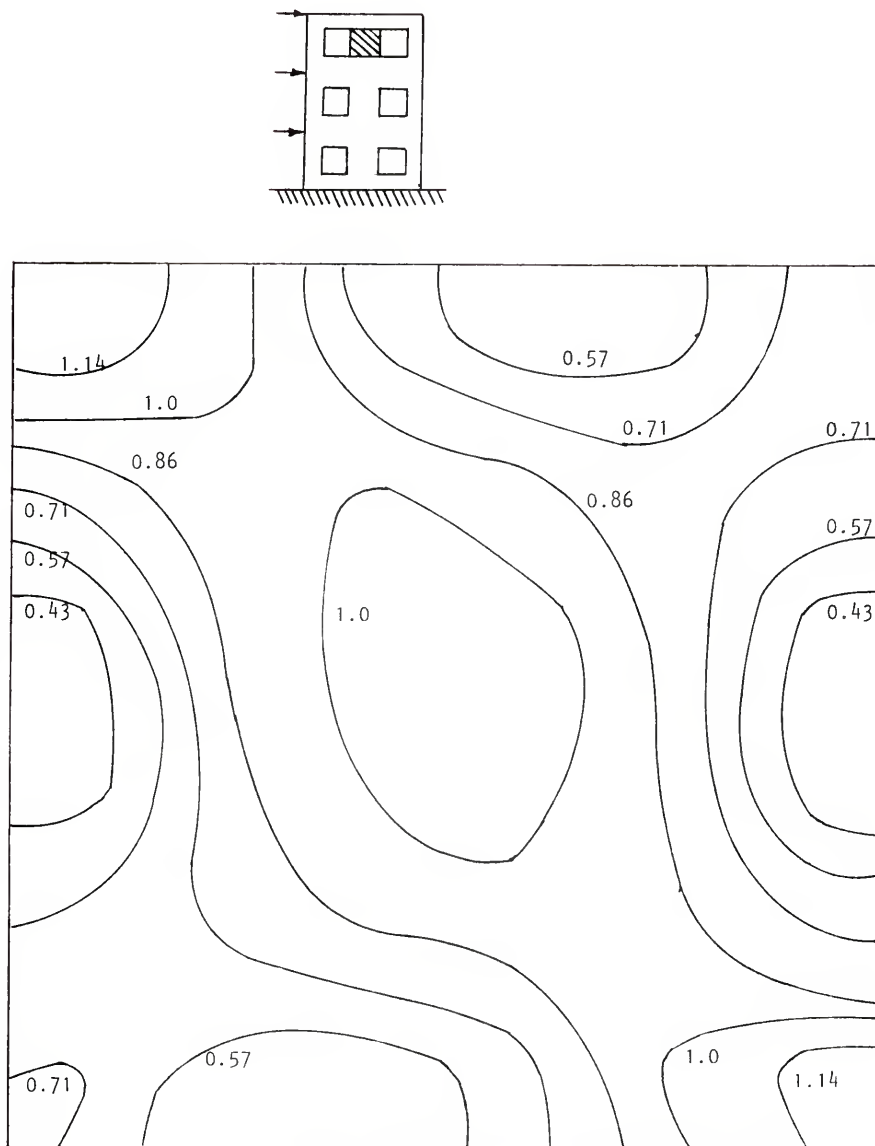


Fig. 4.7. Isoshear lines for the pier shaded as shown above.

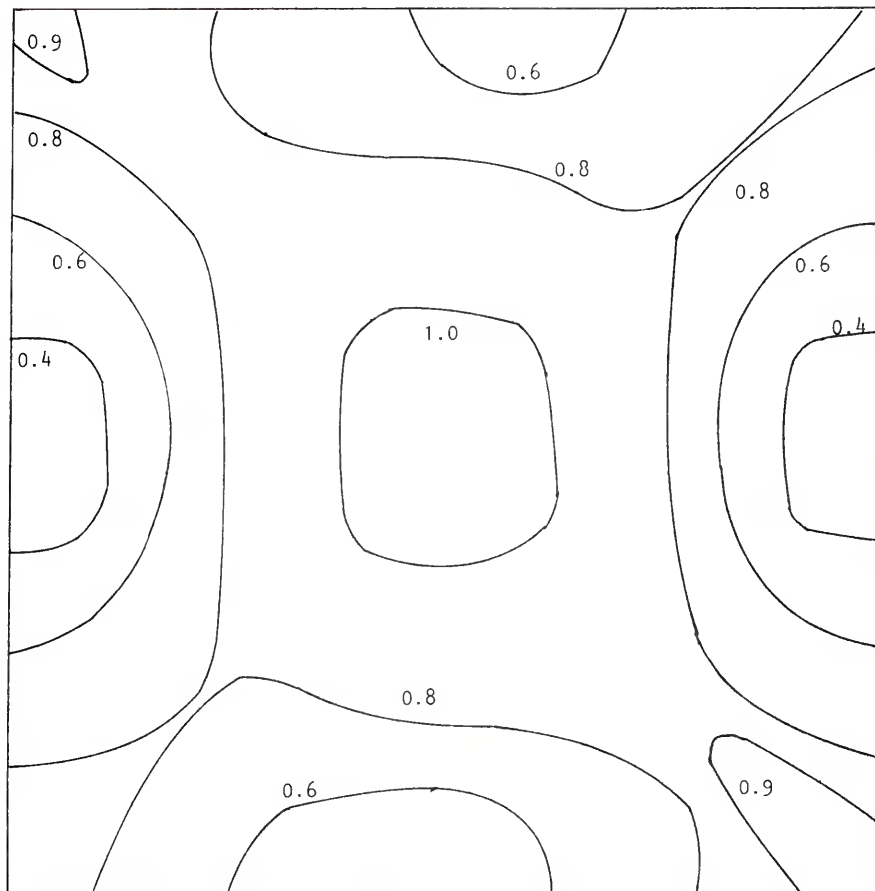
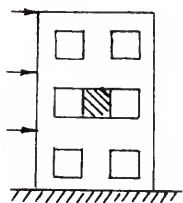


Fig. 4.8. Isoshear lines for the pier shaded as shown above.

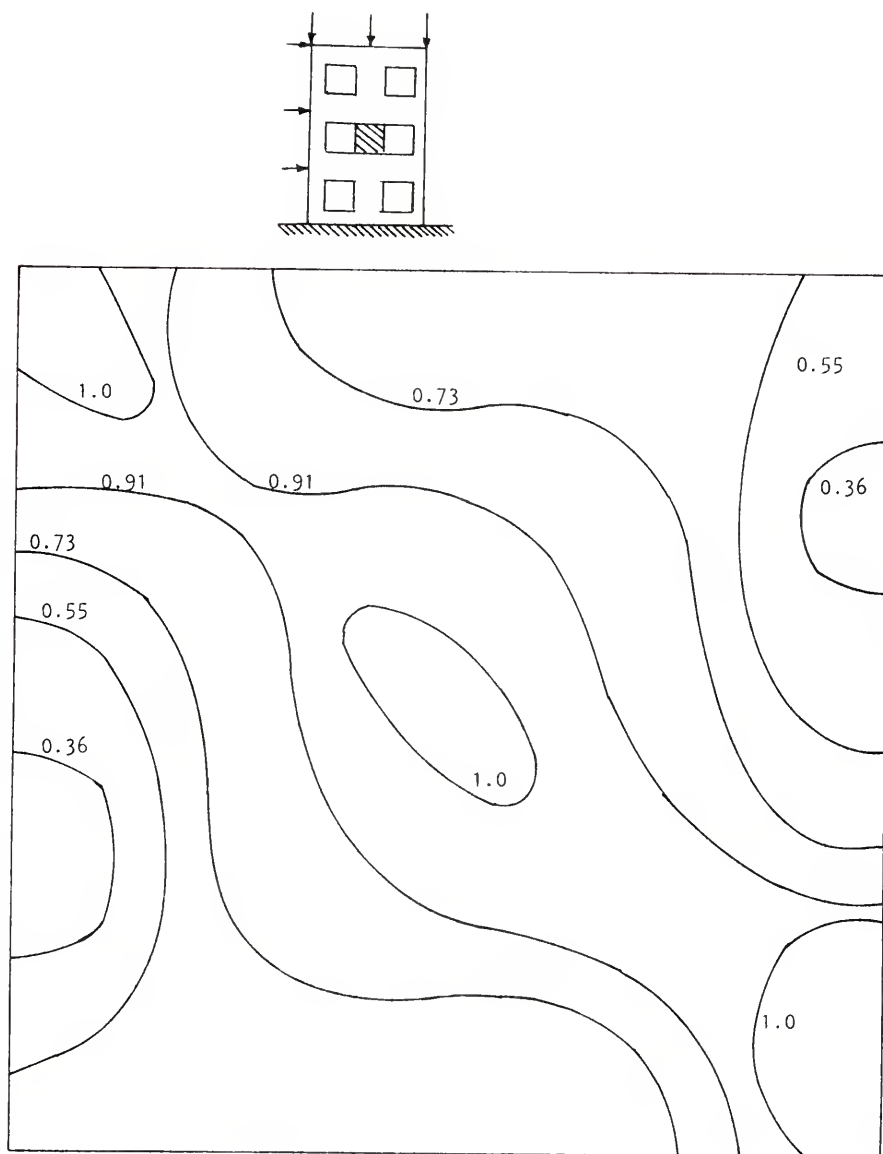


Fig. 4.9. Isoshear lines for the pier shaded as shown above.

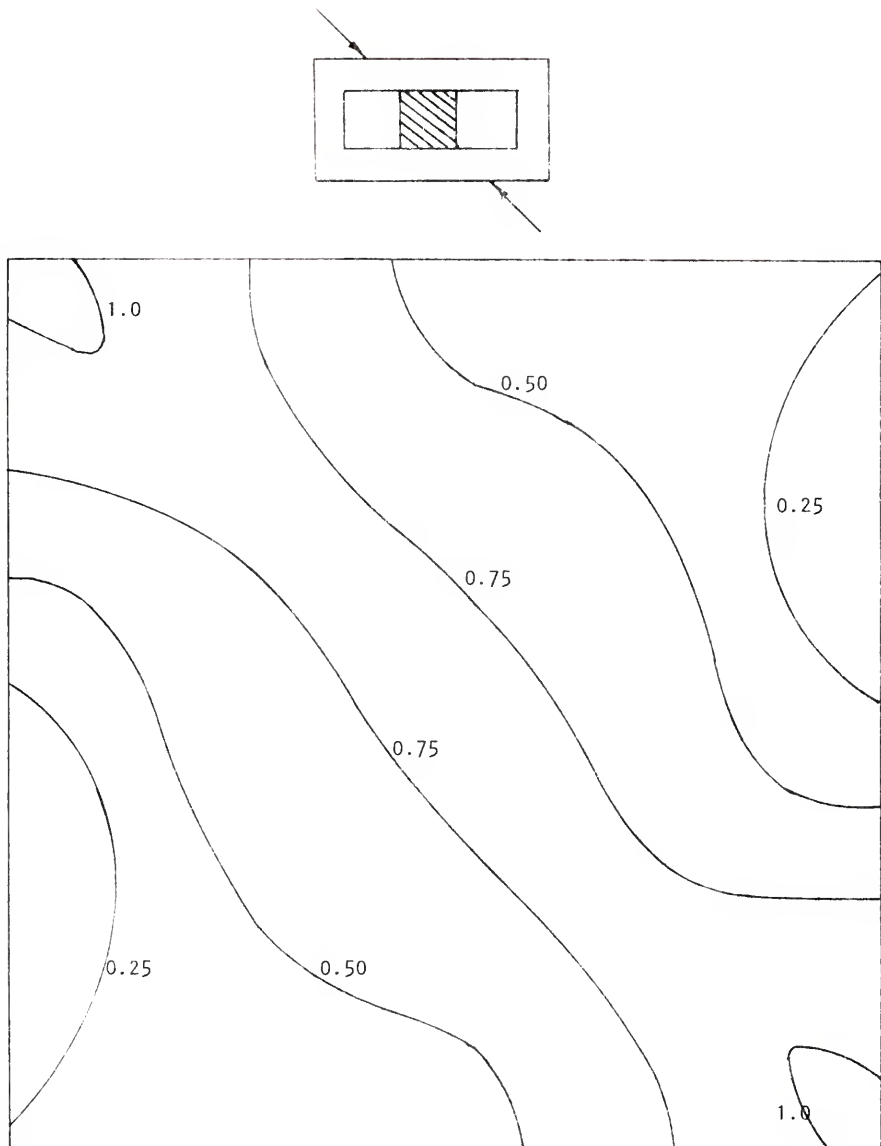


Fig. 4.10. Isoshear lines for the pier shaded as shown above.

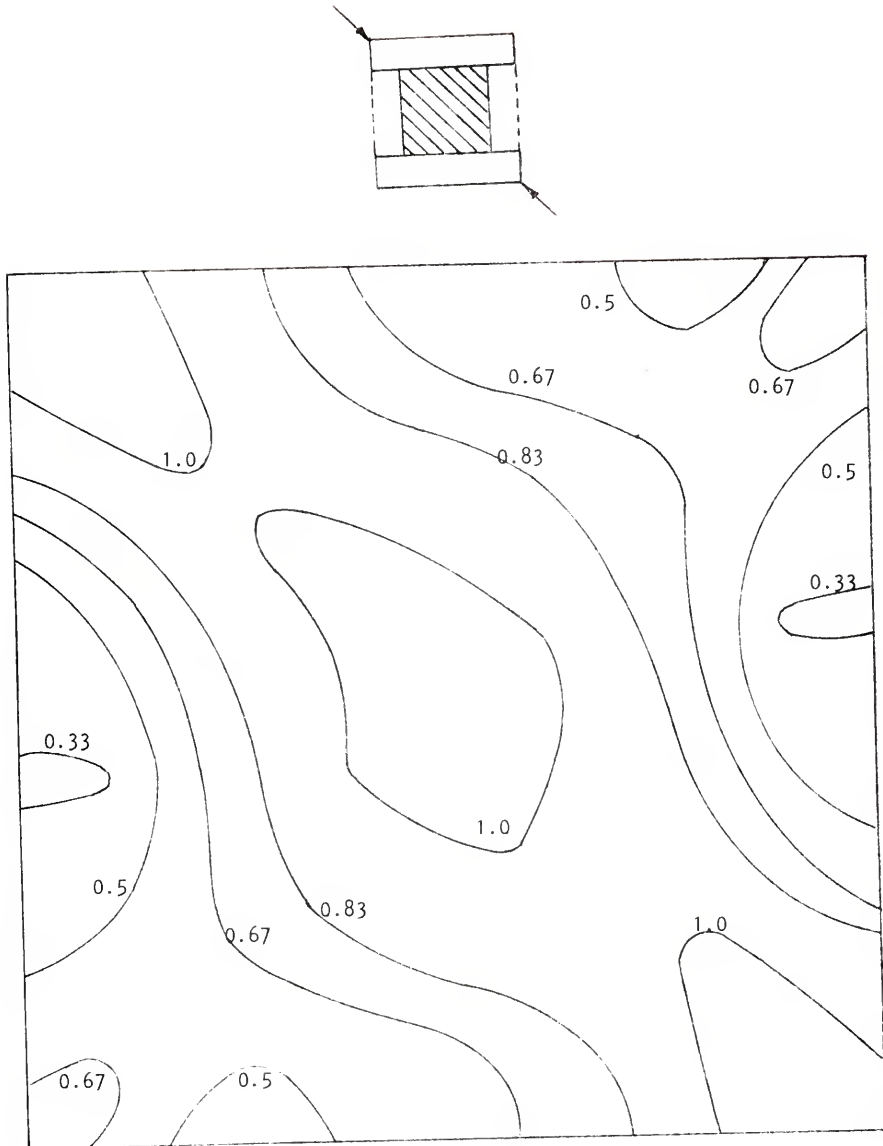


Fig. 4.11. Isoshear lines for the pier shaded as shown above.

On the basis of the preceding findings, the model configuration shown in Figure 4.12 was adopted. The present investigation is restricted to a pier having a shear-span/depth ratio of 0.5.

4.2 Selection of Model Materials: The materials used in the construction of a model structure depend upon the type of test to be made on the model. Inelastic models should be constructed of materials which simulate the physical properties as closely as possible in all respects (26) (38). The selection of a model material to simulate concrete requires the selection of a cementitious material with a stress-strain curve up to failure that is homologous to that of concrete, and with Poisson's ratio, ratio of tensile strength to compressive strength, and shrinkage equal to the counterpart prototype properties (40) (9). Previous research (40) indicates that it is not possible to obtain a model material corresponding to prototype concrete by merely scaling the individual components, e.g., coarse and fine aggregates, cement, and the admixtures. However, as long as the overall physical properties of the model material, such as the stress-strain curve and the failure envelope, are compatible with those of the prototype concrete according to the laws of similitude, it does not matter how these properties are obtained (54).

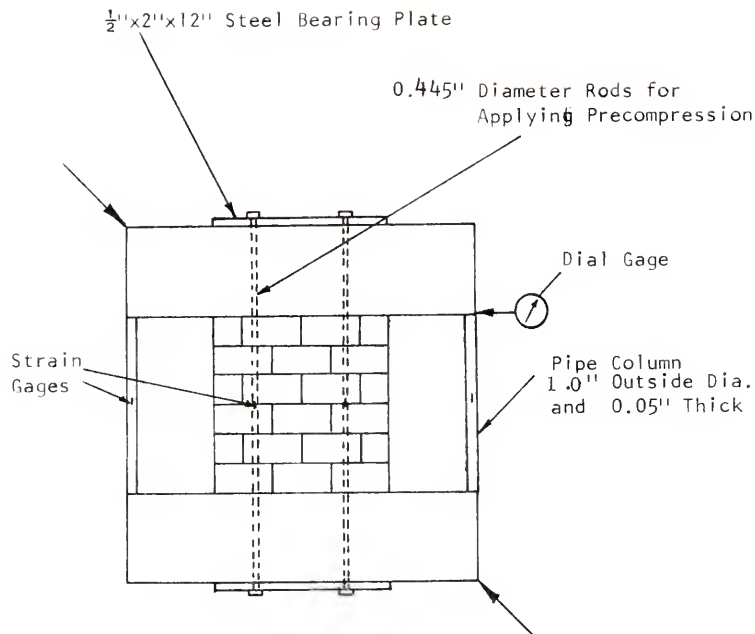


Fig. 4.12. Schematic test setup for finding the shearing strength of a pier.

In this investigation, model concrete blocks one-fourth the size of the full size blocks were used. The physical and mechanical properties of the block have already been described in Chapter 2. While the stress-strain curves and strengths of the model blocks are comparable to the prototype blocks available in the market, their absorption characteristics differ widely from those of the prototype blocks. Because of their higher absorption, the water in the mortar was absorbed when placed on a dry block, impairing the workability of the mortar. Hence, the model blocks were prewetted before placing the mortar.

The types of mortar used and their components are described in Section 2.6 of Chapter 2. To cope with the increased absorption of the blocks and reduced thickness of joints in the model specimens, an increase in the initial flow of mortar was needed. This resulted in reduced strength of mortars used in the model specimens compared to the strengths of corresponding types of mortars used in the investigation described in Chapter 3. Since it is the amount of aggregate and not the gradation that has the greatest effect on the mechanical properties of mortar (40), no attempt was made to model the mortar sand on the basis of the grading curve.

The details of the grout mixes used and their properties are given in Chapter 2. The grout strength and

its fluidity without separation of grout components were the factors governing the choice of the mixes adopted.

The model reinforcing steel exhibited a higher yield strength than the normal grades of steel used in practice. Since this investigation is mainly on nonreinforced walls and the vertical reinforcing in end cells do not contribute appreciably to the strength of the pier, this deviation is not considered important. The depressions in the bar simulate to a certain extent a deformed bar. However, no attempt was made to simulate bond characteristics. Workmanship is an important factor in masonry which cannot be modelled.

4.3 Fabrication of Model: As the model concrete blocks are one-fourth full size, the individual pier was modelled to represent a story height of 8' 0". Because of the limitations of available space in the testing machine which was suitable for testing models, the height of the model was restricted to 2' 0" representing a story height of 8' 0". Since the region of interest is the pier, it was decided to use cement mortar (1:3 by weight) for the spandrel portion to economize the use of blocks. The thickness of mortar joints varied between 0.125" to 0.15". The dimensions of the model are shown in Figure 4.13.

The blocks were soaked in water for a minute and then wiped clean with paper towels and allowed to dry for about

ten minutes. The mortar was mixed to an initial flow of about 120%. Mortar was applied to the web as well as the face shells of the block. Also, the vertical joints extended to the full thickness of the blocks. After each course was laid, the mortar protruding in the cells was removed so as to facilitate proper grouting later. After the six courses of blocks were laid, the pier was allowed to cure in air for twenty-four hours. The pier was placed on a wooden plank and the vertical reinforcing bars were inserted through holes corresponding to the centers of the end cells in the pier, and projecting 6" at top and bottom of the pier. The grout was then poured in the cells and well tamped. In the case of hollow piers, only the end cells were grouted. After being allowed to cure in air for twenty-four hours, this assembly was placed horizontally in a wooden mold to form the 2" x 6" x 24" spandrels. The spandrel beam was reinforced as shown in Figure 4.13. Steel angles 1-1/4" x 1-1/4" x 1/4" two inches long were placed at the loaded corners to avoid local crushing of the specimen. The spandrel concrete consisting of one part of Portland Cement to three parts of sand by weight with a water-cement ratio of 0.55 was poured. Moist cloths were kept over the spandrel surface to avoid shrinkage cracks. The formwork was removed after three days and the specimen allowed to cure in air until testing.

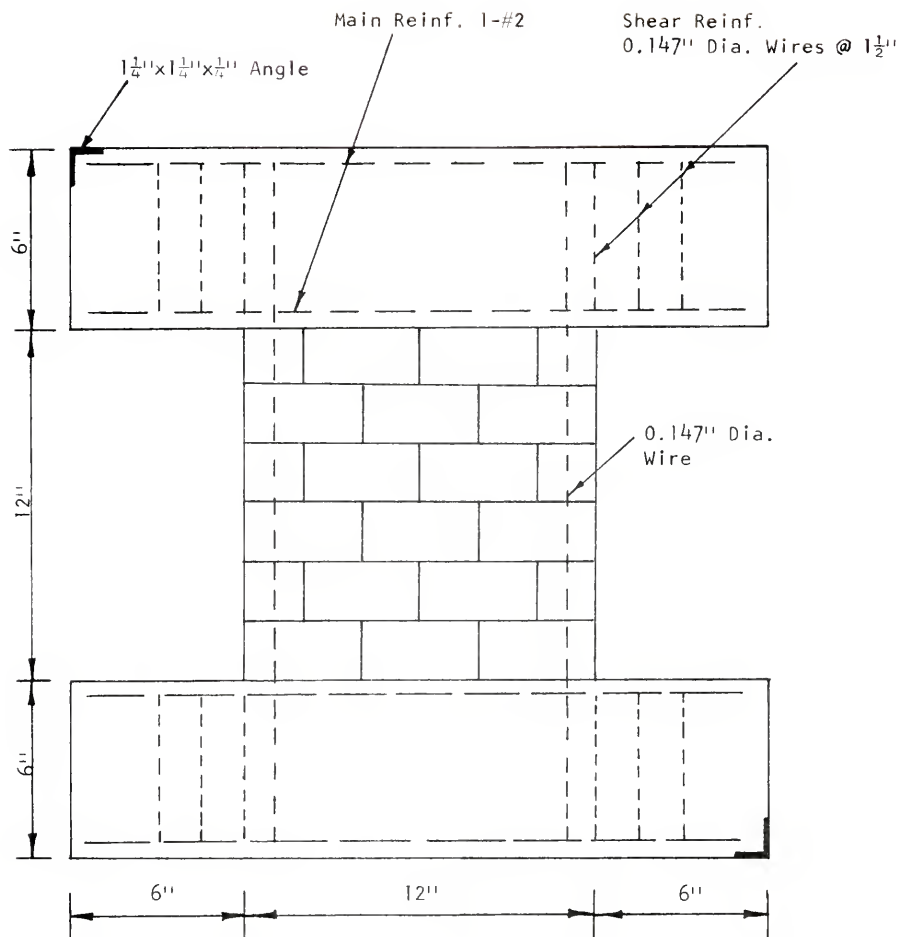


Fig. 4.13. Details of pier model.

In the case of hollow piers, holes were left in the spandrel beam for insertion later of prestressing rods (Figure 4.12). This was accomplished by inserting steel tubes wound with greased paper before pouring the mortar.

4.4 Test Setup: The test setup adopted is shown in Figures 4.12 and 4.14. The pipe columns were used to maintain the geometry of the openings. They consisted of two steel tubes 1.0" in outside diameter and 0.05" thick. Two strain gages were mounted diametrically opposite to each other at the center of each pipe column and connected in series to measure the load taken by the column. The gages were previously calibrated for the strains corresponding to the axial load on the column. The deflection at the corner of the spandrel is measured in a direction parallel to the soffit of the spandrel beam as shown in Figure 4.12. This would correspond to the horizontal deflection of the pier had the pier been placed vertically and the load applied diagonally.

In the case of hollow piers subject to external precompression, the compressive stress was applied by tightening two steel rods, 0.445" in diameter, threaded at the ends. Two bearing plates, 1/2" x 2" x 12", were used to distribute the load uniformly over the cross-section of the pier. Two strain gages were mounted



Fig.4.14. Model test on pier

diametrically opposite to each other on each rod and connected in series to measure the axial force in the rod.

4.5 Test Parameters: In earlier studies by Schneider, the main parameters considered were the shear-span to depth ratio, the effect of reinforcement and constant external precompression, on different pier configurations. In this investigation, only one pier configuration was considered. This study was designed to:

- 1) find the influence of different types of mortar and grout on the shear strength of a grouted pier, and
- 2) ascertain the effect of different magnitudes of precompression on the strength of nongrouted piers.

The mechanical properties of mortar and grout used are described in Chapter 2.

4.6 Tests on Grouted Piers: Three different types of grout and two types of mortars were used in this test series. In all the cases, the failure occurred by diagonal tensile cracking along the vertical diagonal, the first crack occurring near the center of the pier at about 85% of the ultimate load. The diagonal crack then progressed quickly towards the corners. In no case did complete collapse occur even after large cracks had opened up completely through the pier. The failure patterns of piers with strong mortar joints and different types of grout are shown in Figures 4.15 through 4.17. The failure



Fig. 4.15. Failure pattern of PR 4
strong mortar, weak grout.

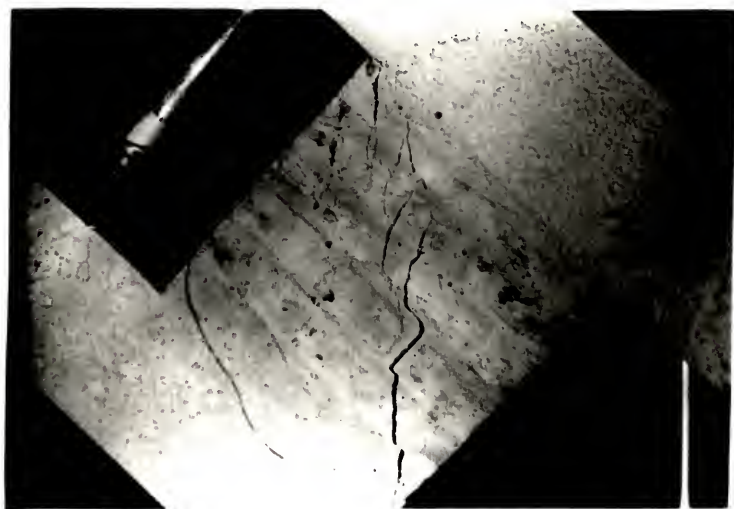


Fig. 4.16. Failure pattern of PR 3
strong mortar, medium grout.

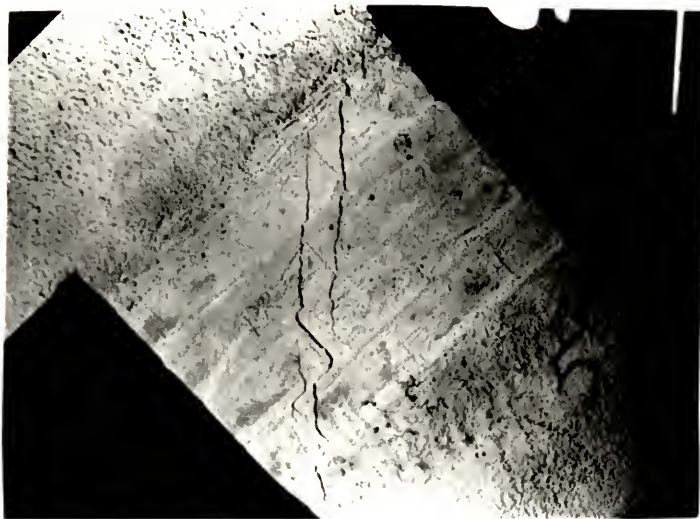


Fig. 4.17. Failure pattern of PR 5
strong mortar, strong grout.



Fig. 4.18. Failure pattern of PR 9
weak mortar, weak grout.



Fig. 4.19. Failure pattern of PR 10
weak mortar, medium grout.



Fig. 4.20. Failure pattern of PR 7
weak mortar, strong grout.

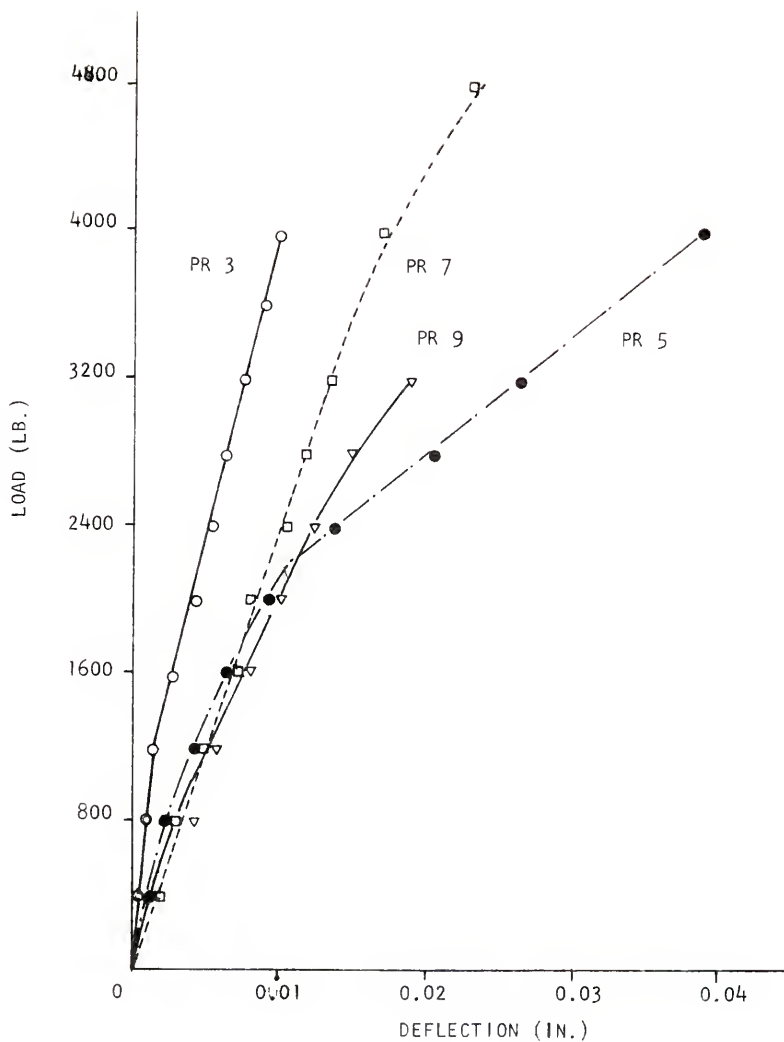


Fig. 4.21. Typical load-deflection curves for grouted piers.



Fig. 4.23. Failure pattern of PR 23 weak mortar, precompression 125 psi.

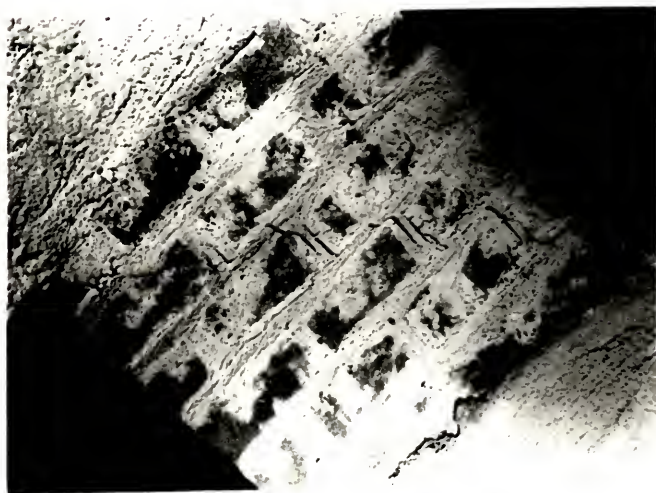


Fig. 4.22. Failure pattern of PR 13 weak mortar, precompression 50 psi.



Fig. 4.24. Failure pattern of PR 17
weak mortar,
precompression 200 psi.

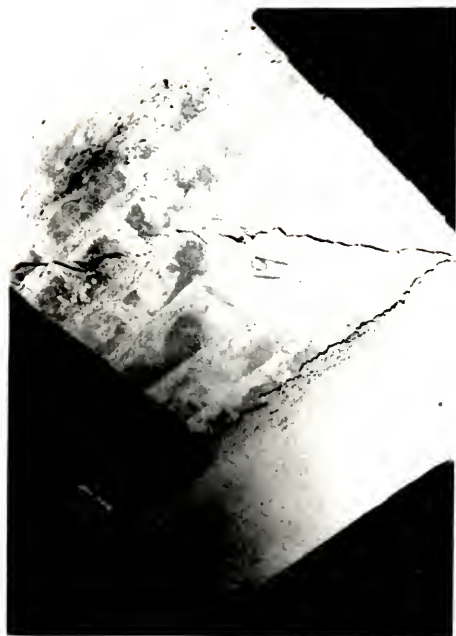


Fig. 4.25. Failure pattern of PR 19
strong mortar, precompression 50 psi.



Fig. 4.26. Failure pattern of PR 21
strong mortar,
precompression 125 psi.



Fig. 4.27. Failure pattern of PR 20
strong mortar,
precompression 200 psi.

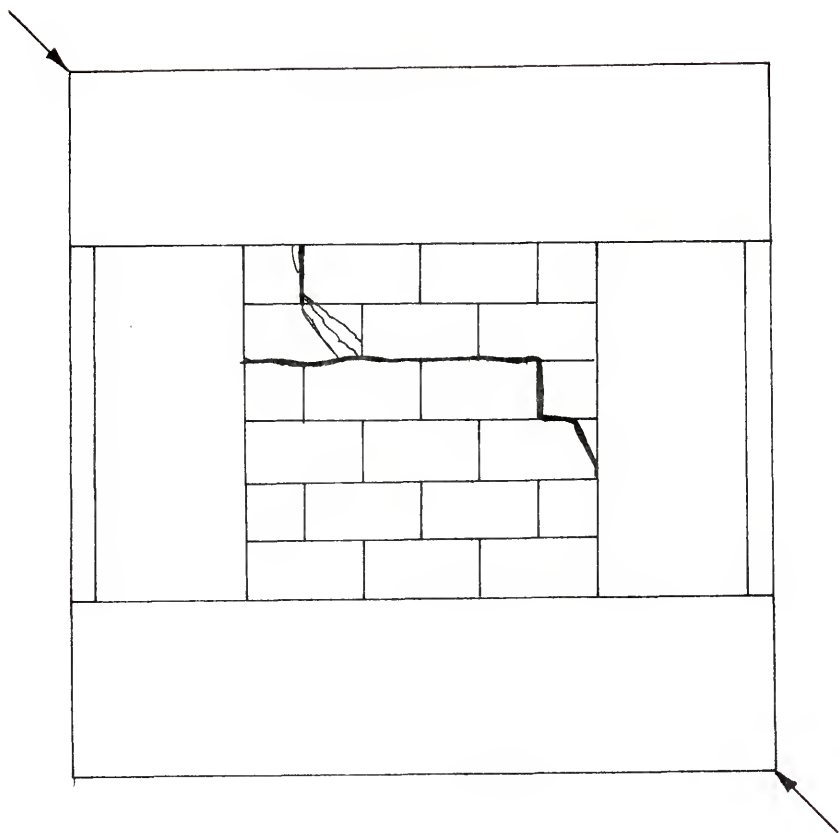


Fig. 4.28. Failure pattern of hollow pier PR 1
(strong mortar).

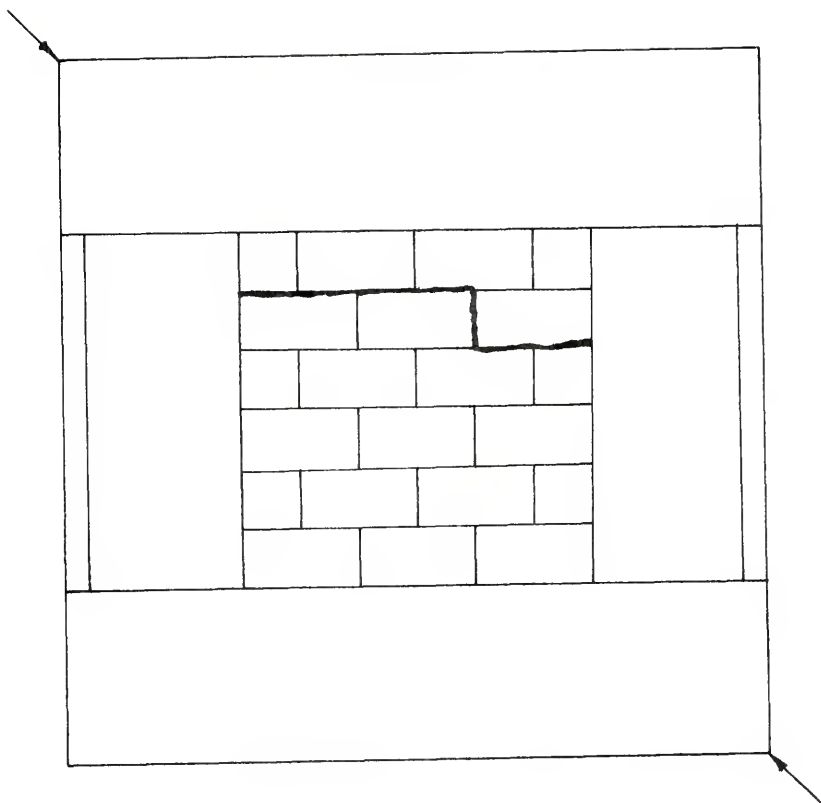


Fig. 4.29. Failure pattern of hollow pier PR 6
(weak mortar).

patterns of piers with weak mortar joints are shown in Figures 4.18 through 4.20. Typical load deflection curves are shown in Figure 4.21. For each test, two corresponding three-block grouted prisms, three mortar cubes, three grout cubes, and a model concrete block were tested in axial compression.

4.7 Tests on Nongrouted Piers: In order to study the effect of external precompression on nongrouted piers with weak and comparatively strong mortar joints, piers were tested at precompressions of 0, 50, 125, and 200 psi. It was found that in the case of piers with weak mortar joints, the failure was always initiated by debonding of mortar joints irrespective of the value of precompression imposed. However, the piers with stronger mortar joints failed by diagonal tensile cracking along the vertical diagonal at precompressions above 50 psi. In all the cases where external precompression was applied, the joints near the center of the pier failed first and the crack extended towards the corners. The failure patterns are shown in Figures 4.22 through 4.27. Figures 4.28 and 4.29 show the mode of failure of a pier with strong and weak mortar joints, respectively, when no external precompression was applied. In no case was a complete collapse of the whole specimen observed after attainment of the maximum load.

The tests results are presented in the next chapter.

CHAPTER 5
ANALYSIS OF TEST RESULTS

5.1 Grouted Piers: Table 5.1 presents the results of the tests on grouted piers. The ultimate shear strength of the pier was calculated as the average shear stress over the gross area of the pier as:

$$f_s = H/tD \quad (5.1)$$

where H equals the horizontal component of the ultimate load in lbs ($P_u/\sqrt{2}$), t equals the thickness of wall in inches (1.9"), D equals the overall depth of the pier in inches (12"), and f_s equals the average shear stress over the cross-section of the pier (psi).

Figure 5.1 shows the plot between the square root of the prism strength (f_m') and the average shear stress on the pier. Using the method of least squares, the best-fit curve for the observed data was found to plot as a straight line yielding the following relation:

$$f_s = 3.8 \sqrt{f_m'} \quad (5.2)$$

TABLE 5.1
TEST RESULTS OF GROUTED PIERS

Specimen	Age at Test (days)	Mortar Strength (psi)	Flow (%)	Cube Strength of Grout (psi)	Prism Strength (psi)	$\sqrt{f'_m}$	Ultimate Load (P_u) (lbs)	Shear Stress (f_s) (psi)
PR 2	29	1310	118	283	771	27.8	3,700	116
PR 3	30	1695	119	1000	1491	38.0	4,740	149
PR 4	30	1302	130	475	1170	34.2	3,230	101
PR 5	28	1438	120	1360	1751	41.8	4,640	146
PR 7	31	955	124	1850	1834	42.8	5,600	176
PR 9	32	905	124	558	1073	32.8	3,350	105
PR 10	31	881	120	1163	941	30.7	3,700	116

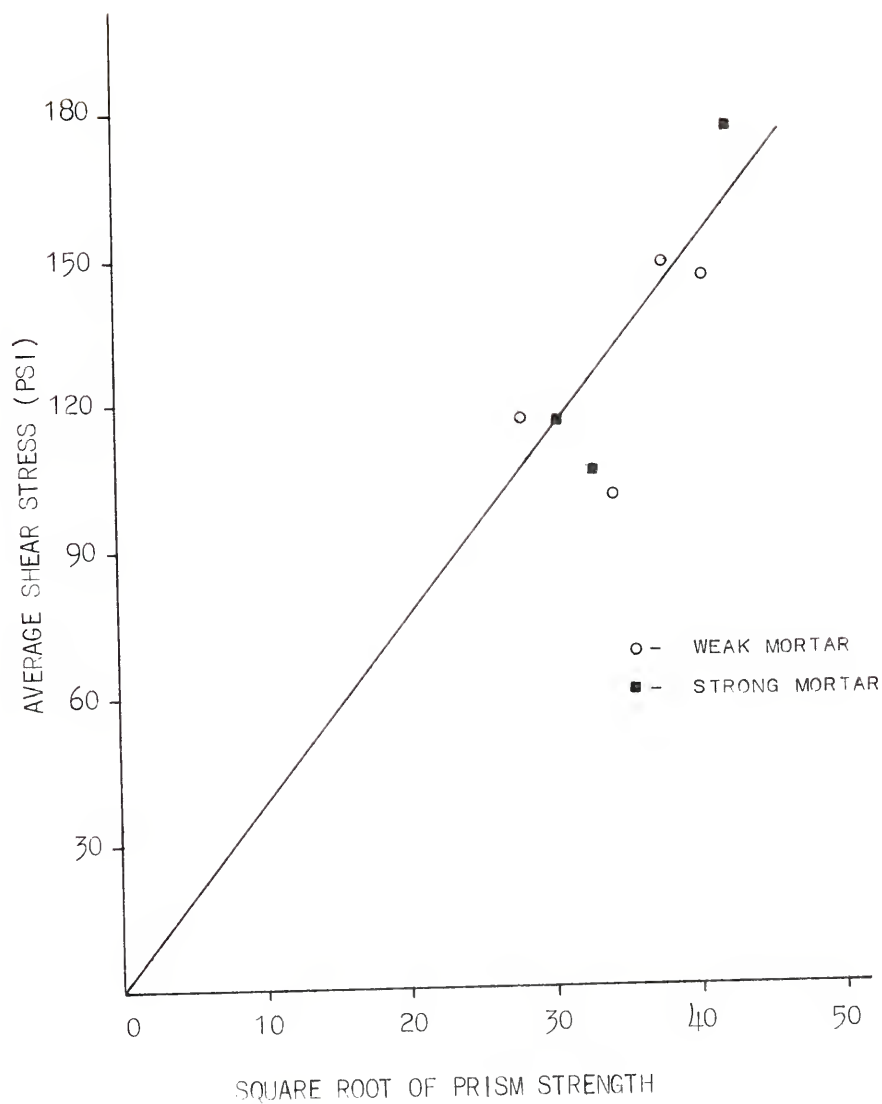


Fig. 5.1. Relation between average shear stress and square root of prism strength for grouted piers.

Figure 5.2 shows the plot between f_m' and f_s which yields the relation:

$$f_s = 20 + 0.0829 f_m' \quad (5.3)$$

It is not possible to attach any physical significance between the failure of a grouted prism in axial compression and a grouted pier in diagonal tension. However, so long as the mortar and grout are of strengths used in this investigation, Equation (5.2) could be used as an empirical equation to assess the diagonal tensile strength of grouted masonry piers.

It can also be noted that the strengths of the piers with weak and strong mortar joints, but with the same strength of grout, are not appreciably different.

5.2 Nongrouted Piers: The ultimate shear stress in the case of a nongrouted pier is calculated on the basis of the net area of the cross-section shown shaded in Figure 5.3. The applied precompression was also based on this area only. Since the load is applied diagonally, the vertical component of the load would contribute an internal compressive stress in addition to the external precompression applied. The internal precompressive force is the vertical component of the load less the load taken by the pipe columns. It is assumed that both the compressive stresses are uniformly

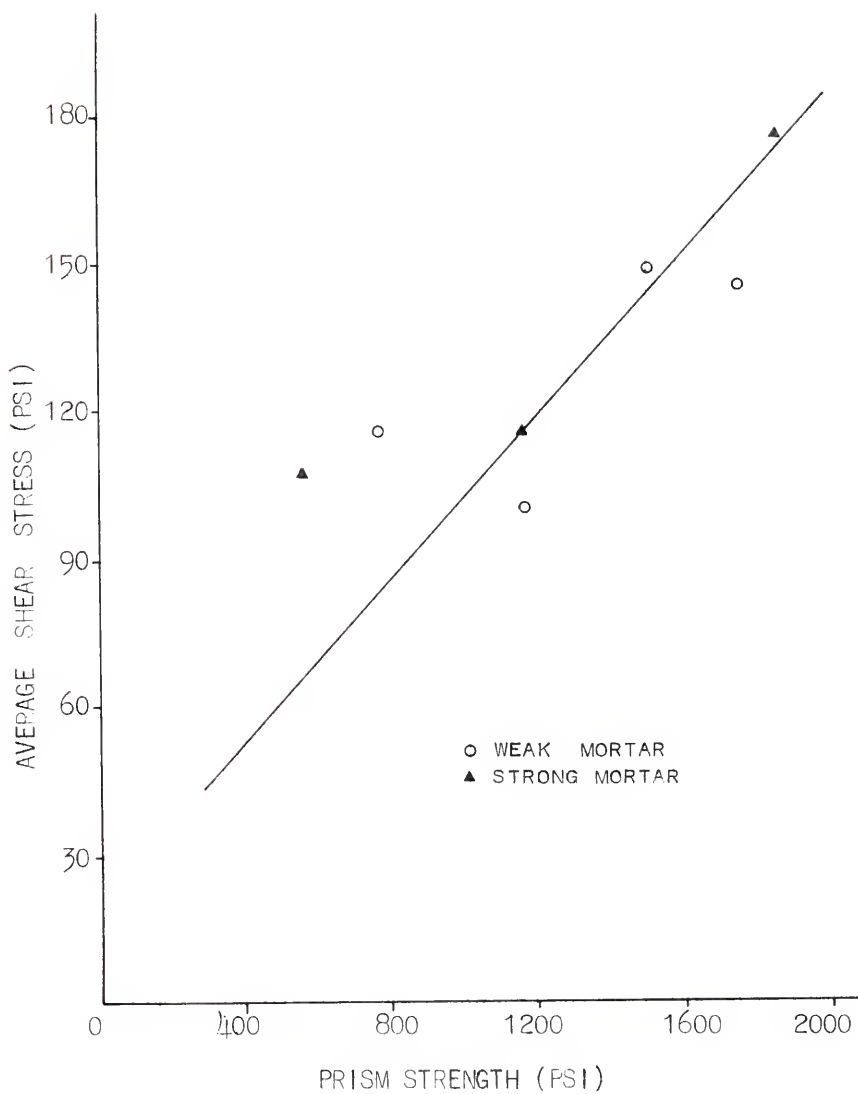
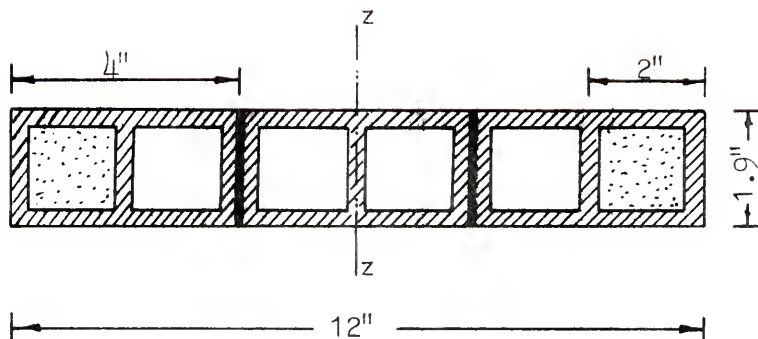


Fig. 5.2. Comparison of results of grouted piers with corresponding prism strengths.



$$\text{NET AREA} = 16.42 \text{ SQ. IN.}$$

Fig. 5.3. Area used to compute shear stress for hollow piers.

distributed over the cross-section of the pier. The results of the tests on nongrouted piers are shown in Table 5.2. Figure 5.4 shows the plot between the total precompression and the average shear stress in the pier. It is evident that precompression definitely aids in increasing the shear capacity of a nongrouted pier. Also, there was not a marked increase in the shear capacity of the piers when stronger mortar joints were used. However, this observation is limited to the strengths of mortars used in this investigation.

5.3 Equations for Predicting the Diagonal Tensile Strength of Masonry:

5.3.1 Grouted Piers: on the basis of this investigation, it is concluded that Equation (5.2) could be used for predicting the diagonal tensile strength of grouted masonry for the ranges of strengths of mortar and grout and for the pier configuration considered in this investigation. Blume (6) has suggested that diagonal tensile strengths should always be ascertained by testing a corresponding square panel under diagonal compression. In a model investigation such as this one, it is difficult to define a suitable size for the companion panel. Also, results on 4-ft-square panels tested by Schneider indicated that the ultimate shear strength of the masonry was nearly the same irrespective of the reinforcing present in these panels and it was

TABLE 5.2
TEST RESULTS OF NONGROUTED PIERS

Specimen	Age at Test (days)	Mortar Strength (psi)	Flow %	Precompression External (psi)	Internal (psi)	Total (psi)	Ultimate Load (lbs)	Shear Stress (psi)
PR 6	31	900	119	0	44	44	1,100	47
PR 13	41	900	119	50	113	163	2,830	122
PR 23	31	900	119	125	115	240	2,900	125
PR 17	35	900	119	200	178	378	4,450	192
PR 1	28	1344	120	0	63	63	1,600	69
PR 19	32	1344	120	50	127	177	3,200	138
PR 21	31	1344	120	125	169	294	4,180	180
PR 20	31	1344	120	200	230	430	5,600	241

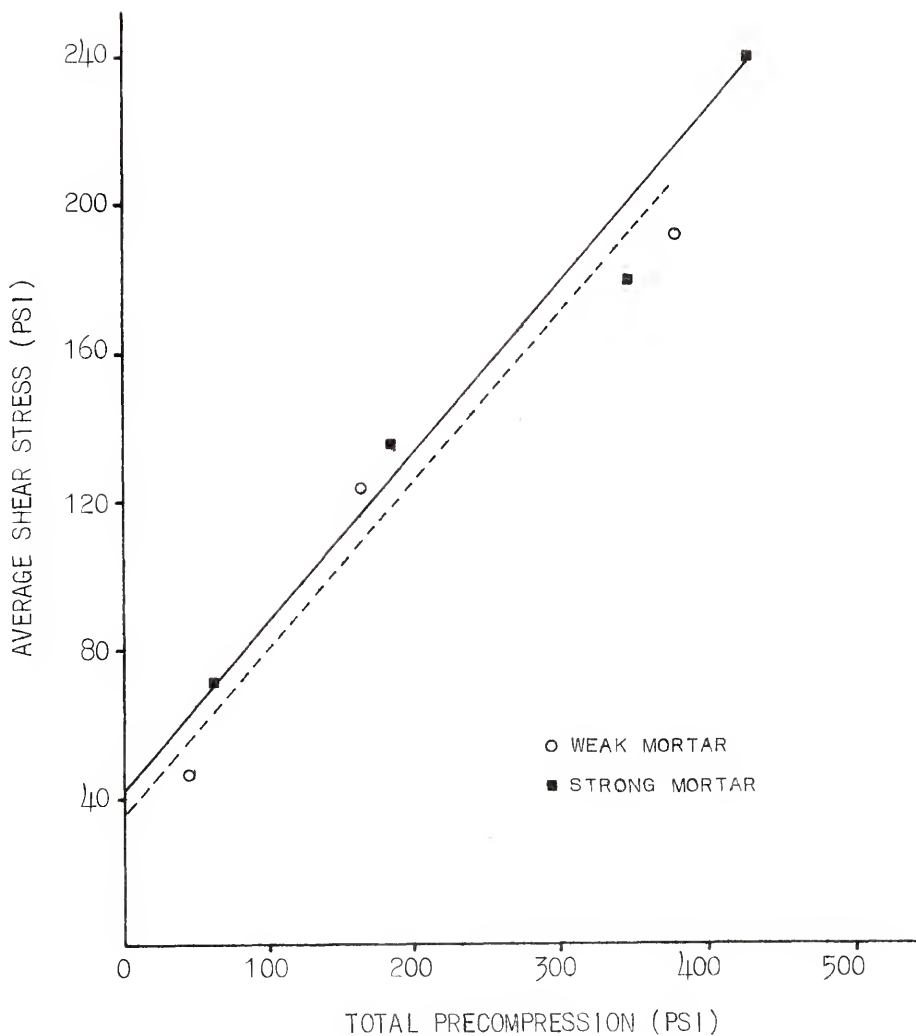


Fig. 5.4. Effect of precompression on shearing strength of nongROUTED piers.

not the same as the diagonal tensile stress produced by combined flexural tension and shear stresses in a pier contained within a wall (46). In the light of the above remarks, it is suggested that Equation (5.2) is a suitable means for ascertaining the strength of grouted piers with shear span to depth ratio (a/D) around 0.5. Since the shear strength varies with a/D ratios, more tests are necessary to arrive at a suitable value corresponding to other pier configurations.

5.3.2 Nongrouted Piers: a pier subjected to diagonal compression is idealized as shown in Figure 5.5. Applying the simple beam theory and considering YY as the neutral plane, the bending stress at any section XX is:

$$f_b = (Hy - X_1 V) / S_{zz}$$

where S_{zz} is the elastic section modulus corresponding to the extreme fiber computed on the basis of the cross-section shown in Figure 5.3, and H and V are the horizontal and vertical components of the diagonal load 'P'. The total precompression on the cross-section is taken as $(\frac{V - V_{PI}}{A} + f_{pr})$ where A is the area of cross-section of the pier as shown in Figure 5.3, f_{pr} is the extent of external precompression applied, and V_{PI} is the load taken by the pipe columns. Using Equation (3.3), the maximum allowable flexural tension at this level of precompression can be

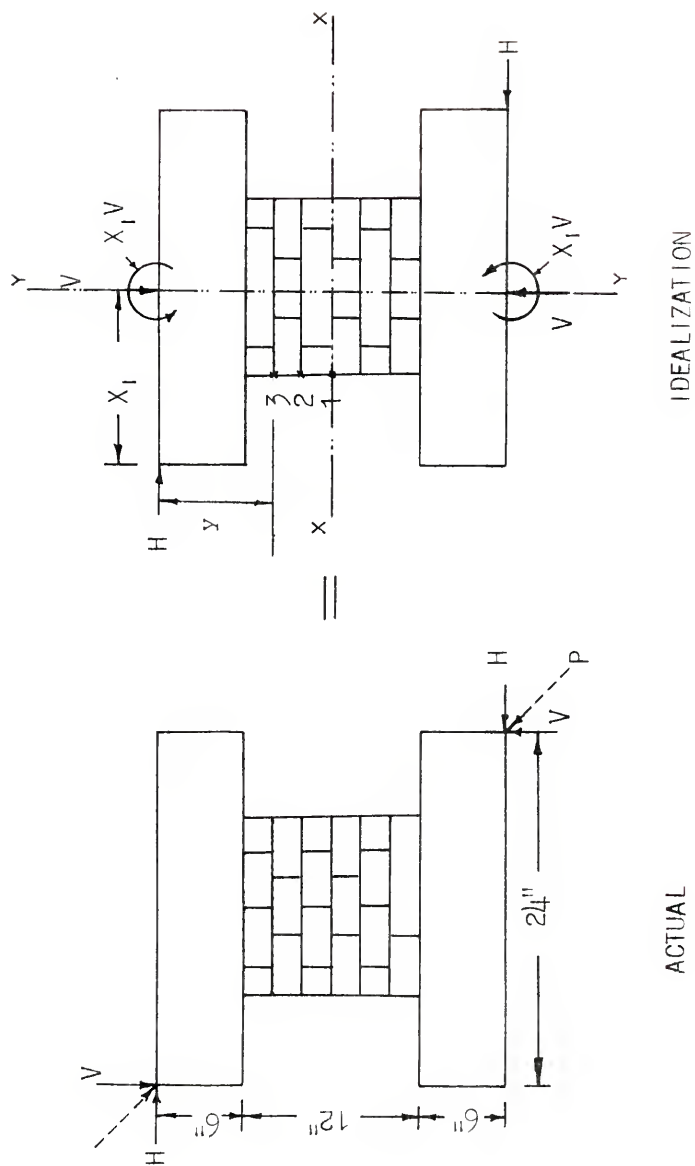


Fig. 5.5. Idealization for a pier loaded in diagonal compression.

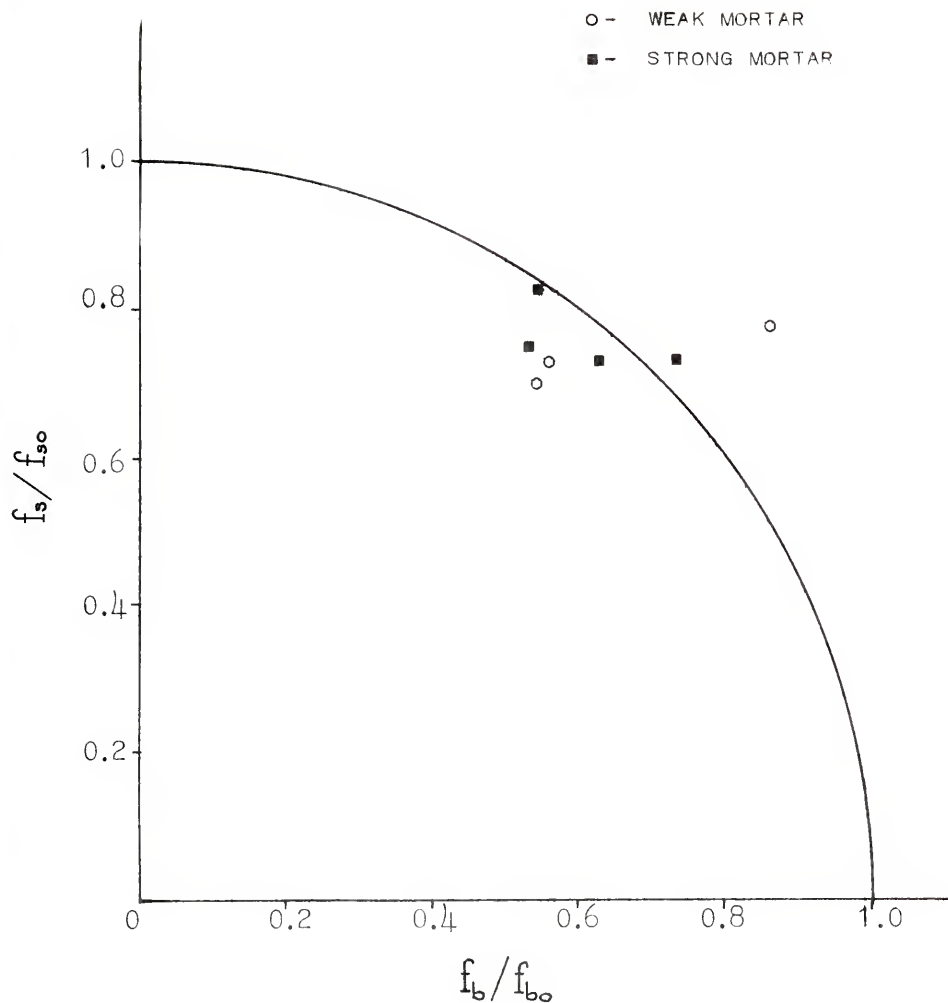


Fig. 5.6. Test results of nongROUTED pier specimens.

found (f_{bo}). The average shear stress on the cross-section is calculated as:

$$f_s = H/A$$

and the shear strength of the cross-section at this level of precompression is calculated from Equation (3.1) as f_{so} . It was verified whether the combined shearing and bending stresses on the mortar joint satisfy the interaction equation proposed in Chapter 3, viz.,

$$\left(\frac{f_s}{f_{so}}\right)^2 + \left(\frac{f_b}{f_{bo}}\right)^2 = 1$$

The above results are presented in Table 5.3. It can be seen that the scatter is excessive in the case of piers with weak mortar joints. However, other pier specimens seem to follow the interaction equation quite closely. The values of f_s/f_{so} and f_b/f_{bo} are plotted on the interaction diagram to show the deviations graphically, as shown in Figure 5.6. The observed mode of failure verifies the above equation only for the piers without precompression where the debonding occurred first near point '3' in Figure 5.5. In all other cases, the crack originated at or near the center of the panel. This suggests that higher precompression resulted in correspondingly higher flexural tensile strength

TABLE 5.3

ANALYSIS OF RESULTS OF TESTS ON NONGROUTED PIERS

Specimen	H	V-V _{PI}	Total Precom- pression	f _{so}	f _{bo}	f _s	f _b	$\frac{f_s}{f_{so}}$	$\frac{f_b}{f_{bo}}$	$\frac{(9)^2}{(10)^2}$	f _{max}	$\frac{f_{max}}{f_t}$	$\frac{f_{max}}{f_{dt}}$	$\frac{f_s}{0.7f_{so}}$
(1)	(2)	(3)	(4)	(5)	(6)	(7)	(8)	(9)	(10)	(11)	(12)	(13)	(14)	(15)
PR 6	778	728	44	60	82	47	71	0.78	0.86	1.35	27	0.201	0.93	-
PR 23	2051	1891	240	179	327	125	177	0.70	0.54	0.78	53	0.265	1.83	1.00
PR 13	2001	1861	163	133	231	122	178	0.92	0.77	1.43	58	0.428	1.99	0.76
PR 17	3147	2921	378	263	500	192	278	0.73	0.56	0.84	80	0.593	2.76	0.96
PR 1	1131	1035	63	94	151	69	95	0.74	0.63	0.94	38	0.190	0.78	-
PR 19	2263	2079	177	167	348	138	193	0.83	0.55	0.99	75	0.375	1.53	0.85
PR 21	2956	2772	294	242	511	180	271	0.74	0.53	0.83	85	0.427	1.73	0.94
PR 20	3960	3776	430	329	786	241	384	0.73	0.73	0.78	108	0.540	2.20	0.96

at point '3', thus suppressing debonding of the mortar joint at that point. Hence, it is logical to assume that the critical point under higher precompression for a pier configuration considered in this investigation would be the center of the pier wherein the bending stresses are absent. Therefore, it can be concluded that failure by debonding would occur in those cases wherein the shear stress exceeds the shear strength of the joint given by Equations (3.1) and (3.2), depending on the type of mortar used. This would suggest a value of $f_s/f_{so} = 1$ in column (9) of Table 5.3. As can be seen, the values of f_s/f_{so} range from 0.7 to 0.916, suggesting the variability involved. It can also be noted that Equations (3.1) and (3.2) consistently overestimate the capacity of the pier. Hence, it is suggested that the shear strength obtained using the above equations be suitably factored. A multiplier of 0.7 is recommended. The adjusted values using a factor of 0.7 are shown in column (15) of Table 5.3.

The above procedure is recommended for piers with an a/D ratio less than or equal to 0.5. For higher a/D ratios, the bending stresses are more predominant and the interaction Equation (3.5) seems to be more applicable.

Since the debonding failure mode could be suppressed completely at higher levels of precompression, it can be conceived that failure might be initiated by exceeding the tensile strength of the mortar or block. The maximum

principal stress occurs at the center of the pier. The state of stress at this point is assumed to be as shown in Figure 5.8. The maximum principal stress is given by:

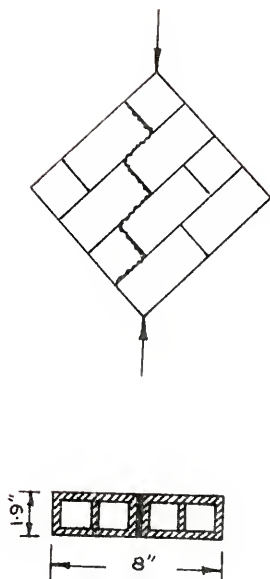
$$f_{\max} = -\frac{1}{2}\left(\frac{V}{A} + f_{pr}\right) + \sqrt{0.25\left(\frac{V}{A} + f_{pr}\right)^2 + \left(\frac{H}{A}\right)^2}$$

Tensile cracking is assumed to occur if f_{\max} exceeds the tensile strength of the block or mortar, whichever is less:

$$f_{\max} \geq f_t \quad (5.4)$$

The values of f_{\max}/f_t are given in column (13) in Table 5.3. The results indicate that in no case did failure occur due to tensile cracking.

Another failure criterion that could be conceived is to equate the maximum principal stress to the diagonal tensile strength of a square panel. A square panel 8" x 8" was built for this purpose with the same mortar and blocks used for building the corresponding pier. This was tested under diagonal compression as shown schematically in Figure 5.7. For both mortar types, the failure was initiated by debonding of the mortar joints as shown in Figure 5.8. The panel with weaker mortar joints failed at 350 lbs, while the one with stronger joints failed at 600 lbs. Based on the net area of cross-section of the panel, the average shear stress as a measure of the diagonal tension



NET AREA = 8.6 SQ. IN.

Fig. 5.7. Failure pattern of hollow square panel subject to diagonal compression.

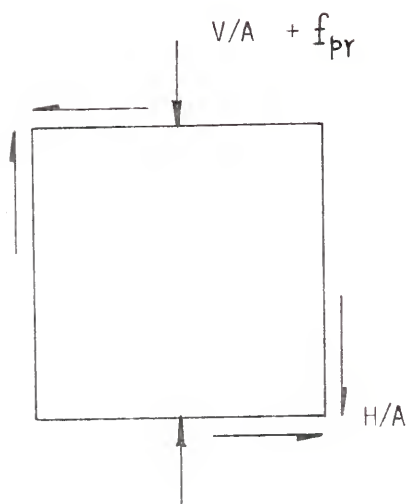


Fig. 5.8. Assumed state of stress at the center of pier.

for both cases is , respectively, 29 psi and 49 psi. The values of f_{\max}/f_{dt} are given in column (14) in Table 5.3, where f_{dt} is the value of the shear stress obtained in the diagonal tension test. As the results indicate, this criterion seems to be valid only for the case without any external precompression.

The equations proposed by Sinha and Hendry (50) for predicting the load capacity of brickwork have already been presented in Chapter 1. They proposed that within certain values of precompression the failure was initiated by the maximum stress exceeding the tensile strength of the brickwork. In the case of brickwork, the tensile strength was determined by a diametrical compression test on a circular disc of masonry. The equations proposed by Sinha and Hendry (50) were applied for the nongROUTED piers assuming the diagonal tensile strength obtained from the square panel for f_t in Equation (1.10) and Equation (1.11). Imaginary values were obtained for the lower limit of precompression. The upper limits of precompression were found to be 85 psi and 158 psi for piers with weak and strong mortar, respectively. This implies that in the case of piers with weak mortar joints, the failure will result in compression typically by vertical splitting for precompressive stresses above 85 psi. In this study, the failure patterns suggest a failure initiated by debonding of mortar joints. The difference may be attributed to the

size of the square panel considered for determining the diagonal tensile strength and in differences between brick and concrete block masonry. However, more tests are necessary to arrive at a definite conclusion in this regard.

In the light of the preceding remarks, the following equations are proposed for ascertaining the shear strength of a nongROUTED masonry pier:

Case (i): The following equations are considered to be applicable for pier configurations for low levels of precompression; but for piers with shear span to depth ratio > 0.5 , these equations may be considered to be applicable for all levels of precompression:

$$\left(\frac{f_s}{f_{so}}\right)^2 + \left(\frac{f_b}{f_{bo}}\right)^2 = 1$$

$$f_{\max} = f_t$$

The lesser of the loads predicted by the above equations is to be taken as the ultimate load on the pier.

Case (ii): For piers with a/D ratio less than 0.5, the governing equations are:

$$f_s = 0.7(f_{so})$$

$$f_{\max} = f_t$$

The minimum load obtained from the above equations is to be taken as the ultimate load on the pier.

CHAPTER 6

NONLINEAR FINITE ELEMENT ANALYSIS

6.1 General Remarks: The finite element method is now widely accepted as a method of stress analysis. "Progress in the method has been made on three fronts, all of which contribute to the strength and flexibility of the method. First of all, the relation of the finite element method to previous well-established methods in continuum mechanics has given it a firm foundation. Secondly, the search for and development of the many consistent elements has given it a wide area of application. Finally, extension of the method to the study of nonlinear behavior in both material and geometric nonlinearities has resulted in more realistic models and design methods" (37, p. 35).

The finite element method has been described extensively in the literature. A comprehensive discussion of the theory and application of the method to two-dimensional and three-dimensional systems is given in the book by Zienkiewicz (55). An introductory treatment of the method is given in the book by Desai and Abel (15).

6.2 Finite Element Linear Analysis: The following steps outline the basic procedure of a Finite Element Linear Analysis:

1. Discretization of the continuum: The basis of the finite element method is the representation of a body or a structure by an assemblage of subdivisions called finite elements. These elements are interconnected at joints, which are called nodes, and also along their interfaces.

2. Selection of displacement model: Simple functions called interpolation functions are chosen to approximate the distribution or variation of the actual displacements (or other field variables) over each finite element. Thus, the element displacements ' $u(x,y,z)$ ' are expressed in terms of a finite number of nodal displacements (δ) through assumed interpolation functions ' N ':

$$\{u(x,y,z)\} = \{N(x,y,z)\} \{\delta\} \quad (6.1)$$

It is generally not possible to select a displacement function that can represent exactly the actual variation of displacement in the element. Hence, the basic approximation of the finite element method is introduced at this stage.

3. Strains: By differentiating equation (6.1), element strains $\{\epsilon\}$ may be stated in terms of the nodal point displacements $\{\delta\}$:

$$\{\epsilon\} = \{B\} \{\delta\} \quad (6.2)$$

4. Stresses: Stresses are related to strains through a constitutive law. Usually, a linear relation is assumed.

$$\{\sigma\} = [D] (\{\epsilon\} - \{\epsilon_0\}) + \{\sigma_0\} \quad (6.3)$$

where $\{\epsilon_0\}$ are the initial strains and $\{\sigma_0\}$ the residual stresses.

5. Using the principle of virtual displacements, the element stiffness matrix $[k]$ relating element nodal forces $\{F\}$ to nodal displacements $\{\delta\}$ is formed:

$$\{F\} = [k] \{\delta\} \quad (6.4)$$

where,

$$[k] = \int \{B\}^T [D] \{B\} d(vol) \quad (6.5)$$

6. The structure stiffness matrix or global stiffness matrix $[K]$ relating external nodal point forces $\{R\}$ to the nodal displacements $\{\delta\}$ is assembled by using the Direct Stiffness Method where it is possible to add directly the individual stiffnesses $[k]$ and loads to locations in the overall matrices $[K]$ and $\{R\}$ in conformity with the requirements of one-to-one correspondence between the nodes of the elements and those of the assemblage.

$$\{R\} = [K] \{\delta\} \quad (6.6)$$

7. Equation (6.6) is solved to determine the nodal point displacements:

$$\{\delta\} = [K]^{-1} \{R\} \quad (6.7)$$

8. The element strains and the element stresses are found using equations (6.2) and (6.3), respectively.

6.3 Finite Element Nonlinear Analysis:

6.3.1 General Remarks: in the displacement method of finite element analysis, nonlinearities occur in two different forms. The first is material or physical nonlinearity which results from nonlinear constitutive laws. The second is geometric nonlinearity which derives from finite changes in the geometry of the deforming body.

The first category encompasses problems in which the stresses are not linearly proportional to the strains, but in which only small displacements and small strains are considered and linear strain displacement relations are used. Since displacements in reinforced concrete structures are inherently small, geometric nonlinearities generally do not occur and attention can be restricted to the problems of nonlinear material properties (47). These include:

1) cracking of the concrete; 2) nonlinear stress-strain

relations for concrete, steel, bond and aggregate interlock; and 3) time dependent effects such as creep, shrinkage, temperature and load history.

6.3.2 General Physical Approach: for arriving at the solution of a linear elastic problem, the set of equations,

$$[K] \{\delta\} - \{R\} = 0 \quad (6.8)$$

were solved in which the vector $\{R\}$ lists all the forces due to external loads, initial stresses and strains, etc.

In the above, a linear constitutive law (Eq. 6.3) and a linear strain displacement relation (Eq. 6.2) were assumed. Continuity of displacements was required and the equilibrium conditions were satisfied approximately.

In a nonlinear constitutive problem, displacement continuity and equilibrium still have to be satisfied. Thus, the only relationship which has to be replaced is Equation (6.3). This new relation, in general, will be given by some relation,

$$f(\{\sigma\}, \{\epsilon\}) = 0 \quad (6.9)$$

If a solution of Equation (6.8) can be achieved in which, by adjustment of one or more of the parameters $[D]$, $\{\epsilon_0\}$, or $\{c\}$ in Equation (6.3), this and Equation (6.9) are made to yield the same stress values, then a solution is found. An

iterative procedure becomes necessary. If the iteration is conducted by adjustment of the $[D]$ matrix, the process is known as one of variable stiffness. If $\{\epsilon_0\}$ or $\{\sigma_0\}$ is adjusted, so-called initial strain or initial stress approaches are obtained.

In many real situations, relations of the type of Equation (6.9) cannot be written in terms of total strains and stresses; however, relations could be established between the increments $\{\Delta\sigma\}$ and $\{\Delta\epsilon\}$. In such cases, the same process can be applied for an increment of load. Such incremental processes can be combined with any of the previous methods.

6.4 Variable Stiffness Methods: The procedure for linear analysis described in Section 6.2 can be utilized in conjunction with one of several iterative schemes to account for nonlinear behavior. The simple truss structure of Figure 6.1 can be utilized to explain the three common iterative solution techniques illustrated in Figure 6.2 (47). These are designated as: a) initial stiffness method, b) secant stiffness method, and c) tangent stiffness method.

stress-strain relation for any of the elements is to be nonlinear in compression and to be linear in tension. The nonlinear analysis is to be made for a given load R . The following steps are performed:

1. For the segment 0-1 in Figure 6.2, the initial stiffness 0-1 on the σ - ϵ curve is used in all the three

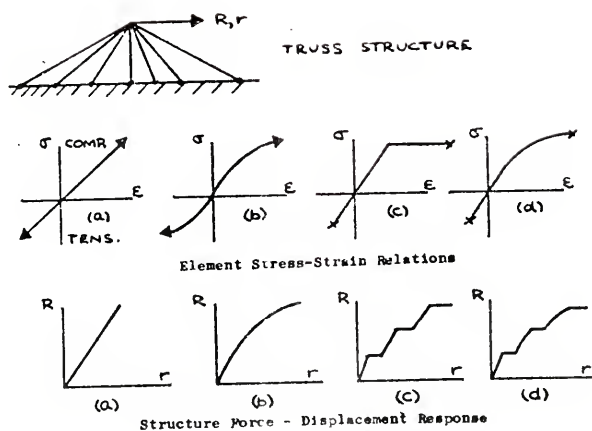


Fig. 6.1. Effect of nonlinear material properties.

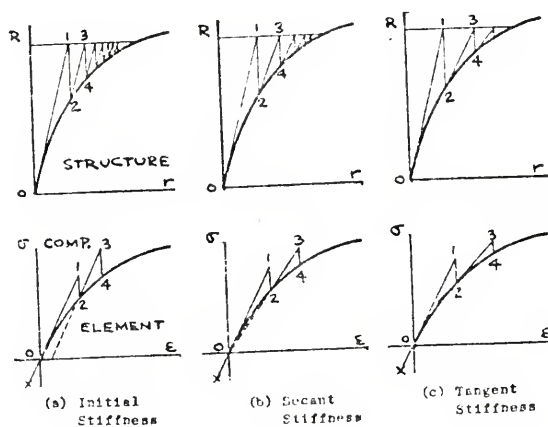


Fig. 6.2. Iterative solution techniques for nonlinear analysis.

methods to find the element stiffness $[k]$ and the structure stiffness $[K]$. Equations (6.1) through (6.7) are used to find the displacements and strains.

2. For the segment 1-2 in all three methods, the actual stress σ corresponding to ϵ from step 1 is found for each element. The unbalanced element stresses $\Delta\sigma_{12}$ are computed, from which the unbalanced nodal forces ΔR_{12} can be obtained by proper summation.

3. For the segments 2-3 and 3-4, the procedure differs for the three methods. In each case, the structure is to be analyzed for the unbalanced load ΔR_{12} .

a) the initial stiffness from the σ - ϵ curve is used again and steps 1 and 2 above are repeated.

b) the secant stiffness, 0-2-3, from the σ - ϵ curve is used and steps 1 and 2 above are repeated.

c) the tangent stiffness at point 2 on the σ - ϵ curve is used and steps 1 and 2 above are repeated.

In all the three methods, if a tensile failure occurs in an element, its stiffness $[k]$ is disregarded.

4. Steps 1, 2, and 3 above are repeated until the unbalanced nodal point forces ΔR reach a predefined acceptable value, at which time, final values of stresses, strains and displacements are output.

It is evident that the convergence is fastest by the tangent stiffness method and slowest by the initial stiffness method. On the other hand, only the initial stiffness method possesses the distinct advantage that the structure stiffness $[K]$ need not be reformulated for each iteration. If direct solution methods are used in the elastic program, the variable stiffness method is extremely uneconomical.

6.5 Initial Stress Method: The "initial stress" process as proposed by Zienkiewicz et al. (57) approaches the solution of a nonlinear problem as a series of approximations. In the first place, during a load increment, a purely elastic problem is solved and incremental strains $\{\Delta\epsilon'\}$ and incremental stresses $\{\Delta\sigma'\}$ are obtained. The nonlinearity implies, however, that for the increment of strain found, the stress increment will, in general, not be correct. If the true increment of stress possible for the given strain is $\{\Delta\sigma\}$, then the situation can only be maintained by a set of body forces equilibrating the "initial stress" system $(\{\Delta\sigma'\} - \{\Delta\sigma\})$.

At the second stage of the computation, this body force system can be removed by allowing the structure (with unchanged elastic properties) to deform further. An additional set of strain and corresponding stress increments is caused. Once again, these are likely to exceed those permissible by the nonlinear relationship, and the redistribution of equilibrating body forces has to be repeated.

If the process converges then finally within an increment the full nonlinear compatibility and equilibrium conditions will be satisfied, just as they are in an "incremental elasticity" solution.

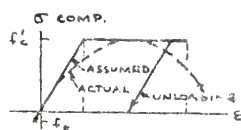
It can be noted that at every stage of the iteration the same stiffness matrix is used and, if this is once inverted, each step can be accomplished in a small fraction of the time needed for the first solution. The body forces calculated at the last iteration can be considered as an unbalanced residual force left on the structure and this serves as a means to assess the error involved.

6.6 Initial Strain Method: This method is similar to the initial stress approach and is useful when the stress level cannot be explicitly determined in terms of strain, but strains in terms of stress. Thus symbolically,

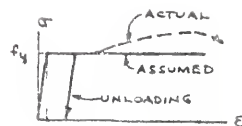
$$\{\epsilon\} = f(\{\sigma\}) \quad (6.10)$$

Now the equality between the above equation and the elastic relation (Eq. 6.3) can be obtained by adjusting $\{\epsilon_0\}$. Here, also, Equation (6.8) is solved iteratively, but the elastic strains obtained at every stage are compared with those corresponding to the constitutive relation (Eq. 6.10) and the difference used in evaluating the residual forces.

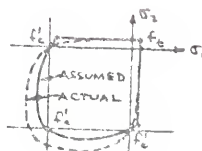
6.7 Previous Investigations: The various aspects of application of the finite element method to reinforced concrete structures were reviewed recently by Scordelis (47). The response of a reinforced concrete wall panel specimen was studied experimentally and analytically by Cervenka and Gerstle (10). Constant strain triangular finite elements were used to model the concrete and steel reinforcement. The steel was assumed to be uniformly distributed over the element in two orthogonal directions, and a composite material constitutive relation was developed in order to determine the element stiffness matrix. The constitutive relations are shown in Figures 6.3(a) and 6.3(b). The assumed biaxial stress criterion is shown in Figure 6.3(c). The concrete plasticity was limited by maximum concrete strain ϵ_u . Plasticity of the uncracked concrete, which is in a biaxial state of stress, was assumed to obey the von Mises yield criterion and associated flow rule. A method similar to that presented by Zienkiewicz et al. (57) was used in the finite element analysis to account for plastic deformations under biaxial compressive yielding. An incremental nonlinear analysis was used which accounted for tensile cracking and subsequent stress redistribution. No account was taken of bond, the effects of dowel action and aggregate interlocking of crack faces. The experimental and analytical crack patterns obtained are shown in Figures 6.3(d) and (e).



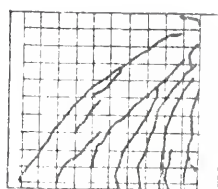
(a) Uniaxial Stress-Strain Curve for Concrete



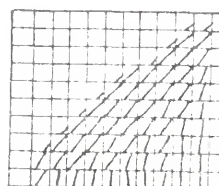
(b) Uniaxial Stress-Strain Curve for Steel



(c) Concrete Failure Criteria



(d) Experimental Crack Pattern



(e) Analytical Crack Pattern

Fig. 6.3. Material idealization and selected results of analysis of RC panels by Cervenka and Gerstle.

Franklin (19) used quadrilateral discrete elements for concrete and one dimensional bar elements for steel reinforcement for analyzing shear panels. A multilinear stress-strain curve was used for concrete in compression and also for reinforcement to approximate the actual curves obtained in uniaxial tests, while a linear curve was assumed up to failure in tension for concrete.

Figure 6.4 shows the biaxial failure criterion assumed for concrete. Tensile cracking was accounted for and the concrete was assumed to have failed when it reached f_c' in compression with no subsequent plasticity. An incremental iterative secant stiffness approach was used for the analysis.

Yuzugullu and Schnobrich (53) used quadrilateral elements composed of four constant strain triangles to model a shear-wall frame system. Special tie link elements were used to connect the wall to the frame. The steel bar reinforcement mesh used in the wall was assumed to be smeared out and uniformly distributed over each quadrilateral element. The von Mises yield criterion was assumed for the biaxial compression of concrete. An elastic perfectly plastic stress-strain relationship was assumed for concrete and steel, with a limiting compressive strain in the case of concrete. A composite material property matrix for the reinforced concrete model was obtained as the sum of the material property matrices of the concrete and of

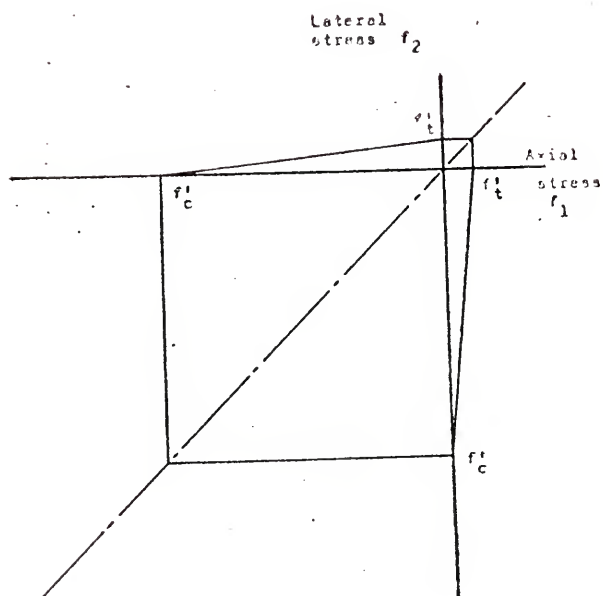


Fig. 6.4. Failure envelope adopted by Franklin.

reinforcing. Full bond was assumed to remain even throughout the crack region. Concrete was assumed to crack when principal tensile stress reached the tensile strength of the concrete. It was assumed that the cracked concrete could no longer carry any tensile forces perpendicular to the crack, but could maintain some amount of shear stiffness because of the irregular surface of the crack. A shear retention factor β was introduced so that a shear force could be transferred across the cracked planes. It was realized that the shear strength along the crack should be a function of the crack width and has upper and lower bounds of one and zero relative to the uncracked shear strength capacity (23). However, a constant value of 0.4 was assumed in the analysis. Elastic behavior of a cracked element was terminated if compressive yielding occurred in the cracked concrete and/or yielding occurred in the steel reinforcement. Once concrete reached its ultimate strain, it was assumed to crack and its stiffness was disregarded.

Figures 6.5 and 6.6 illustrate schematically the method of solution adopted. Method 1 was used to account for plasticity of the reinforcement and cracking of concrete, while Method 2 was used for biaxial plasticity of the concrete.

Suidan and Schnobrich (52) used three-dimensional 20-node isoparametric elements to investigate the cracking,

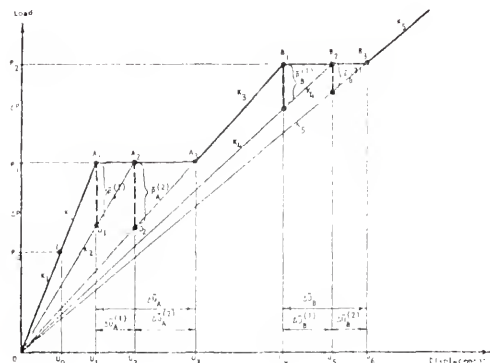


Fig. 6.5. Schematic diagram to illustrate crack propagation (initial stress method using variable stiffness within an increment).

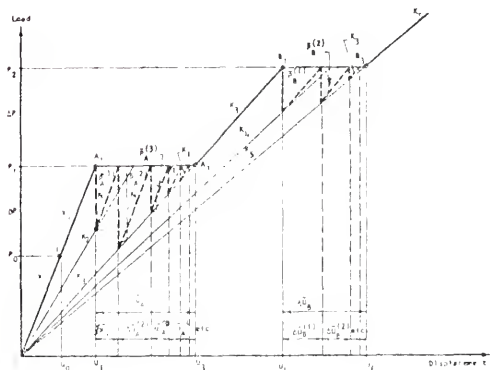


Fig. 6.6. Schematic diagram to illustrate crack propagation (initial stress method using constant stiffness within an increment).

crushing, and yielding of reinforced concrete beams. The constitutive relations and the method of analysis were the same as in the previous case. However, stresses and strains were computed at integration points so that the failure patterns could be investigated at these points. In both of the previous two investigations, no biaxial stress failure criteria were assumed.

6.8 Objective and Scope of Present Investigation: In this investigation, an attempt is being made to use the Finite Element Method to estimate the load capacity of concrete masonry elements. The analytical model and the method of solution adopted are described in Chapters 7 and 8. The analysis takes into account cracking, crushing, and compressive yielding of the concrete blocks, mortar, and grout, as well as the debonding of mortar joints. The theoretical results are compared with experimental data. The analysis considers only short time loading.

CHAPTER 7

DESCRIPTION OF ANALYTICAL MODEL

7.1 Choice of Finite Elements: The problem under investigation is assumed to be approximated by plane stress conditions. A number of finite elements have behavior characteristics that are adequate when used to represent a small region of a structure, but are insufficient when behavior of the structure depends on a small number of such elements (52). In order to provide flexibility in an analysis of concrete masonry panels such that it can go beyond the early cracking stages, elements which can be adapted to general shapes should be employed. The best available element of this kind is the isoparametric element (55) (56). Here the geometry and displacements of the element are described in terms of the same interpolation functions:

$$x = \{N^T\} \{X_n\} \quad (7.1)$$

$$u = \{N^T\} \{\delta\} \quad (7.2)$$

where 'x' is the x-coordinate of any point and 'X_n' that of node 'n' in an element, 'u' is the displacement in

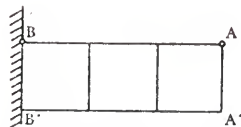
x-direction at any point, and ' δ ' represents the nodal displacements.

Thus, the shape function is identical to those used to generate the element. Equations of the form of Eq. (7.1) may be considered as transformations between Cartesian coordinates and curvilinear coordinates if $[N]$ is a matrix of shape functions of order two or more. These equations can be interpreted as the mapping of a straight-sided element in local coordinates into a curved-sided element in global Cartesian system, provided that the transformation is unique in that there is one-to-one correspondence between points in the two coordinate systems.

Any shape function chosen, for proper convergence, should provide for rigid body displacements, constant strain conditions, and finite strains at the interface between elements. Zienkiewicz and Irons (56) have shown how, for a given number of total degrees of freedom, the representation improves when elements with progressively larger degrees of freedom are used (Figure 7.1). Accordingly, a quadratic rectangular element (8 nodes) was chosen for this investigation (Figure 7.2). Satisfying the convergence criteria mentioned above, the shape functions for this element are:

$$N_i = 1/4 (1 + \xi\xi_i) (1 + \eta\eta_i) (\xi\xi_i + \eta\eta_i - 1)$$

for corner nodes, and,



TYPE OF ELEMENT	VERTICAL LOAD OF 1 AT A		COUPLE AT 1 AT A	
	MAX DEFL AT AA	MAX STRESS BB	MAX DEFL AT AA	MAX STRESS BB
	-26	-19	-22	-22
	0.53	0.51	0.52	0.55
	-65	-56	-67	-67
	-99	-99	1.00	1.00
	1.00	1.00	1.00	1.00
EXACT	1.00	1.00	1.00	1.00

Fig. 7.1. Solution of a cantilever beam by elements with varying degrees of freedom.

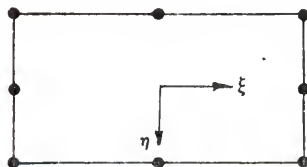


Fig. 7.2. Quadratic rectangular element.

$$\xi_i = 0: N_i = 1/2 (1 - \xi^2) (1 + \eta\eta_i)$$

$$\eta_i = 0: N_i = 1/2 (1 + \xi\xi_i) (1 - \eta^2)$$

for midside nodes.

7.2 Formulation of Element Stiffness Matrix:

a) Displacement function: in the plane stress case, the displacements at any point within an element defined by nodes 1, 2, 3... can be written as:

$$\begin{Bmatrix} u \\ v \end{Bmatrix} = \{N_1, N_2, N_3 \dots\} \begin{Bmatrix} \delta_1 \\ \delta_2 \end{Bmatrix} \quad (7.3)$$

where,

$$\{\delta_1\} = \begin{Bmatrix} u_1 \\ v_1 \end{Bmatrix}$$

b) Strains: the strains at any point can be written as:

$$\{\epsilon\} = [B] \{\delta\}^e \quad (7.4)$$

For the plane stress case,

$$\{\epsilon\} = \begin{Bmatrix} \epsilon_x \\ \epsilon_y \\ \gamma_{xy} \end{Bmatrix} = \begin{Bmatrix} \frac{\partial u}{\partial x} \\ \frac{\partial v}{\partial y} \\ \frac{\partial u}{\partial y} + \frac{\partial v}{\partial x} \end{Bmatrix} \quad (7.5)$$

With the shape functions $[N]$ already obtained, the matrix $[B]$ may easily be computed.

c) Stresses: considering the initial strains ϵ_0 and residual stresses σ_0 and assuming general elastic behavior, the relationship between stress and strain will be of the form,

$$\{\sigma\} = [D] (\{\epsilon\} - \{\epsilon_0\}) + \{\sigma_0\} \quad (7.6)$$

where $[D]$ is the elasticity matrix containing the appropriate material properties. For the plane stress case,

$$\{\sigma\} = \begin{Bmatrix} \sigma_x \\ \sigma_y \\ \tau_{xy} \end{Bmatrix} \quad (7.7)$$

$$[D] = \frac{E}{1 - \nu^2} \begin{bmatrix} 1 & \nu & 0 \\ \nu & 1 & 0 \\ 0 & 0 & \frac{1-\nu}{2} \end{bmatrix} \quad (7.8)$$

d) Equivalent nodal forces: if a typical element 'e' is examined, the forces at the nodes are uniquely defined by:

- 1) 1) the displacements of those nodes $(\delta)^e$,
- 2) the distributed loading acting on the element (p),
- 3) the initial strain (ϵ_0) , and
- 4) the initial stress (σ_0) .

Assuming elastic behavior, the characteristic relationship will always be of the form,

$$\{F\}^e = [k]^e \{\delta\}^e + \{F\}_p^e + \{F\}_{\epsilon_0}^e + \{F\}_{\sigma_0}^e \quad (7.9)$$

where,

$[k]^e$ represents the element stiffness,

$\{F\}_p^e$ the nodal forces required to balance any distributed loads acting on the element,

$\{F\}_{\epsilon_0}^e$ the nodal forces required to balance any initial strain,

$\{F\}_{\sigma_0}^e$ the nodal forces required to balance any initial stress, and

$[k]^e \{\delta\}^e$ forces induced through the displacement of the nodes.

Thus,

$$\{F\}^e = \begin{Bmatrix} F_i \\ F_j \\ \vdots \end{Bmatrix} \quad (7.10)$$

define the equivalent nodal forces. Each of the forces $\{F_i\}$ must contain the same number of components as the corresponding nodal displacement $\{\delta_i\}$ and be ordered in the same direction.

For the plane stress case,

$$\{F_i\} = \begin{Bmatrix} U_i \\ V_i \end{Bmatrix} ; \quad \{p\} = \begin{Bmatrix} X \\ Y \end{Bmatrix}$$

in which components U and V correspond to the directions of 'u' and 'v' displacements. X and Y are the body force components.

To make the nodal forces statically equivalent to the actual boundary stresses and distributed loads, an arbitrary virtual nodal displacement can be imposed and the external and internal work done by the various forces and stresses during the displacement can be equated. Thus, we get,

$$\begin{aligned} \{F\}^e &= \left(\int \{B\}^T [D] \{B\} d(\text{vol}) \right) \{\delta\}^e - \int \{B\}^T [D] \{\epsilon_0\} d(\text{vol}) \\ &+ \int \{B\}^T \{\sigma_0\} d(\text{vol}) - \int \{N\}^T \{p\} d(\text{vol}) \end{aligned} \quad (7.11)$$

e) Evaluation of element matrices: an evaluation of $\int \{B\}^T [D] \{B\} d(\text{vol})$ in global coordinates is needed to compute the element stiffness. For plane problems,

$$\{B_i\} = \begin{vmatrix} \frac{\partial N_i}{\partial x} & 0 \\ 0 & \frac{\partial N_i}{\partial y} \\ \frac{\partial N_i}{\partial y} & \frac{\partial N_i}{\partial x} \end{vmatrix}$$

Consider the set of local coordinates and corresponding set of global coordinates x and y ,

$$\frac{\partial N_i}{\partial \xi} = \frac{\partial N_i}{\partial x} \frac{\partial x}{\partial \xi} + \frac{\partial N_i}{\partial y} \frac{\partial y}{\partial \xi}$$

$$\frac{\partial N_i}{\partial \eta} = \frac{\partial N_i}{\partial x} \frac{\partial x}{\partial \eta} + \frac{\partial N_i}{\partial y} \frac{\partial y}{\partial \eta}$$

Thus,

$$\begin{bmatrix} \frac{\partial N_i}{\partial \xi} \\ \frac{\partial N_i}{\partial \eta} \end{bmatrix} = \begin{bmatrix} \frac{\partial x}{\partial \xi} & \frac{\partial y}{\partial \xi} \\ \frac{\partial x}{\partial \eta} & \frac{\partial y}{\partial \eta} \end{bmatrix} \begin{bmatrix} \frac{\partial N_i}{\partial x} \\ \frac{\partial N_i}{\partial y} \end{bmatrix} = [J] \begin{bmatrix} \frac{\partial N_i}{\partial x} \\ \frac{\partial N_i}{\partial y} \end{bmatrix}$$

$$\begin{bmatrix} \frac{\partial N_i}{\partial x} \\ \frac{\partial N_i}{\partial y} \end{bmatrix} = [J]^{-1} \begin{bmatrix} \frac{\partial N_i}{\partial \xi} \\ \frac{\partial N_i}{\partial \eta} \end{bmatrix}$$

To evaluate $[J]$:

$$\{x\} = \{N^T\}\{x_i\} ; \quad \{y\} = \{N^T\}\{y_i\}$$

$$\frac{\partial x}{\partial \xi} = \frac{\partial N_i}{\partial \xi} x_i ; \quad \frac{\partial y}{\partial \xi} = \frac{\partial N_i}{\partial \xi} y_i$$

$$[J] = \begin{vmatrix} \frac{\partial N_1}{\partial \xi} & \frac{\partial N_2}{\partial \xi} & \cdots \\ \frac{\partial N_1}{\partial \eta} & \frac{\partial N_2}{\partial \eta} & \cdots \end{vmatrix} \begin{vmatrix} x_1 & y_1 \\ x_2 & y_2 \\ \vdots & \vdots \end{vmatrix} \quad (7.12)$$

Also, $dx \, dy$ equals $\det [J] \, d\xi \, d\eta$.

After finding the inverse of $[J]$, the matrix $\{B\}$ could be evaluated. Numerical integration using the Gauss Quadrature Formula is adopted, wherein,

$$\int_{-1}^{+1} f(x) \, dx = \sum_{j=1}^n H_j f(a_j) \quad (7.13)$$

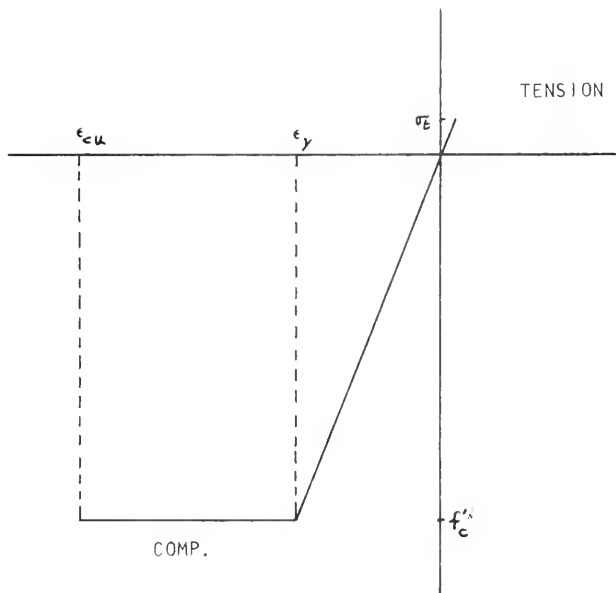
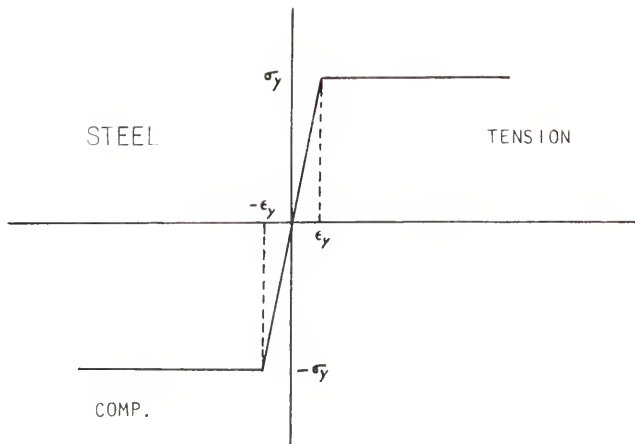
where H_j are the weighting coefficients, $f(a_j)$ the value of the function at specified points a_j , and n the number of Gauss points used.

7.3 Material Properties and Failure Criteria:

7.3.1 Uniaxial Stress-Strain Curves: the uniaxial stress-strain relationships considered for concrete block, mortar, grout, and reinforcing steel are shown in Figure 7.3.

7.3.2 Representation of Properties of Masonry Element: the uncracked masonry element is assumed to be isotropic and the material properties are represented by matrix $[D]$:

$$[D] = \frac{E}{1 - \nu^2} \begin{vmatrix} 1 & \nu & 0 \\ \nu & 1 & 0 \\ 0 & 0 & \frac{1-\nu}{2} \end{vmatrix} \quad (7.14)$$



CONCRETE BLOCK, MORTAR AND GROUT

Fig. 7.3. Uniaxial stress-strain curves.

In the discretization of a nongROUTED concrete masonry element for analysis element boundaries were made to coincide with the edges of the mortar joints so that the finite element would always represent a single material. However, even if the same discretization is adopted, every element would contain at least two different materials in the case of a grouted masonry element. Since the problem could only be handled using a three-dimensional analysis, an assumption has to be made regarding the value of E for such elements. For a plane problem this could be approximately handled by assuming the axial rigidity of the composite element as the sum of the axial rigidities of its components. No such modification is made for adjusting the Poisson ratio. A constant value is adopted. Referring to Figure 7.4, the equivalent modulus, E_{eq} , for the composite element is obtained as,

$$E_{eq} (at) = A_G E_G + A_B E_B + A_S E_S \quad (7.15)$$

where A_G , A_B , and A_S denote the areas of grout, block, and steel and E_G , E_B , and E_S denote the respective moduli. Perfect bond is assumed between steel and grout.

In order to calculate the stresses in the components, the following procedure is adopted. Since the strains are the same for each of the components, the stresses in a

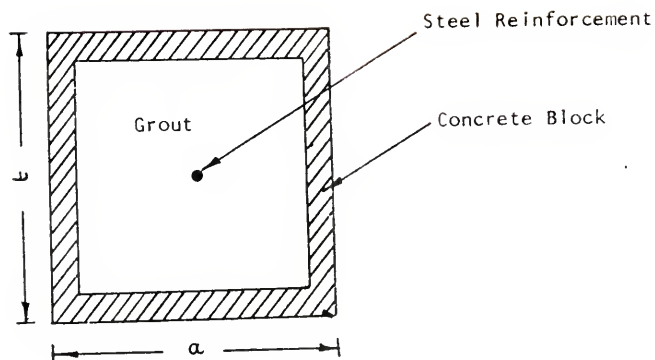


Fig. 7.4. Components of a reinforced grouted element.

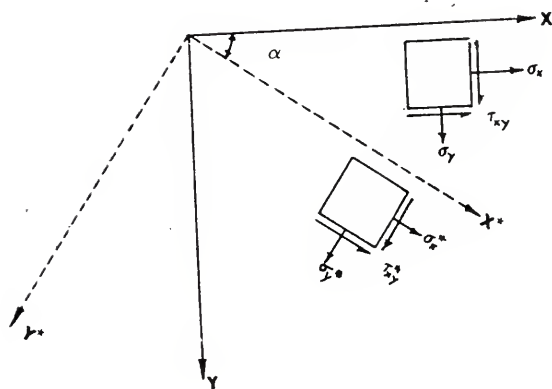


Fig. 7.5. Rotation of coordinates.

particular component, e.g., steel, are given by:

$$\begin{Bmatrix} \sigma_x^s \\ \sigma_y^s \\ \tau_{xy}^s \end{Bmatrix} = \frac{E_s}{1 - \nu^2} \begin{vmatrix} \epsilon_x^{eq} & \nu \epsilon_y^{eq} & 0 \\ \nu \epsilon_x^{eq} & \epsilon_y^{eq} & 0 \\ 0 & 0 & \frac{1-\nu}{2} \gamma_{xy}^{eq} \end{vmatrix} \quad (7.16)$$

In the case of steel reinforcement, the axial stresses have to be determined so as to detect yielding. Equation 7.16 can be used, and the stress corresponding to the direction of the steel reinforcement computed. If, however, the reinforcement were oriented at an angle to the x-y frame, then using a strain transformation matrix $[T_\epsilon]$, the strains at the new orientation could be determined. The positive directions of stresses and angle are indicated in Figure 7.5.

The strains corresponding to the new coordinate axes are (11):

$$\begin{Bmatrix} \epsilon_x^* \\ \epsilon_y^* \\ \gamma_{xy}^* \end{Bmatrix} = \begin{vmatrix} \cos^2 \phi & \sin^2 \phi & \sin \phi \cos \phi \\ \sin^2 \phi & \cos^2 \phi & -\sin \phi \cos \phi \\ -\sin 2\phi & \sin 2\phi & \cos 2\phi \end{vmatrix} \begin{Bmatrix} \epsilon_x \\ \epsilon_y \\ \gamma_{xy} \end{Bmatrix} \quad (7.17)$$

or,

$$\{\epsilon^*\} = [T_\epsilon] \{\epsilon\} \quad (7.18)$$

where $[T_\epsilon]$ is the strain transformation matrix.

Now Equation (7.16) is used to compute the stress in steel.

7.3.3 Plastic Yielding in Compression: the von Mises yield criterion and the associated flow rule are considered to be applicable for biaxial compression of the masonry components. For the plane stress case,

$$F = 1/2 [(\sigma_x - \sigma_y)^2 + \sigma_y^2 + \sigma_x^2] + 3\tau_{xy}^2 - \bar{\sigma}^2 \quad (7.19)$$

where $\bar{\sigma}$ equals the uniaxial stress at yield. The condition that F is less than, equal to, or greater than zero establishes, respectively, the condition where the stress vector is within the yield surface, on the yield surface, or outside it. The material stiffness matrix including these plasticity conditions was derived in detail in references (17) and (57). For incremental stress $\{\Delta\sigma\}$ and incremental strains $\{\Delta\epsilon\}$,

$$\{\Delta\sigma\} = [D_{ep}]\{\Delta\epsilon\} \quad (7.20a)$$

where $\{\Delta\sigma\}$ is the change in the stress vector which is compatible with a change in the strain vector, $\{\Delta\epsilon\}$, the increment being in the plastic region. The elasto-plastic matrix $[D_{ep}]$ is,

$$[D_{ep}] = [D] - [D] \left\{ \frac{\partial F}{\partial \{\sigma\}} \right\} \left\{ \frac{\partial F}{\partial \{\sigma\}} \right\}^T [D] \left[\left\{ \frac{\partial F}{\partial \{\sigma\}} \right\}^T [D] \left\{ \frac{\partial F}{\partial \{\sigma\}} \right\} \right]^{-1} \quad (7.20b)$$

No plasticity is accounted for if the point under investigation has already failed under the biaxial compressive strength criterion as described in the next section.

7.3.4 Biaxial Strength of a Masonry Component: Recently, various researchers (31 - 35) have proposed failure envelopes for biaxial strength of concrete. The failure envelope proposed by Liu et al. (33 - 35) for biaxial compression is considered to be applicable in this investigation because of its simplicity and nondependability on knowledge of any empirical constants. Their experiments consisted of testing thin square plates (5" x 5" x 1/2") under uniaxial and biaxial compression. Eight of their experiments were performed on idealized models of concrete and eighty-four used real concrete. Principal variables were ratio of principal stresses, water-cement ratio, aggregate-cement ratio, and maximum size of aggregate. Special effort was made to minimize the frictional confinement introduced between the bearing plates and concrete. The brush bearing platens designed by Buyukozturk et al. (7) were used in this investigation. Based on their experimental results, the failure envelope shown in Figure 7.6 was proposed and may be written as:

$$\alpha < 0.2 \qquad \sigma_p / \sigma_o = 1 + \frac{\alpha}{1.2\alpha - 1} \qquad (7.21)$$

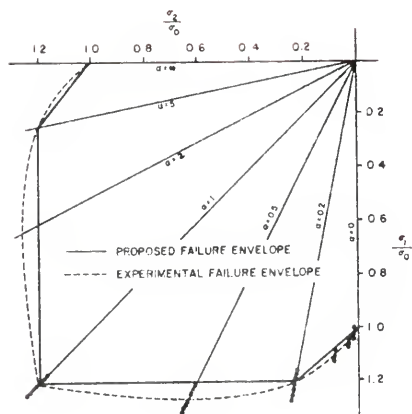


Fig. 7.6. Liu's failure envelope for concrete under biaxial compression.

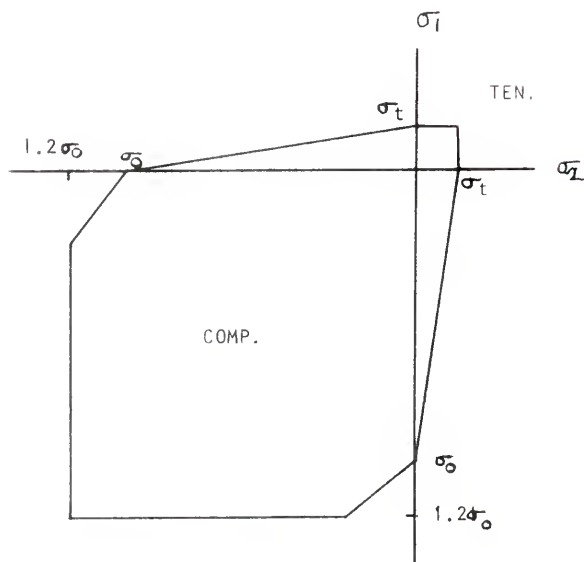


Fig. 7.7. Assumed failure envelope for block, mortar, and grout.

$$\begin{array}{ll}
 1.0 \geq \alpha \geq 0.2 & \sigma_p / \sigma_o = 1.2 \\
 5.0 \geq \alpha \geq 1.0 & \sigma_p / \sigma_o = 1.2 / \alpha \quad (7.21 \text{ cont}) \\
 \alpha > 5.0 & \sigma_p / \sigma_o = \frac{1}{\alpha} \left(1 + \frac{1}{1.2\alpha - 1} \right)
 \end{array}$$

where σ_o equals ultimate strength of concrete plate in uniaxial compression in psi, σ_p equals peak stress in biaxial compression in psi, and α equals ratio of principal stress in orthogonal direction to principal stress in direction considered.

The complete biaxial strength envelope assumed for the present investigation is shown in Figure 7.7 where f_t equals tensile strength of the component. While considering grouted masonry elements, the values of σ_o and σ_t are assumed to be as for the weaker of the two components, viz., grout and mortar or grout and concrete block as the case may be.

7.3.5 Crushing of Masonry: once the compressive strain exceeds a limiting strain, ϵ_{cu} , of the weaker component in an element, then it is assumed to crush at that point, and its stiffness is disregarded, i.e., $[D]$ is zero.

7.3.6 Cracking: the principal stress planes can be determined at any point in an element from the stress vector at that point. Since uncracked masonry is assumed to be isotropic, the constitutive matrix $[D]$ is applicable

in the principal stress coordinate system. The cracking strength of masonry is determined from the biaxial failure envelope in Figure 7.7. If the maximum principal tension exceeds this value, cracking will occur along a plane normal to the maximum principal stress direction. It is assumed that the cracked concrete can no longer carry any tensile forces perpendicular to the crack. However, it was assumed that the irregular surface of crack could transfer a certain amount of shear depending on the value of β , the shear retention factor. A value of $\beta = 0.4$ is assumed in this investigation. The cracked masonry is assumed to be an orthotropic material with the principal axes of orthotropy (X^*-Y^*)(Figure 7.8) normal and tangent to the assumed crack direction. Under those conditions the material stiffness matrix for cracked component in the local principal coordinate system is

$$D_{cro} = \frac{E}{1 - \nu^2} \begin{vmatrix} 0 & 0 & 0 \\ 0 & 1 & 0 \\ 0 & 0 & \frac{\beta(1-\nu)}{2} \end{vmatrix} \quad (7.22)$$

where β equals shear retention factor ($0 \leq \beta \leq 1$). Thus,

$$\{\sigma^*\} = [D_{cro}] \{\epsilon^*\} \quad (7.23)$$

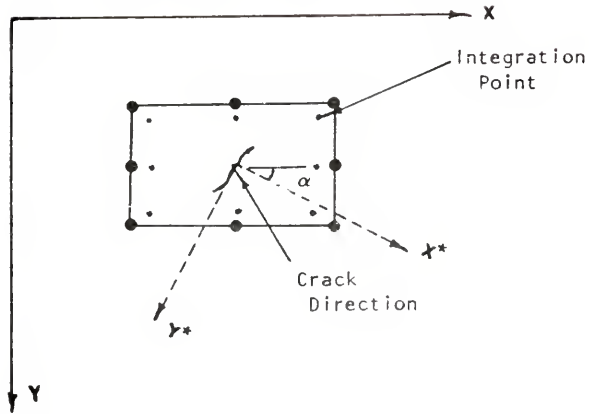


Fig. 7.8. Cracking at an integration point.

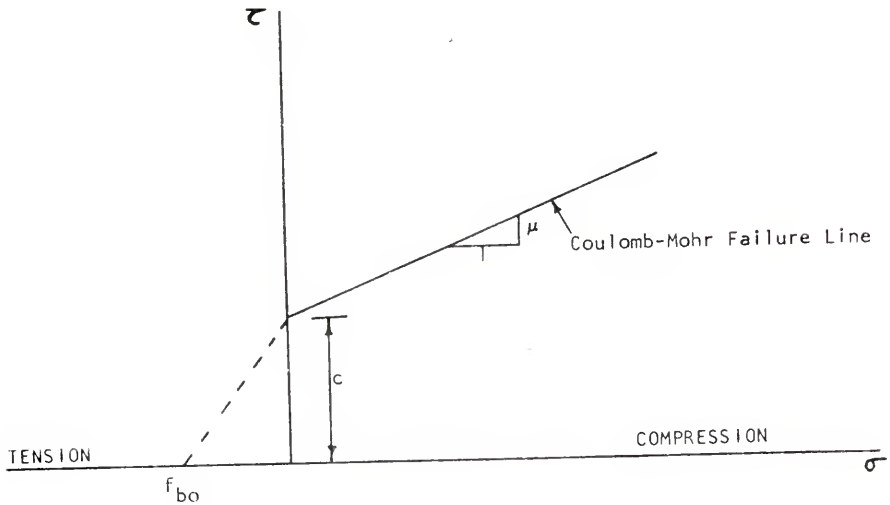


Fig. 7.9. Bond strength criterion.

However, the rigidity matrix in Equation (7.22) must be referred to the x-y frame of reference. The stresses and strains in the $X^* - Y^*$ frame are related to the corresponding values in the X-Y frame through the relationships:

$$\{\sigma^*\} = [T_\sigma] \{\sigma\} \quad (7.24)$$

$$\{\epsilon^*\} = [T_\epsilon] \{\epsilon\} \quad (7.25)$$

where $[T_\sigma]$ and $[T_\epsilon]$ are the stress and strain transformation matrices, respectively. Substituting Equations (7.24) and (7.25) into Equation (7.23) yields

$$[T_\sigma] \{\sigma\} = [D_{cro}] [T_\epsilon] \{\epsilon\}$$

or,

$$\{\sigma\} = [T_\sigma]^{-1} [D_{cro}] [T_\epsilon] \{\epsilon\} \quad (7.26)$$

As the work done by stresses on strains should be the same in the global and local systems, it can be shown that $[T_\sigma]^{-1}$ equals $[T_\epsilon]^T$. Therefore,

$$\{\sigma\} = [T_\epsilon]^T [D_{cro}] [T_\epsilon] \{\epsilon\} \quad (7.27)$$

and the rigidity matrix for the cracked point in the x-y frame is:

$$[D_{cr}] = [T_{\epsilon}]^T [D_{cro}] [T_{\epsilon}] \quad (7.28)$$

Combining Equations (7.28), (7.22), and (7.17):

$$D_{cr} = \frac{E}{1 - \nu^2} \begin{vmatrix} \sin^4 \alpha + \delta (\sin 2\alpha)^2 & \text{sym} & \text{sym} \\ \sin^2 \alpha \cos^2 \alpha - \delta (\sin 2\alpha)^2 & \cos^4 \alpha + \delta (\sin 2\alpha)^2 & \text{sym} \\ -\sin^2 \alpha \frac{\sin 2\alpha}{2} - \delta \cos 2\alpha \sin 2\alpha & -\cos^2 \alpha \frac{\sin 2\alpha}{2} + \delta \cos 2\alpha \sin \alpha & \frac{(\sin 2\alpha)^2}{4} + \delta (\cos 2\alpha) \end{vmatrix} \quad (7.29)$$

If the masonry element had yielded plastically before it cracked, after cracking its stiffness is disregarded.

7.3.7 Bond Failure at the Interface between Mortar and Block: debonding of mortar joints may occur in two modes, a) compression-shear and b) tension-shear.

The failure criteria assumed are similar to those adopted by Buyukozturk and Nilson (8) for modelling the interface between mortar and coarse aggregate. As described in Chapter 3, the compression-shear bond strength can be

modelled by the Coulomb-Mohr failure theory (Figure 7.9).
 Debonding occurs when,

$$\zeta = \zeta_{lim} = c + \mu \sigma_n \quad (7.30)$$

where ζ equals shear stress at the interface, σ_n equals normal stress at the interface, c equals adhesion, and μ equals coefficient of friction between mortar and block.

It is assumed that the adhesion is lost when the strength of the interface is exceeded and sliding is resisted thereafter only by friction:

$$\zeta = \mu \sigma_n \quad (7.31)$$

Once ζ_{lim} is exceeded, to account for the loss of adhesion, zero shear modulus is assigned to the particular point. In the local coordinate system, the constitutive matrix at the point of occurrence of compression-shear crack is modified as follows:

$$[D_{cbo}] = \frac{E}{1 - \nu^2} \begin{vmatrix} 1 & \nu & 0 \\ \nu & 1 & 0 \\ 0 & 0 & 0 \end{vmatrix} \quad (7.32)$$

Equation (7.32) predicts that no shear can be transferred by the debonded unit. Since the stresses are resisted by friction in accordance with Equation (7.31), a correction

factor must be applied. Friction stresses are calculated depending upon the normal compression acting as given by Equation (7.31). These stresses were replaced by statically equivalent forces at the corners of the element, details of which are presented in the next chapter.

If the joints were inclined at an angle α to the X-axis, in order to calculate the normal compressive stress acting on the interface between mortar and block, the stresses have to be transformed to the local system and appropriate stresses considered (Figure 7.10) depending on the orientation of the joints. Also in this case, the matrix $[D_{cbo}]$ has to be transformed to the global system to obtain the global constitutive matrix $[D_{cb}]$ for the debonded point. Using Equation (7.28),

$$[D_{cb}] = \frac{E}{1 - \nu^2} \begin{vmatrix} \cos^4\alpha + 2\nu\sin^2\alpha\cos^2\alpha + \sin^4\alpha & \nu(\cos^4\alpha + \sin^4\alpha) + 2\cos^2\alpha\sin^2\alpha & \frac{1-\nu}{2} \sin^2\alpha\cos^2\alpha \\ \text{sym} & \text{sym} & \\ \sin^4\alpha + \cos^4\alpha + 2\nu\sin^2\alpha\cos^2\alpha & \text{sym} & \\ \left(\frac{\nu-1}{2}\right) \sin 2\alpha\cos 2\alpha & 2(1-\nu)\sin^2\alpha\cos^2\alpha & \end{vmatrix}$$

(7.33)

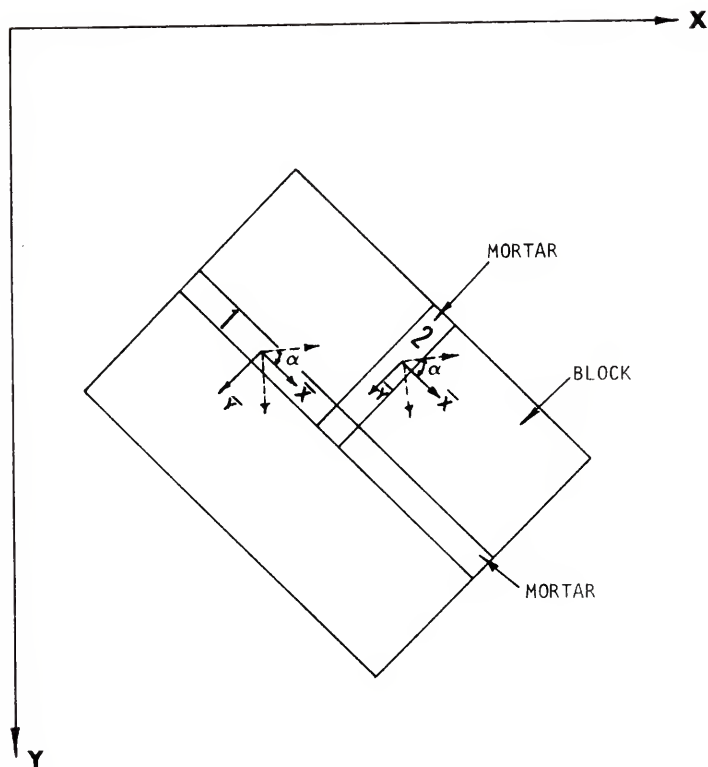


Fig. 7.10. Normal stresses acting on interface of inclined mortar joints.

Presently, there is no information on the tension-shear strength of the interface. However, the modulus of rupture tests described in Chapter 2 provide values for flexural tensile bond strength of the mortar joint. These values are assumed as applicable to pure tension, and a straight line variation between the pure tension and pure shear failure points is assumed as criterion for predicting the tension-shear strength of the interface (Figure 7.9).

Due to the nature of the tension-shear crack, no shear or normal stress can be transmitted across the interface after cracking, although compression or tension parallel to the crack can be carried. Thus, the local constitutive matrix for mortar joint type (1) becomes:

$$\begin{Bmatrix} \sigma_x \\ \sigma_y \\ \tau_{xy} \end{Bmatrix} = \frac{E}{1 - \nu^2} \begin{vmatrix} 1 & 0 & 0 \\ 0 & 0 & 0 \\ 0 & 0 & 0 \end{vmatrix} \begin{Bmatrix} \epsilon_x \\ \epsilon_y \\ \gamma_{xy} \end{Bmatrix} \quad (7.34)$$

Transformed to global coordinates, the constitutive matrix is:

$$D_{tb} = \frac{E}{1 - \nu^2} \begin{vmatrix} (1-\nu^2)\cos^4\alpha & \text{sym} & \text{sym} \\ (1-\nu^2)\sin^2\alpha\cos^2\alpha & (1-\nu^2)\sin^4\alpha & \frac{(1-\nu^2)\sin^2\alpha\sin 2\alpha}{2} \\ (1-\nu^2)\cos^2\alpha\frac{\sin 2\alpha}{2} & (1-\nu^2)\sin^2\alpha\frac{\sin 2\alpha}{2} & \frac{(1-\nu^2)(\sin 2\alpha)^2}{4} \end{vmatrix} \quad (7.35)$$

For joint type (2), the local constitutive matrix is:

$$\begin{Bmatrix} \sigma_x \\ \sigma_y \\ \tau_{xy} \end{Bmatrix} = \begin{vmatrix} 0 & 0 & 0 \\ 0 & 1 & 0 \\ 0 & 0 & 0 \end{vmatrix} \begin{Bmatrix} \varepsilon_x \\ \varepsilon_y \\ \gamma_{xy} \end{Bmatrix} \quad (7.36)$$

Transformed to global coordinates, the constitutive matrix is:

$$D_{tb} = \frac{E}{1 - \nu^2} \begin{vmatrix} (1-\nu^2)\sin^4\alpha & \text{sym} & \text{sym} \\ (1-\nu^2)\sin^2\alpha\cos^2\alpha & (1-\nu^2)\cos^4\alpha & (\nu^2-1)\cos^2\alpha\frac{\sin 2\alpha}{2} \\ (\nu^2-1)\sin^2\alpha\frac{\sin 2\alpha}{2} & (\nu^2-1)\cos^2\alpha\frac{\sin 2\alpha}{2} & (1-\nu^2)\frac{(\sin 2\alpha)^2}{4} \end{vmatrix} \quad (7.37)$$

7.3.8 Yielding of Reinforcement: using Equation (7.16), the stress in steel can be determined. If the stress in steel exceeds the yield limit, then E_s equals zero in Equation (7.15), and the equivalent modulus is modified for subsequent increments.

CHAPTER 8

ANALYSIS AND EXAMPLES

8.1 Method of Solution: The finite element method used in this analysis is of the displacement type and is applied in an incremental form. Initial elastic analysis continues until either cracking or plasticity occurs. The "initial stress" approach is adopted to redistribute the released stresses due to cracking or plasticity to the surrounding elements. In this analysis, the initial stiffness is used throughout each iterative cycle as well as through all the load increments. The method is schematically illustrated in Figure 8.1. Load R_1 is applied and a deflection U_1 is computed using the initial elastic stiffness K_1 . It was found that some points have failed at this level. This changes the stiffness matrix to K_2 . The ordinate A_1D_1 represents the load released due to failure of some elements (Q_1). Reloading the structure with Q_1 causes additional displacements ΔU_1 and also additional cracking reducing the structure stiffness to K_3 . However, since the same initial stiffness K_1 was used again, the reloaded path (dotted lines) is D_1B_1 instead of D_1A_2 . The unbalanced load on the structure is B_1D_2 . The process is continued until no further cracking occurs and the unbalanced force is within a predetermined limit.

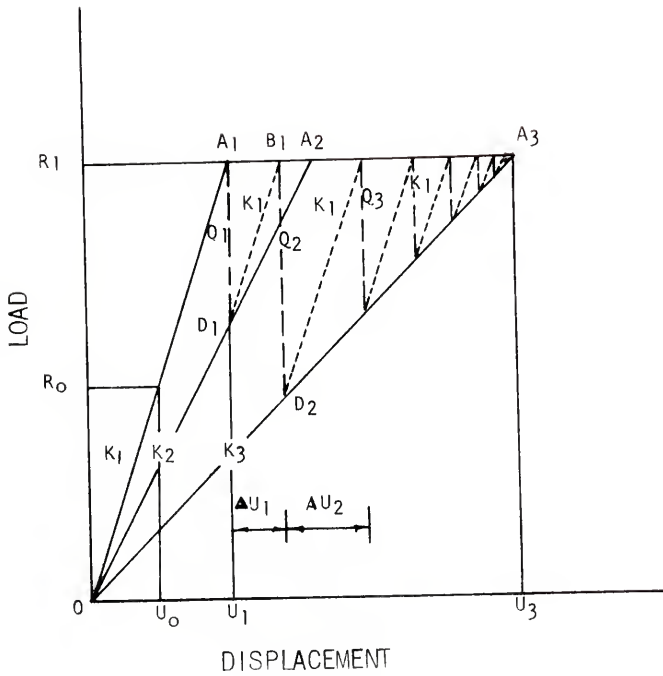


Fig. 8.1. Schematic diagram illustrating the nonlinear analysis adopted.

8.2 Computational Procedure: Stresses and strains are computed at Gaussian integration points. Three types of arrangements were adopted. For very narrow elements, the stresses were computed only at the three Gauss points along its longer centroidal axis. However, when the aspect ratios were smaller, the stresses were calculated at all the nine points. For a typical load increment 'i', the following procedure is adopted:

1) The incremental displacements $\Delta\delta_i$ and the total displacements δ_i are computed. The incremental strains $\Delta\epsilon_i$ are also computed.

2) If the Gauss point has not failed earlier due to cracking, crushing, or debonding, incremental stresses $\Delta\sigma_i$, total stresses σ_i , and the principal stresses and their direction are computed.

3) The minimum principal strain at the Gauss point is checked to see whether it exceeds the ultimate compressive strain of the component. If it does, then crushing occurs and the entire stress vector at the point ($\sigma_{i-1} + \Delta\sigma_i$) is converted into equivalent nodal forces by using:

$$\{Q_1^e\} = \int \{B\}^T (\sigma_{i-1} + \Delta\sigma_i) d(\text{vol}) \quad (8.1)$$

No further computations are made at this point in subsequent increments.

4) If both principal stresses are compressive, it is verified if the peak stress exceeds the biaxial compressive strength of the component. In which case, the point is assumed to be crushed and all the stresses are released as in the previous case. If not, the next step is executed.

5) If the point has not failed before in other modes, then it is checked for compressive yielding:

a) The vector $(\sigma_{i-1} + \Delta\sigma_i)$ is checked against the von Mises yield criterion F . If $F < 0$, then the point is still in the elastic state and step (8) is executed.

b) If $F > 0$ for the first time, the value of F at the start of the interval is computed and the proportion of the elastic stress and strain increment which has taken place in the range above the yield point is determined by interpolation so that the stress vector is now on the yield surface. For the above values of elastic stress, the corresponding elasto-plastic stress increment is computed using Equation (7.20a). If $\Delta\epsilon_{i-1}^1$ is the elastic strain increment added to ϵ_{i-1} to obtain the stress vector on the yield surface, the additional stress $\Delta\sigma_i^1$ compatible with the strain $(\Delta\epsilon_i - \Delta\epsilon_{i-1}^1)$ is obtained from $[D_{ep}]$:

$$\Delta\sigma_i^1 = [D_{ep}] (\Delta\epsilon_i - \Delta\epsilon_{i-1}^1) \quad (8.2)$$

where $[D_{ep}]$ is the elasto-plastic matrix.

The stress and strain vectors are then updated to be:

$$\sigma_i^p = \sigma_{i-1}^1 + \Delta\sigma_i^1 \quad (8.3)$$

$$\epsilon_i = \epsilon_{i-1} + \Delta\epsilon_i \quad (8.4)$$

where σ_{i-1}^1 equals the stress vector compatible with $F = 0$.

If yielding at the Gauss point has occurred during an earlier iteration or load increment, the compatible $\Delta\sigma_i^1$ is computed directly as:

$$\Delta\sigma_i^1 = [D_{ep}] \Delta\epsilon_i \quad (8.5)$$

The updated stress and strain vectors are then evaluated as:

$$\sigma_i^p = \sigma_{i-1}^1 + \Delta\sigma_i^1 \quad (8.6)$$

$$\epsilon_i = \epsilon_{i-1} + \Delta\epsilon_i \quad (8.7)$$

As the load increment is finite, it is possible for the stress calculated by Equations (8.3) and (8.6) to exceed slightly the yield condition. This is tested, and if excess found, stresses are scaled down to remain on the yield surface (σ_i).

The initial stresses $(\Delta\sigma_i - (\sigma_i - \sigma_{i-1}))$ are converted into equivalent nodal forces for the element:

$$\{Q_2\}^e = \int \{B\}^T (\Delta\sigma_i - (\sigma_i - \sigma_{i-1})) d(vol) \quad (8.8)$$

6) If both principal stresses are tensile, and if the maximum principal stress does not exceed the limiting tensile strength of the component, then step (8) is executed. Otherwise, the Gauss point is assumed to have cracked normal to the direction of the maximum principal stress during this iteration and this crack direction is locked in. Using the elasto-plastic matrix for the cracked point, the compatible stress vector is computed as:

$$\{\Delta\sigma_i\}^1 = [D_{cr}] \{\Delta\epsilon_i\} \quad (8.9)$$

The initial stresses to be supported by the equivalent nodal forces are:

$$\{\Delta\sigma_i\}'' = (\{\Delta\sigma_i\} - \{\Delta\sigma_i\}^1) \quad (8.10)$$

The corresponding nodal forces are:

$$\{Q_3\}^e = \int \{B\}^T \{\Delta\sigma_i\}'' d(vol) \quad (8.11)$$

7) In the biaxial tension-compression case, the appropriate failure criteria are applied to detect cracking. If none is found, then step (8) is executed. Otherwise, the same procedure outlined in step (6) is followed.

8) It is verified whether the point under consideration is in a mortar joint. If not, step (9) is executed.

The stresses are transformed to coordinate axes corresponding to centroidal axes of the joints. The nature of the stress normal to the interface between mortar and block determines the mode of failure in case the shear stress exceeds the limiting shear stress under the corresponding conditions. Using the appropriate elasto-plastic matrix (D_{cb} or D_{tb}), compatible stresses are calculated.

The initial stresses for the case of no previous shear-compression debonding are:

$$\{\Delta\sigma_i\}'' = (\{\Delta\sigma_i\} - [D_{cb}]\{\Delta\epsilon_i\}) \quad (8.12)$$

The shear stresses resisted by friction, $\mu\sigma_n$, are added to the shear stress component of the initial stresses, where σ_n is the normal compressive stress on the joint.

The equivalent nodal forces are then calculated as:

$$\{Q_5\}^e = \int \{B\}^T \{\Delta\sigma_i\}'' d(vol) \quad (8.13)$$

Similar criteria are applied for shear-tension debonding.

9) If the point under investigation happens to be an element containing steel reinforcement, the stresses are checked for the yielding of reinforcement. If yielding occurs, then the equivalent modulus of the element is modified.

10) Steps (1) through (9) are carried out for each Gauss point in an element and for each element in the structure. All the released element nodal forces are stored in their appropriate global locations. Thus,

$$\{Q\} = \sum_{\substack{\text{All} \\ \text{Elements}}} (Q_1^e + Q_2^e + Q_3^e \dots) \quad (8.14)$$

If all the elements of $\{Q\}$ are less than a predetermined value, then the next load increment is applied and steps (1) through (10) repeated. If not, the nodal forces $\{Q\}$ are applied and steps (1) through (10) repeated. This process is continued until all elements of $\{Q\}$ are below the predetermined allowable nodal load which is considered to be negligible compared to the increment of load applied.

8.3 Computer Program: Figure 8.2 shows the general flow chart of the program adopted. Figure 8.3 shows the flow diagram for the computational procedure outlined in the previous section. A modified Gaussian Elimination procedure was adopted for solving the equations (vide Appendix A).

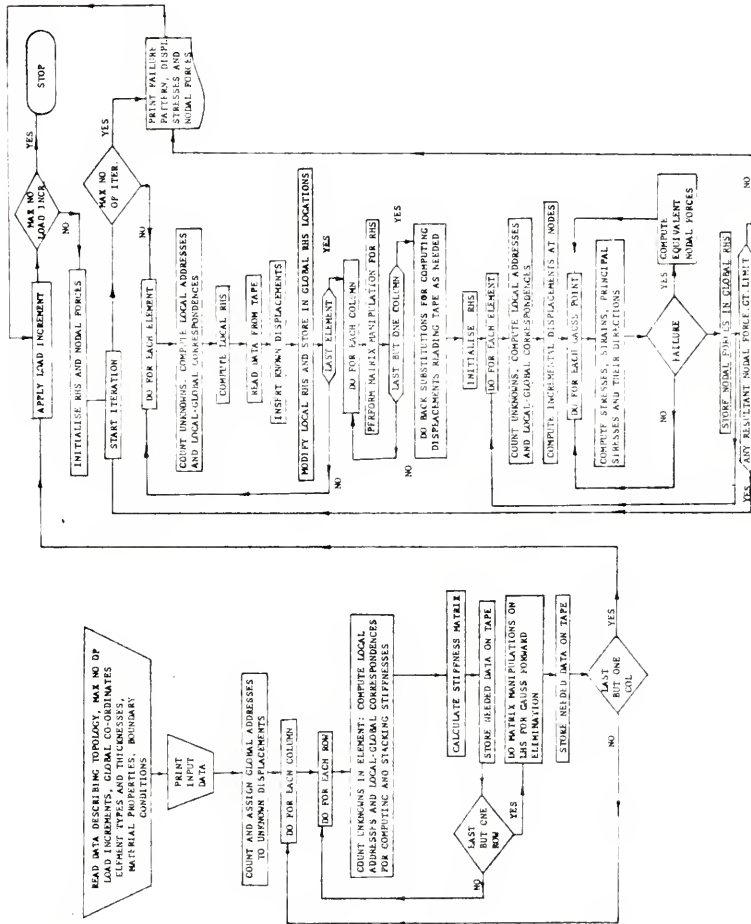


Fig. 8.2. General flow chart of the program.

8.4 Examples of Nonlinear Analysis: The descriptions of several test problems are now presented. The details of the data deck required for each problem are omitted. This information is given for one typical example in Appendix B in the form of a sample computer output.

8.4.1 Square Concrete Panel under Diagonal Compression: this example was chosen to check the program. A square concrete panel tested by Blume and Proulx (6) was considered for analysis. The panel measured 48" x 48" x 6" and had no reinforcement. The compressive strength of concrete (f_c') used was 4350 psi. The data concerning the modulus of elasticity and tensile strength were not provided. The above values were assumed, adopting the equations furnished in the ACI Standard 318-71. Assuming the unit weight of concrete (w) as 140 lb/cu ft,

$$E = w^{1.5} 33\sqrt{f_c'} = 3.6 \times 10^6 \text{ psi}$$

Splitting tensile strength equals $6.7\sqrt{f_c'} = 440 \text{ psi}$.

The maximum experimentally observed shear stress for the panel was 413.5 psi and the corresponding load 168,416 lbs. The mode of failure for the panel was a crack along the loaded diagonal (vertical diagonal).

Figure 8.4 shows the finite element idealization adopted for the panel. The stresses were determined at the

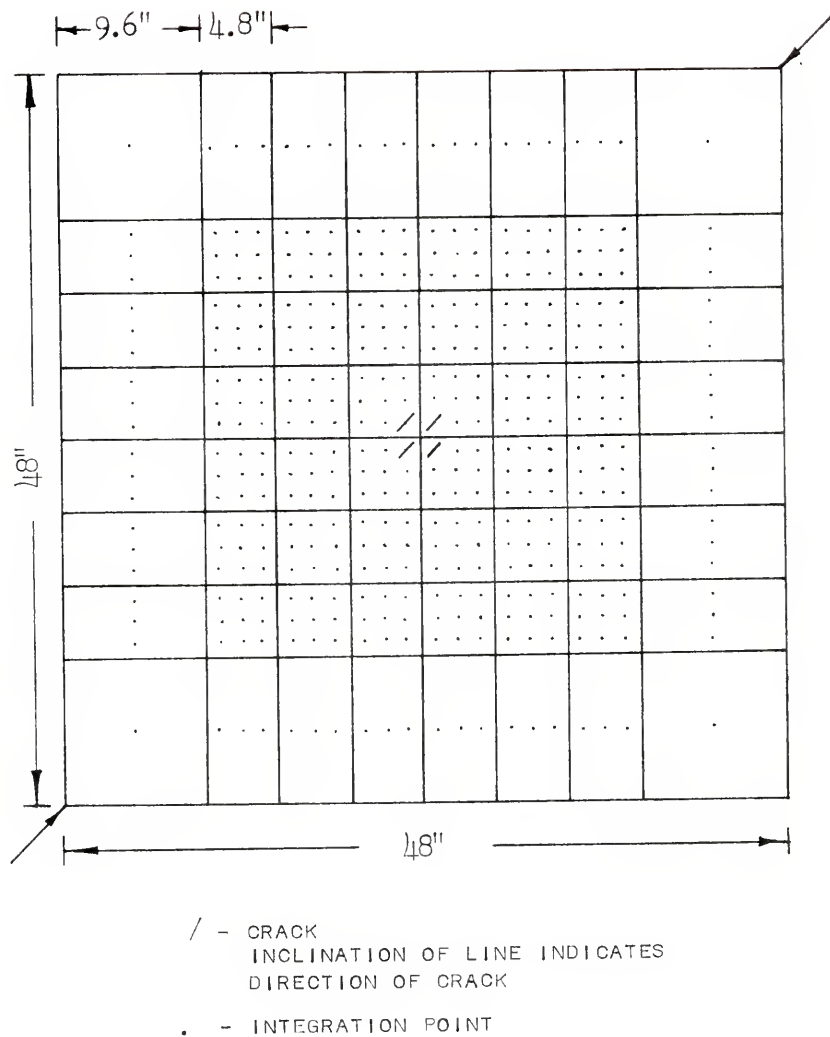


Fig. 8.4. Crack pattern of square concrete panel at 195,000 lbs.

Gauss points (marked '.'). The load was applied in increments of 1,000 lbs, from 190,000 lbs. No cracks were detected till the load reached 195,000 lbs. The first cracks corresponding to this load are indicated in Figure 8.4. All the cracks were parallel to the loaded diagonal. The forces released due to the cracks were checked to see whether they were within the predetermined value of 100 lbs. If so, the next increment was applied. The crack propagation is illustrated in Figures 8.4 through 8.8. When the load reached 199,000 lbs, more points started cracking, releasing large forces at the nodal points. No convergence was obtained at the end of six cycles, indicating failure. It is evident from Figure 8.8 that the analysis predicted a band of cracking region, unlike a single line of crack along the loaded diagonal. The ultimate load predicted by the analysis was 18.2% higher than the experimental value obtained by Blume and Proulx (6). If the value of tensile strength assumed were reduced by 10%, the load corresponding to the initial crack would be 175,500 lbs. A 10% variation in split cylinder strength could be anticipated. However, the analysis predicted closely the crack propagation observed in the experiment.

The solution time for this problem was 73.35 seconds in IBM 370 for the required storage space of 384 k-bytes.

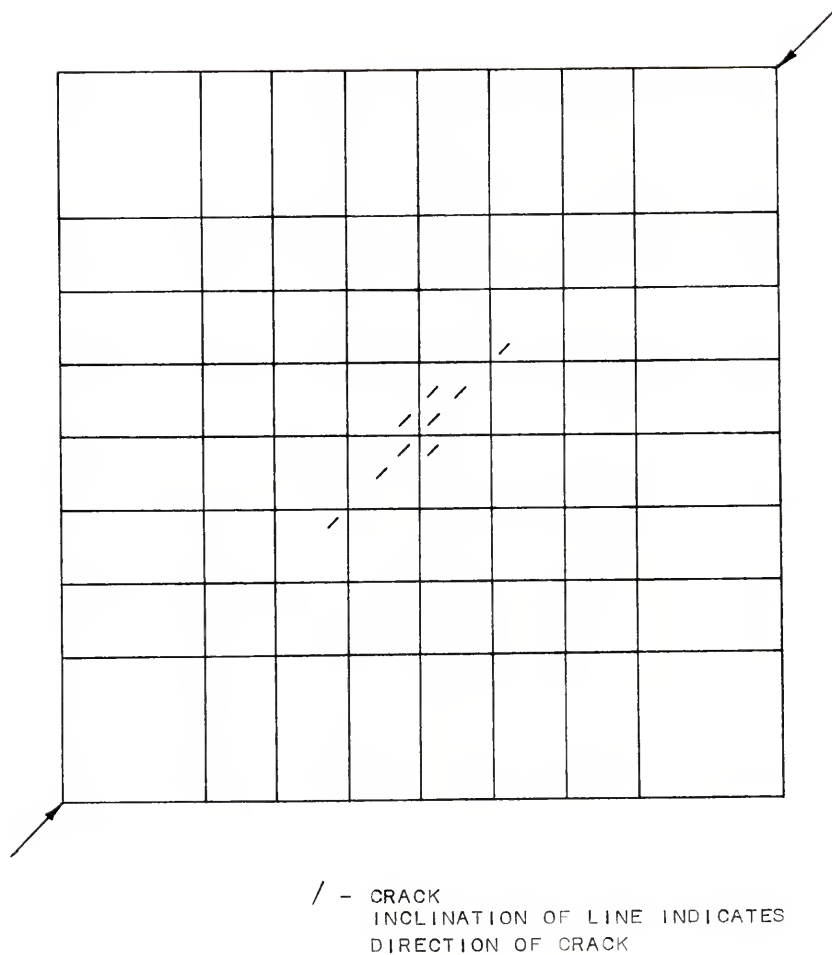


Fig. 8.5. Crack pattern of square concrete panel at 196,000 lbs.

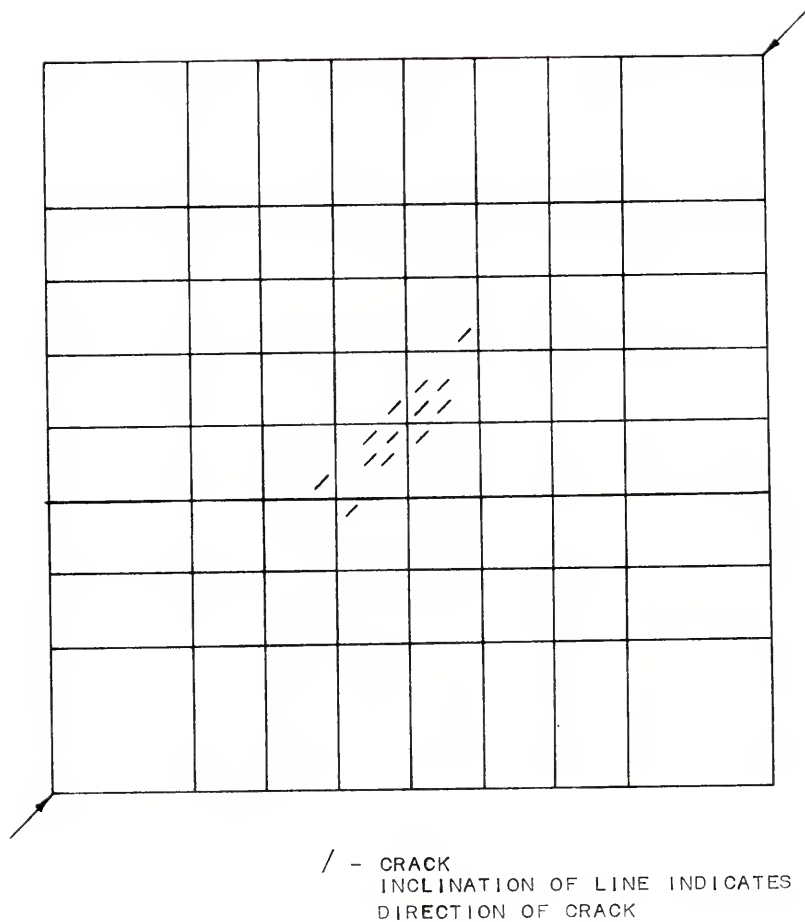


Fig. 8.6. Crack pattern of square concrete panel at 197,000 lbs.

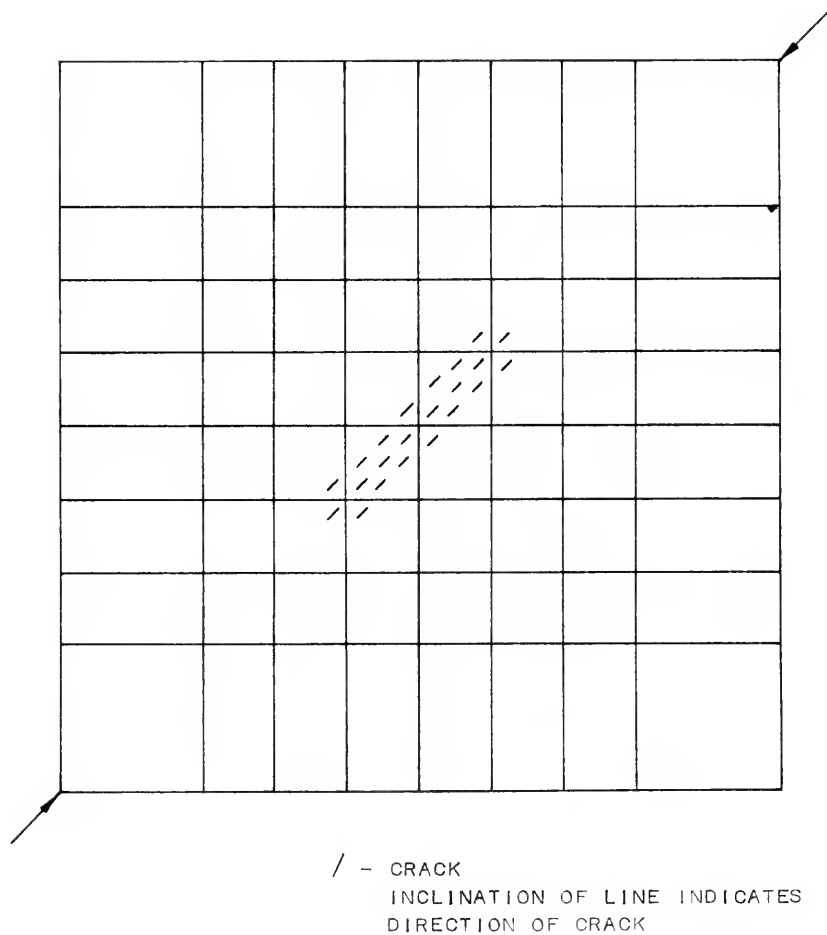


Fig. 8.7. Crack pattern of square concrete panel at 198,000 lbs.

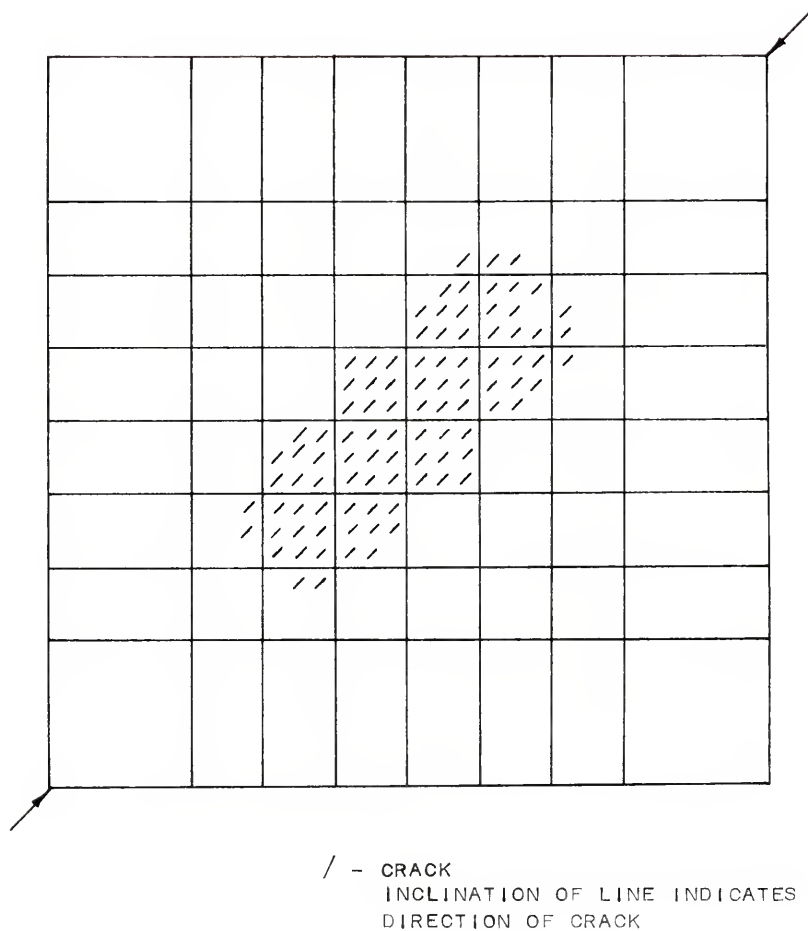


Fig. 8.8. Crack pattern of square concrete panel at 199,000 lbs.

8.4.2 Hollow Concrete Masonry Panels under Diagonal Compression: three hollow concrete masonry panels were considered. These panels were made using the model concrete blocks and mortars MS or MW. The configurations of the panels and their experimental failure modes are shown in Figure 8.9. All the panels failed by debonding of mortar joints. For panels MS and SM, model mortar type MS was used. For panel MW, model mortar type MW was used. The properties of the mortar and blocks are given in Chapter 2. The experimental values of maximum loads for panels SM, MS, and MW were 300 lbs, 600 lbs, and 350 lbs, respectively.

In the finite element analysis, the values of cohesion and coefficient of friction for the model mortars were assumed to be the same as those given by Equations 3.1 and 3.2, respectively, for mortars MW and MS. Similarly, equations 3.3 and 3.4 were assumed for obtaining the modulus of rupture values. Since the panels were hollow and mortar joints were fully bedded, an equivalent thickness, corresponding to the net area of the block was adopted for analysis. This thickness was calculated as the net area of the block divided by the length of the block. A value of 1.073" was assumed in the analysis.

Figure 8.10 shows the finite element discretization adopted for panel SM. Load was applied in increments of 20 lbs, starting from 250 lbs. No failure was detected

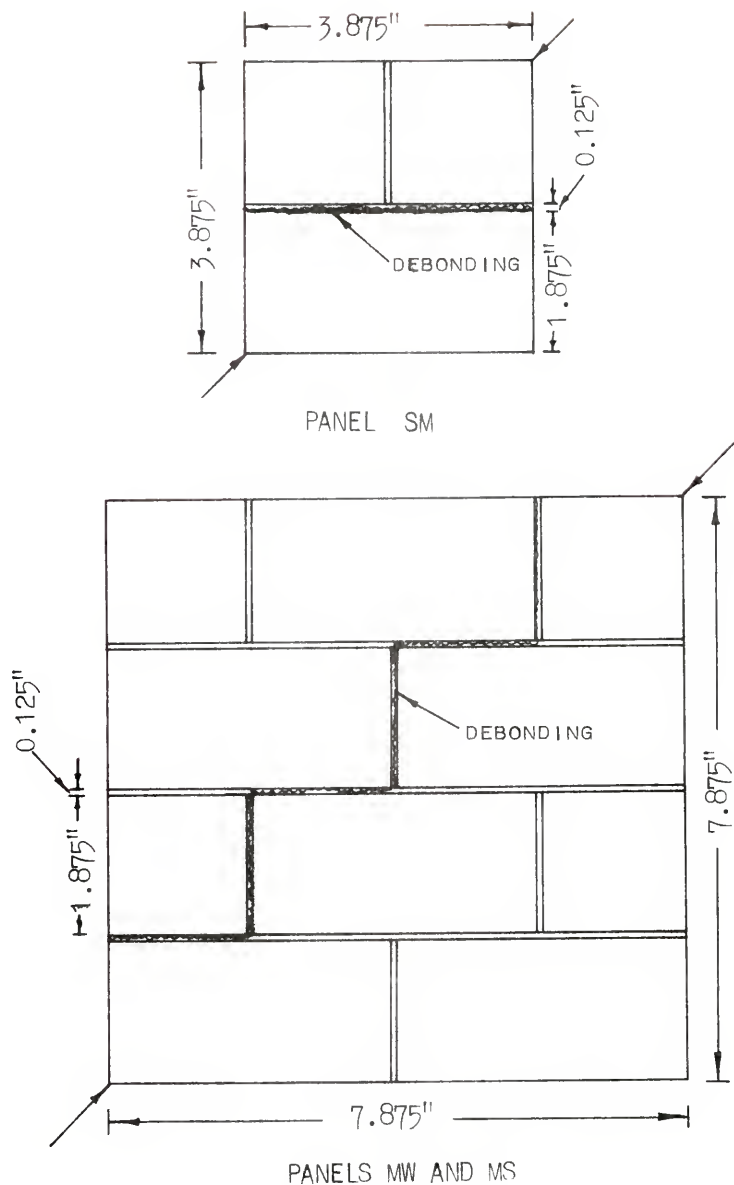


Fig. 8.9. Experimentally observed failure modes in hollow concrete masonry panels.

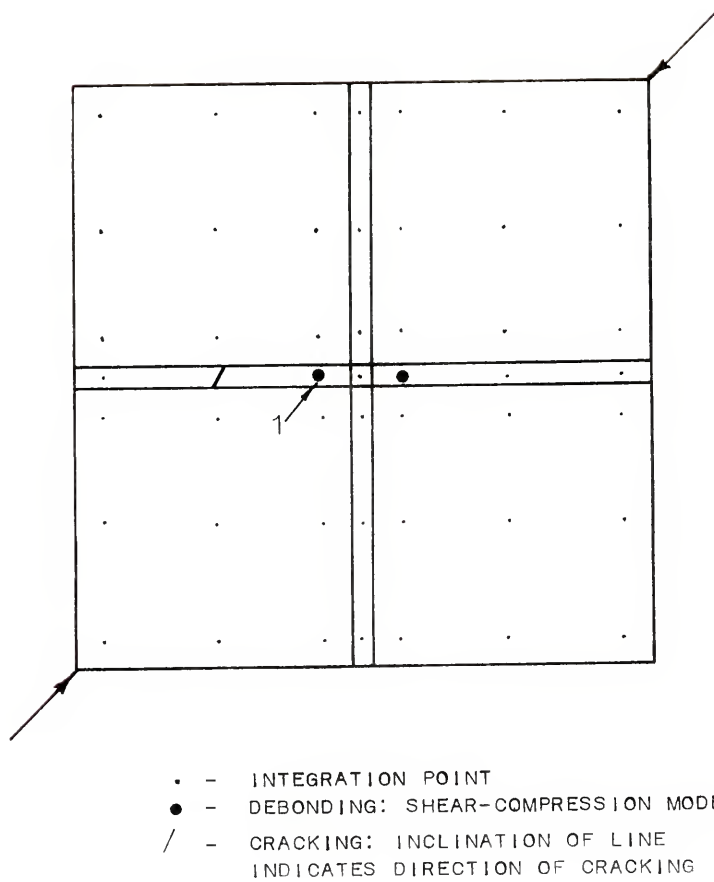


Fig. 8.10. Predicted failure pattern for panel SM.

till the load was 290 lbs. At this load, point 1 (Figure 8.10) failed by compression-shear-debonding. With the nodal forces released due to failure at point 1, the second iteration was performed. This led to the failure of other points shown in Figure 8.10. The next iteration led to the failure of a large number of points and no convergence was obtained, marking failure. In order to check this failure load, the load increment was reduced to 10 lbs. In this case, also, the first failure occurred at 290 lbs and no convergence was obtained.

Even though the predicted failure mode did not agree well with the experimental one, the predicted load of 290 lbs was close to the average experimental value of 300 lbs.

The finite element discretizations for panels MS and MW are shown in Figures 8.11 and 8.12, respectively. In both cases, the load was applied at 20 lb increments. As in the case of panel SM, no failure was detected until a particular load was reached and subsequent iterations at the same load level did not converge, indicating failure. The failure patterns shown correspond to the first two iterations.

It is evident that the complete failure pattern could not be predicted in either case. However, the values of failure load predicted were quite close. For panel MS, the predicted load of 610 lbs was nearly the same as the experimental value of 600 lbs. For panel MW, the

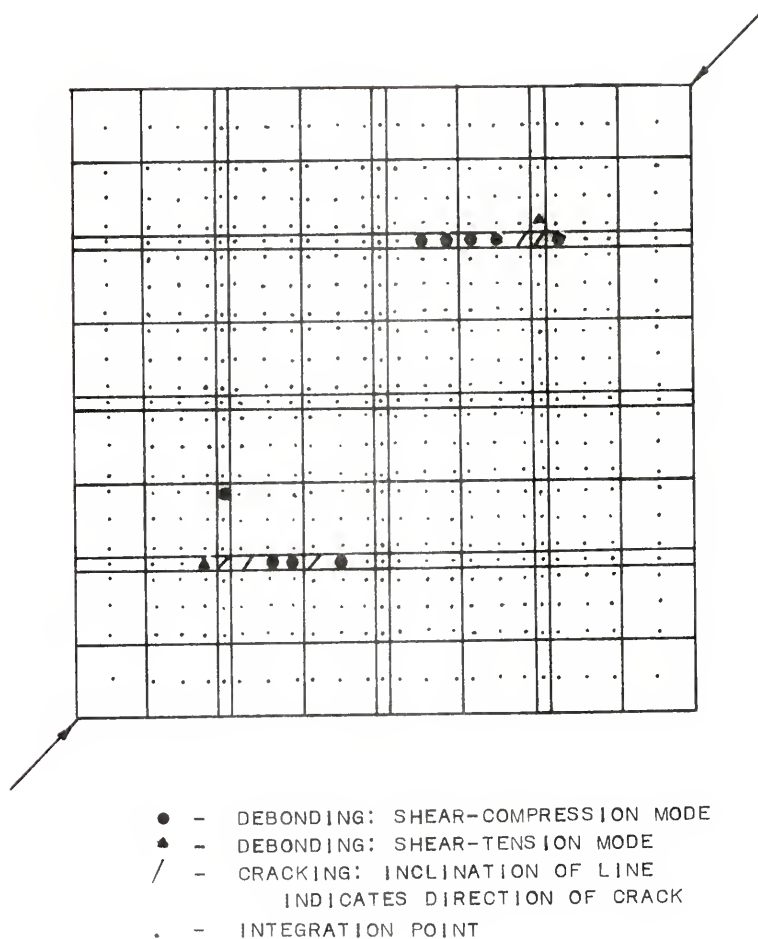
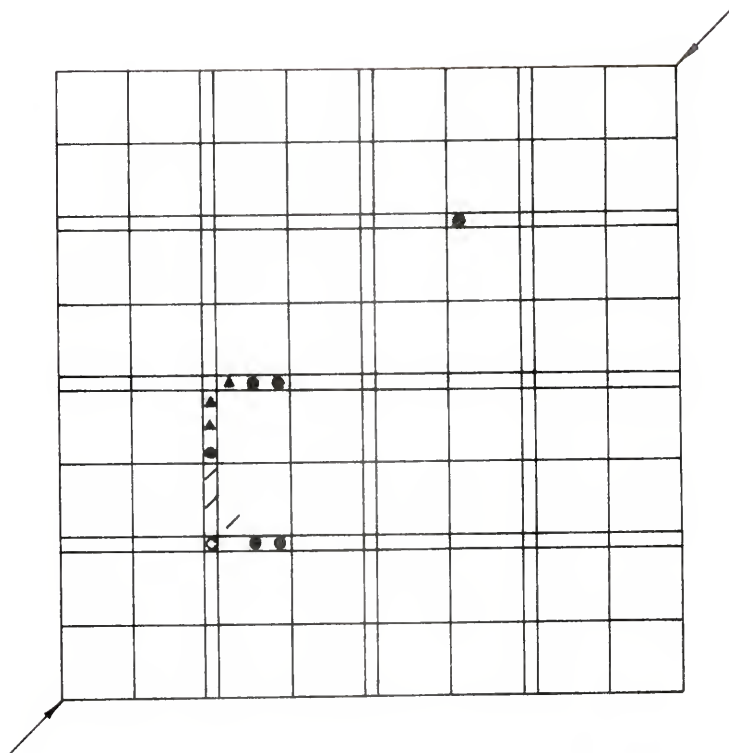


Fig. 8.11. Predicted failure pattern for panel MS.



- - DEBONDING: SHEAR-COMPRESSION MODE
- ▲ - DEBONDING: SHEAR-TENSION MODE
- - CRUSHING
- / - CRACKING: INCLINATION OF LINE
INDICATES DIRECTION OF CRACK

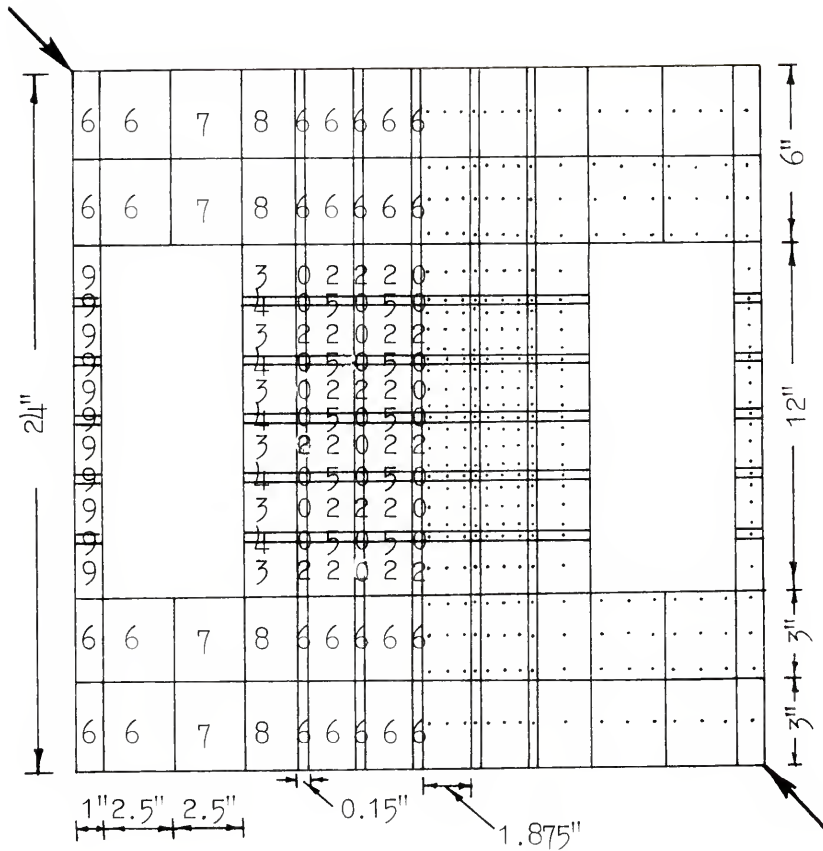
Fig. 8.12. Predicted failure pattern for panel MW.

corresponding values are 370 lbs and 350 lbs. The solution time for MS and MW were 115 seconds and 118 seconds, respectively.

8.4.3 Grouted Masonry Piers: this example considers the tests on model piers described in Chapter 4. The pier chosen was PR 3. The properties of grout, mortar, spandrel concrete, etc. are summarized in Chapter 2. It can be noted that the tensile strengths of the grout and block were nearly equal.

Figure 8.13 shows the finite element discretization adopted for the pier. The numbers indicate the codes for the material types. Table 8.1 summarizes the material properties adopted in the analysis. For tensile cracking at a point, the maximum principal stress should exceed the tensile strength of the weaker component. Accordingly, the value of σ_t was chosen. The equivalent modulus was calculated as described in Chapter 7.

A preliminary analysis predicted failure at about 30% of the experimentally obtained failure load because of the debonding of few vertical and horizontal joints. Since the grouted element consists of two materials in each element, the problem is really three dimensional in character. In the model tests, no debonding failure was observed prior to diagonal cracking. Hence, it was decided to omit the debonding mode while analyzing grouted piers.



. - INTEGRATION POINT

Fig. 8.13. Finite element idealization for pier PR 3.

TABLE 8.1
MATERIAL PROPERTIES USED IN ANALYSIS OF PR 3

Material Code	E psi	ν	σ_o psi	σ_t psi	σ_r psi
0	1.90×10^6	0.2	656	200	42
2	2.08×10^6	0.2	760	205	
3	2.22×10^6	0.2	760	205	
4	1.93×10^6	0.2	656	200	
5	1.79×10^6	0.2	656	200	
6	4.78×10^6	0.25	2300	450	
7	5.18×10^6	0.25	2300	450	
8	5.10×10^6	0.25	2300	450	
9	2.10×10^6	0.25			

In the analysis, the diagonal compressive load was applied in increments of 50 lbs. No failure was observed till the load was 3,800 lbs. At 3,850 lbs, the center point of the pier cracked first (marked '9' in Figure 8.14). The crack direction was parallel to the loaded diagonal. At the same load level, during the second iteration due to the loads released by the first cracking, four more points (marked '2') cracked in a direction parallel to the loaded diagonal. The third iteration, with loads due to the released forces, produced the subsequent crack pattern shown in Figure 8.10. Due to the large magnitude of forces released (30,000 lbs to 100,000 lbs), no convergence was obtained. Thus, the collapse load was taken as 3,850 lbs. The experimental value obtained was 4,740 lbs. Considering the variability of the phenomenon, the predicted value can be considered satisfactory. The predicted failure mode includes a band of cracks parallel to the loaded diagonal instead of a few well-defined cracks obtained in the test. However, the initial crack propagation is well-predicted. The subsequent analytical divergence led to the irregularities in the crack pattern.

Figure 8.15 shows the analytical and experimental load deflection curves obtained. The analytical solution presented a much stiffer structure than the actual one. A similar conclusion was drawn by Cervenka and Gerstle in their analysis of a reinforced concrete shear panel (10).

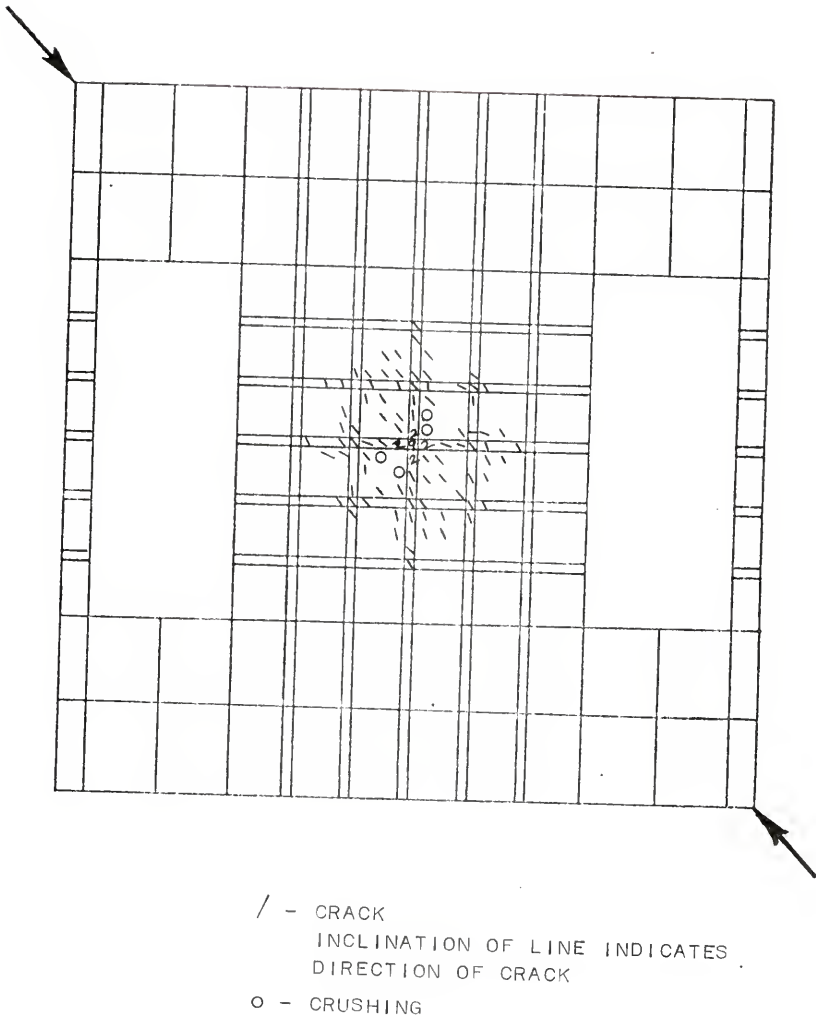


Fig. 8.14. Predicted crack pattern for PR 3.

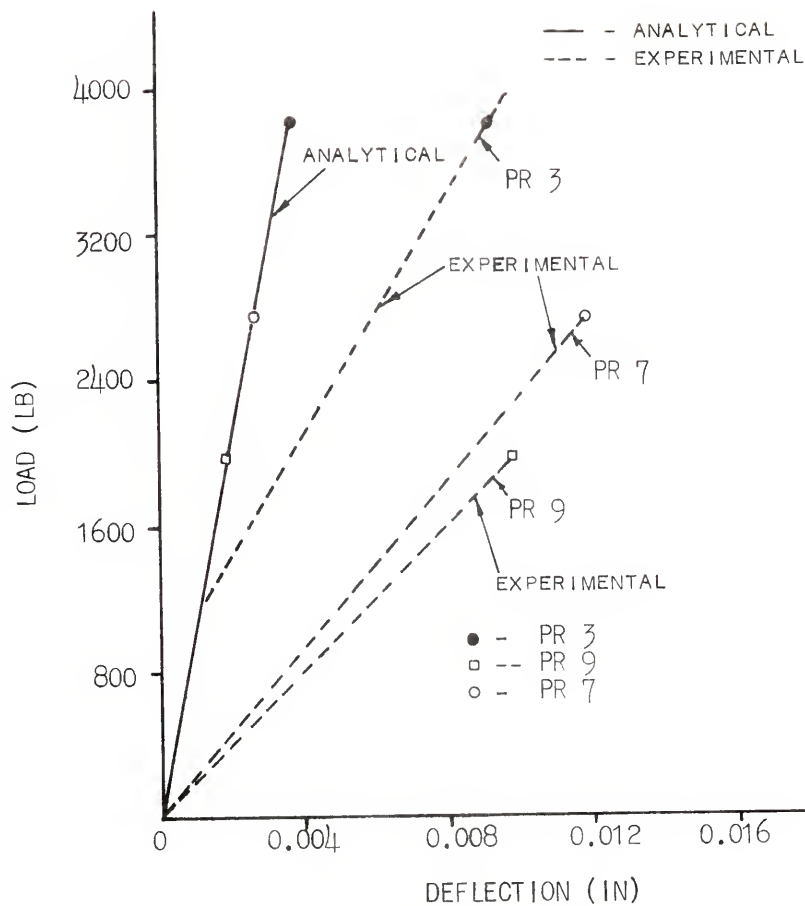


Fig. 8.15. Analytical and experimental load-deflection curves for grouted piers.

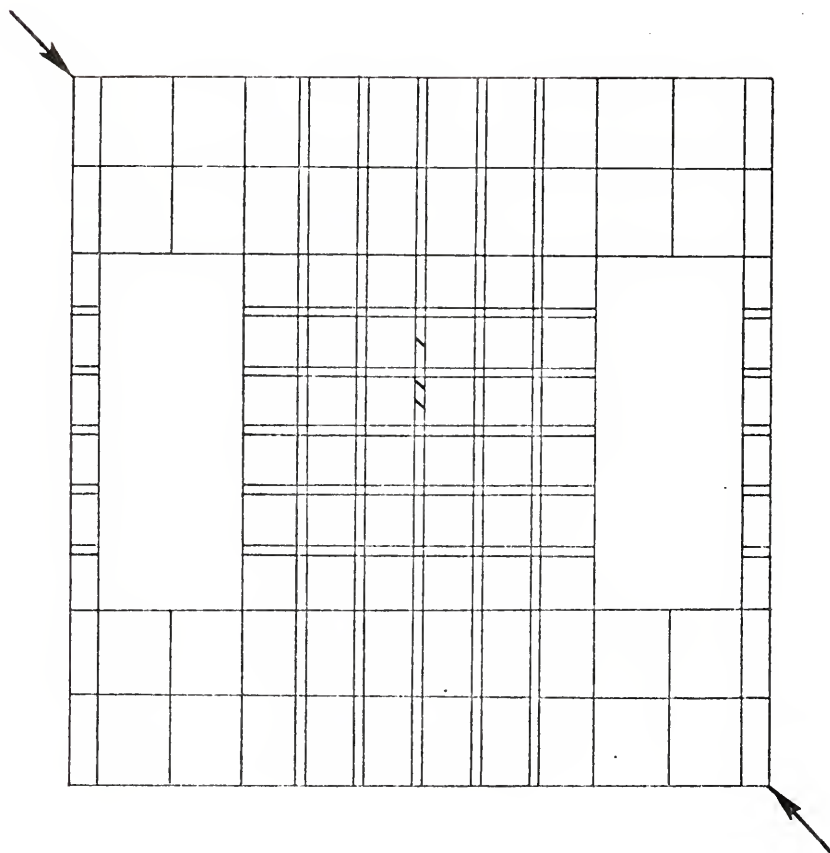
The solution time for the analysis of PR 3 was 250 seconds for seven load increments of 50 lbs, from 3,500 lbs.

Other piers considered for analysis were PR 7 and PR 9. Table 8.2 shows the material properties used in the analysis of PR 7. When the debonding failure mode was considered, failure occurred at 1,000 lbs. When it was not considered, the failure occurred at 2,500 lbs, still well below the experimental value of 5,600 lbs. The failure criteria, based on the weaker component, apparently were not satisfactory because of the two different material properties involved in each element. In the absence of data concerning the actual distribution of stresses in grout and mortar, a trial run was initiated adopting an equivalent tensile strength on the basis of the areas of the components. These values are shown in parentheses in Table 8.2. The analysis was performed by applying load in increments of 50 lbs, starting from 2,500 lbs. Complete collapse occurred at 2,750 lbs, about 50% of the experimental value. The points failed during the first two iterations are shown in Figure 8.16.

The material properties used in the analysis of PR 9 are shown in Table 8.3. Since, in this case, the grout was weaker than both mortar and block, the tensile strength of grout was the governing criterion for cracking. The analysis was performed by applying load at 50 lb increments

TABLE 8.2
MATERIAL PROPERTIES USED IN ANALYSIS OF PR 7

Material Code	E psi	ν	σ_o psi	σ_t psi	σ_r psi
0	1.25×10^6	0.2	485	135	30
2	2.16×10^6	0.2	2688	260 (288)	
3	2.30×10^6	0.2	2688	260 (288)	
4	1.65×10^6	0.2	485	135 (218)	
5	1.50×10^6	0.2	485	135 (218)	



/ - CRACK
INCLINATION OF LINE INDICATES
DIRECTION OF CRACK

Fig. 8.16. Predicted failure pattern for PR 7.

TABLE 8.3
MATERIAL PROPERTIES USED IN ANALYSIS OF PR 9

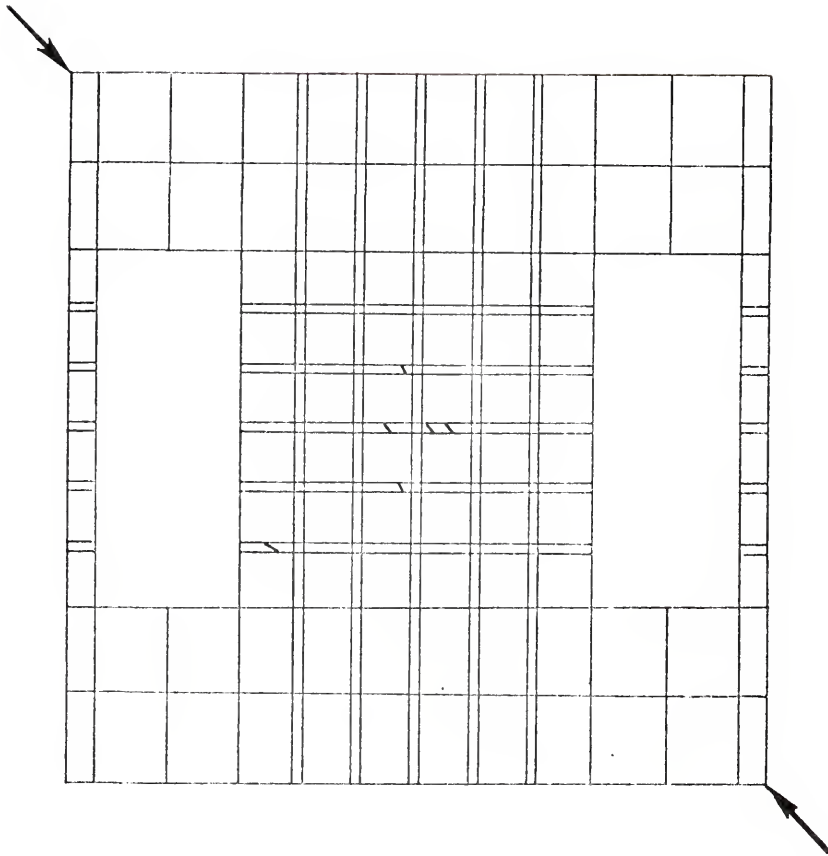
Material Code	E psi	ν	σ_o psi	σ_t psi	σ_r psi
0	1.25×10^6	0.1	485	135	33
2	1.85×10^6	0.1	450	75	
3	2.00×10^6	0.1	450	75	
4	1.32×10^6	0.1	450	75	
5	1.18×10^6	0.1	450	75	

until complete collapse occurred at 2,000 lbs. In this case, also, the predicted load was much lower than the experimental value of 3,350 lbs. The points failed in the first two iterations are shown in Figure 8.17.

The above results indicate that the assumed plane stress condition seemed to be valid only for the case where the tensile strengths of the component materials have comparable values. In all other cases, the manner in which the redistribution of the load occurs subsequent to the failure of the weaker components seems to be the influencing factor in the analysis. It is hoped that this can be taken care of in a three dimensional analysis. The analytical deflection curves indicate that the stiffness is nearly the same for all the three cases considered. Since the values of the various moduli are comparable, this seems to be valid. However, the experimental results show greater deviation for PR 7 and PR 9.

8.4.4 Nongrouted Masonry Piers: two piers, PR 6 and PR 19, were considered for analysis. PR 19 had an external pre-compression of 50 psi applied normal to bedjoints. For both the panels, an equivalent thickness of 1.073" was adopted in the analysis for the hollow portion.

PR 6 consisted of mortar joints made of weak mortar. In the analytical solution when the total load, applied in increments of 50 lbs, reached 700 lbs, complete collapse occurred. The experimental failure load was 1,100 lbs.



/ - CRACK
INCLINATION OF LINE INDICATES
DIRECTION OF CRACK

Fig. 8.17. Predicted failure pattern for PR 9.

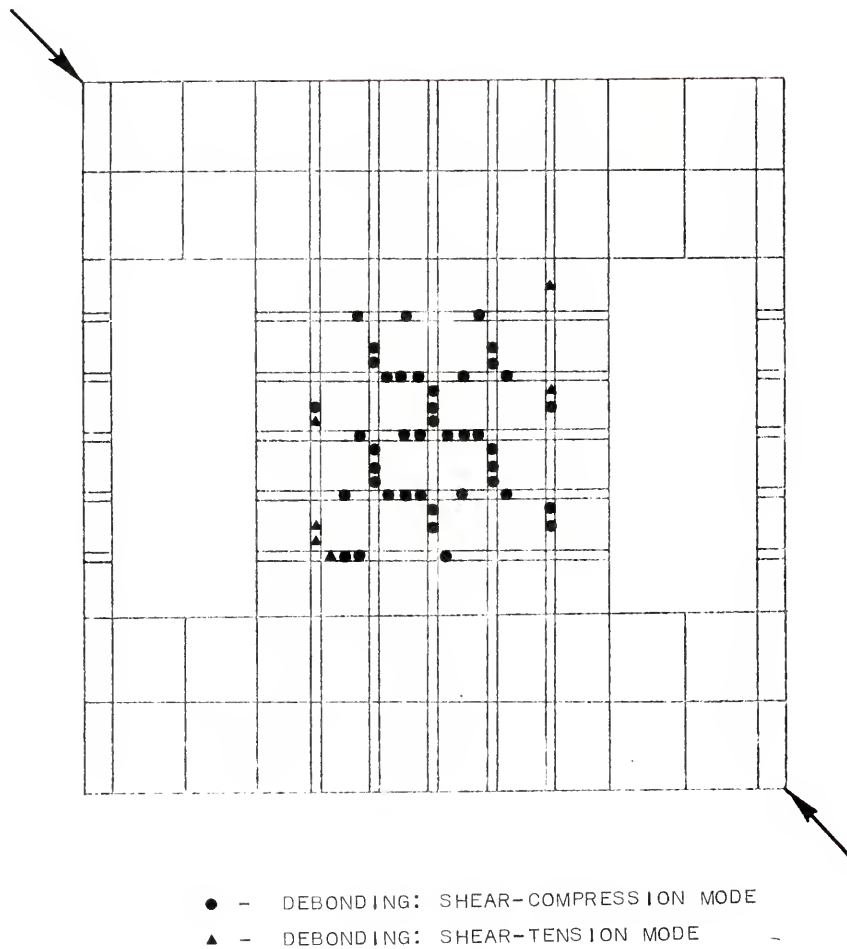


Fig. 8.18. Predicted failure pattern for PR 6.

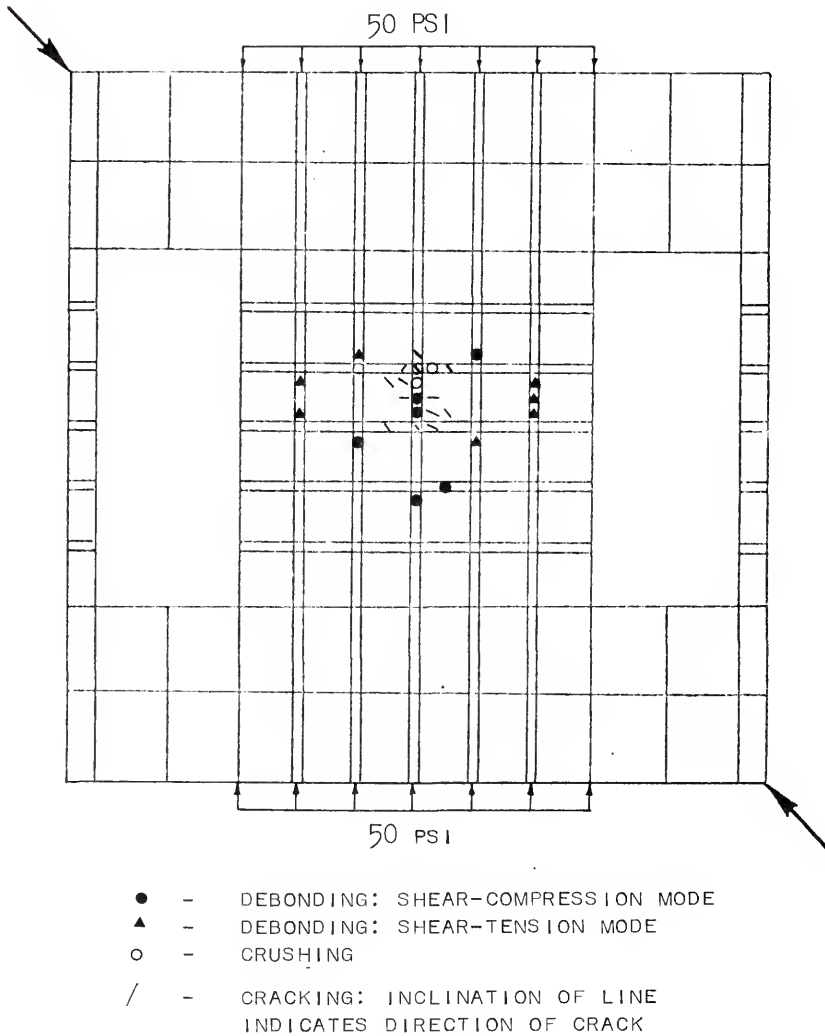


Fig. 8.19. Predicted failure pattern for PR 19.

The points failed during the first two iterations are plotted in Figure 8.18. It is evident that neither the failure load nor the failure mode was predicted correctly.

PR 19 had mortar joints made of strong mortar. An analysis of PR 19 revealed that complete collapse occurred when the load was increased from 1,350 lbs to 1,400 lbs. The experimental value for this case was 3,200 lbs. The failure points corresponding to the first two iterations are shown in Figure 8.19. In this case, also, the failure mode as well as the load was not predicted well.

It can be concluded that the debonding criterion adopted was adequate to predict the failure load correctly in the case of panels with fewer mortar joints; they seem to be inadequate in cases where the joints are subjected to bending and shear, as in the case of piers. This could be due to the confinement of the debonded regions provided by the surrounding blocks which effect could not be modelled with the present experimental data available.

CHAPTER 9

CONCLUSIONS

9.1 Conclusions: An experimental and an analytical model were developed to analyze the problem of a nonreinforced concrete masonry shear wall with openings.

It was realized that for a proper understanding of the behavior of hollow masonry walls, a knowledge of the strength of mortar joints under combined stresses was necessary. An experimental investigation was initiated to study the behavior of mortar joints under combined compression, shear, and bending. The test specimens were standard 3-block prisms with two $3/8$ " mortar joints. The test variables were mortar composition and strength. Other factors, such as suction rate, initial flow, block characteristics and curing procedures, were standardized and held constant.

Test results indicate that both shear strength and flexural tensile strength of mortar joints are appreciably increased linearly by precompression of the joints. Combined flexure and shear under precompression can be represented by a circular interaction diagram. The test data indicate that the current specifications are conservative in limiting stresses for shear and flexure-tension.

Due to limitations of space, capacity of testing machines, and cost, full-scale tests could not be made to study the shear strength of concrete masonry piers. One-fourth-scale models were used instead. The main variables considered were the grout and mortar strengths for the grouted piers; mortar strengths and magnitude of precompression were the main variables for the nongrouted piers.

The failure mode of the grouted piers under diagonal compression loading was tensile cracking along the loaded diagonal. It was found that, within the range of mortar strengths adopted, for the same type of grout used, a lower strength of mortar did not appreciably alter the failure load or mode. An equation for obtaining the diagonal tensile strength of the masonry was proposed by correlating the average shear stress across the cross-section with the square root of the corresponding prism strength. It was found that the diagonal tensile strength of the masonry was approximately equal to 3.8 times the square root of the prism strength.

In the case of hollow piers, precompression increased the shear capacity of the pier approximately linearly. A pier with weak mortar joints always failed by debonding of the mortar joints, even under high precompression. However, the introduction of stronger joints changed the failure mode to diagonal tensile cracking. Within the ranges of

strengths of mortar adopted, the mortar strength does not appreciably increase the shear capacity. It is proposed that the shear strength of a hollow pier may be predicted by calculating the failure load as the lesser of the load corresponding to the circular interaction curve or the load corresponding to the maximum principal stress equal to the tensile strength of the weaker component.

A nonlinear finite element model was chosen for the analytical investigation. An 8-node, rectangular, isoparametric element was used. Failure criteria were developed to predict the debonding of mortar joints and yielding, cracking and crushing of mortar, grout, and block.

The finite element method used was of the displacement type and was applied in an incremental form. Initial elastic analysis continued until either debonding, cracking, or plasticity occurred. The "initial stress" approach was adopted to redistribute the released stresses due to cracking to surrounding elements. The initial stiffness was used throughout each iterative cycle as well as through all the load increments. The complete structural behavior could be followed by means of nodal deflections and stresses at integration points that were printed after each load increment. The process was halted either when the specified load increments had all been applied or when the structural deterioration had become sufficiently extensive (such as when very large deflections were generated).

The validity of the program was checked by applying it to the study of a square concrete panel subjected to diagonal compression. The program predicted the maximum load within 18% of the experimentally obtained value. The application of the analytical model was then considered for concrete masonry panels and piers. The analytical model predicted the collapse loads of nongROUTED square concrete masonry panels quite closely, but not the failure patterns.

In the case of grouted piers, the analytical results were not satisfactory when the debonding of the joints was considered. The predicted loads were only 20% to 30% of the experimental values. Since the grouted element consists of two different materials, the problem is one of three-dimensional character. Also, in the model testing, no debonding failure was observed prior to diagonal cracking. Hence, it was decided to omit the debonding mode of failure while analyzing grouted piers.

The collapse load was predicted within 19% of the experimental value when the mortar and grout had comparable tensile strengths. When the difference in strengths of mortar and grout was considerable, the predicted loads were off by about 40%. It seems that the manner in which the redistribution of the load occurs subsequent to the failure of the weaker component is the influencing factor in the analysis.

The analysis did not give satisfactory results for hollow piers subjected to diagonal compression. The predicted loads were about 50% of the experimentally obtained values. Thus, it can be concluded that while the debonding criteria adopted were adequate to predict the failure load correctly in the case of panels with fewer mortar joints, they seem to be inadequate in cases where the joints are subjected to bending and shear, as in the case of piers.

9.2 Recommendations for Further Study:

- 1) The circular interaction curve proposed for predicting the strength of mortar joints under combined stresses was based on tests on two types of mortar joints under a precompression of 300 psi. More tests should be conducted with different magnitudes of precompression for various types of mortars to verify the validity of the equation over a wider range.

- 2) The entire program on tests on model piers should be repeated for different pier configurations and strengths of mortar and grout.

- 3) The analytical investigations revealed a need for more satisfactory criteria for predicting the debonding of mortar joints. Hence, it is recommended that more refined criteria should be developed for predicting the tension-shear debonding mode.

APPENDIX A
ALGORITHM FOR SOLUTION OF EQUATIONS

As described in Chapter 6, an algorithm is required to solve equations of the form:

$$[K]\{\delta\} = \{R\}$$

where $[K]$ is the symmetric positive definite global stiffness matrix, $\{\delta\}$ the unknown displacements and $\{R\}$ the right-hand side (RHS) column vector of given data.

Since in any problem there may be some known displacements, it is efficient if the knowns and unknowns are separated. In this program, the unknowns are counted column by column, while the knowns are counted and tabulated separately. The stiffness coefficients for knowns and unknowns in an element are stacked up separately.

The resulting global stiffness matrix will be banded as shown on the following page. (For simplicity, the matrix notations are not adopted for the individual matrices.)

D1	B1	C1								x1	F1
B1 ^T	D2	B2								x2	F2
C1 ^T	B2 ^T	D3	B3	C3						x3	F3
	B3 ^T	D4	B4							x4	F4
	C3 ^T	B4 ^T	D5	B5	C5					x5	F5
		B5 ^T	D6	B6						x6	F6
		C5 ^T	B6 ^T	D7	B7	C7				x7	F7
										.	.
										.	.
										.	.
										xn	Fn

where:

D1 is a square matrix of stiffness coefficients which relates the unknown displacements of first column among themselves.

B1 is a matrix of stiffness coefficients which relates the unknown displacements in column 1 with those of column 2.

C1 is a matrix of stiffness coefficients which relates the unknown displacements of column 1 with those of column 3 and so on.

x1 is the vector of unknowns in column 1...

F1 is the corresponding RHS vector for unknowns in column 1...

It is not economical to store the entire matrix [K] before solving for the unknowns. Therefore, the following

procedure is adopted:

The matrices $D1$, $B1...$ are built up for each column. Thus, when considering the first column, the block,

Column	j-1	j	j+1
	D1	B1	C1
		D2	B2
			D3

is first built up. The transposes need not be stored. However, $D3$ is only partially built up; the remainder of $D3$ is built up when considering the next column. Now triangularization can be performed for this block.

Consider the first three equations:

$$D1 \ x1 + B1 \ x2 + C1 \ x3 = F1 \quad (A.1)$$

$$B1^T \ x1 + D2 \ x2 + B2 \ x3 = F2 \quad (A.2)$$

$$C1^T \ x1 + B2^T \ x2 + D3 \ x3 + B3 \ x4 + C3 \ x5 = F3 \quad (A.3)$$

From (A.1),

$$x1 = D1^{-1}(F1 - B1 \ x2 - C1 \ x3) = D1^{-1} \ F1^*$$

Substituting for x_1 in (A.2),

$$(D_2 - B_1^T D_1^{-1} B_1) x_2 + (B_2 - B_1^T D_1^{-1} C_1) x_3 = (F_2 - B_1^T D_1^{-1} F_1)$$

or,

$$D_2^* x_2 + B_2^* x_3 = F_2^*$$

$$x_2 = (D_2^*)^{-1} (F_2^* - B_2^* x_3)$$

Substituting for x_1 in (A.3),

$$(B_2^T - C_1^T D_1^{-1} B_1) x_2 + (D_3 - C_1^T D_1^{-1} C_1) x_3 + B_3 x_4 + C_3 x_5 = (F_3 - C_1^T D_1^{-1} F_1)$$

or,

$$(B_2^*)^T x_2 + D_3^* x_3 + B_3 x_4 + C_3 x_5 = F_3^*$$

Substituting for x_2 in the above,

$$(D_3^* - B_2^{*T} D_2^{-1} B_2) x_3 + B_3 x_4 + C_3 x_5 = F_3^*$$

or,

$$D3^{**} x3 + B3 x4 + C3 x5 = F3^{**} \quad (A.4)$$

In the preceding equations, the ()^{*} and ()^{**} matrices are defined implicitly in terms of the corresponding () matrices and are typically overstored in the same core locations.

Equation (A.4) can be used to eliminate x3 from the next two equations, and so on until the last equation is of the form,

$$Dn x_n = F_n$$

from which x_n is obtained. Back substitution yields the other unknowns.

The algorithm described above was originally developed by Eisenberg and Kim.[†]

[†] Eisenberg, M. A. and Kim, B. S., "Numerical Analysis of Plane Elastic-Plastic Boundary Value Problems: Theory and Application to Single Crystal Beam," University of Florida, Engineering and Industrial Experiment Station Technical Report No. 5, ONR Contract No. N0014-68-A-0173-0002, December, 1970.

APPENDIX B
COMPUTER PROGRAM OUTPUT

The example chosen is the square panel subjected to diagonal compression. The material properties and loading conditions have already been described in Chapter 8.

Figure B.1 shows the finite element idealization of the panel. The computer program output for the above problem are given in the following pages. The input data and results of the last load increment only are given. To facilitate understanding the printout, the following notes are given.

In Figure B.1, the secondary rows and columns are shown in dotted lines. The topological codes for the primary nodes are also marked in the figure. The primary nodes define an element. The secondary nodes are the midside nodes. The integration points chosen are shown in Figure 8.10. 'DELTA' denotes the shear-retention factor. The boundary conditions are: 1) at the loaded point the displacement in the x-direction is zero; 2) at the support the displacements in the x- and y- directions are zero. NFL is the matrix indicating the failure modes at the integration points. 'Two (2)' denotes cracking, '3', debonding (shear-compression), '4',

debonding (shear-tension), and '100', crushing. Matrix NFL was initialized at the start of the analysis. 'TV' denotes the vertical displacement of the loaded point. Since the arrays TU and TV were not initialized, their values beyond stage 5 are not valid.

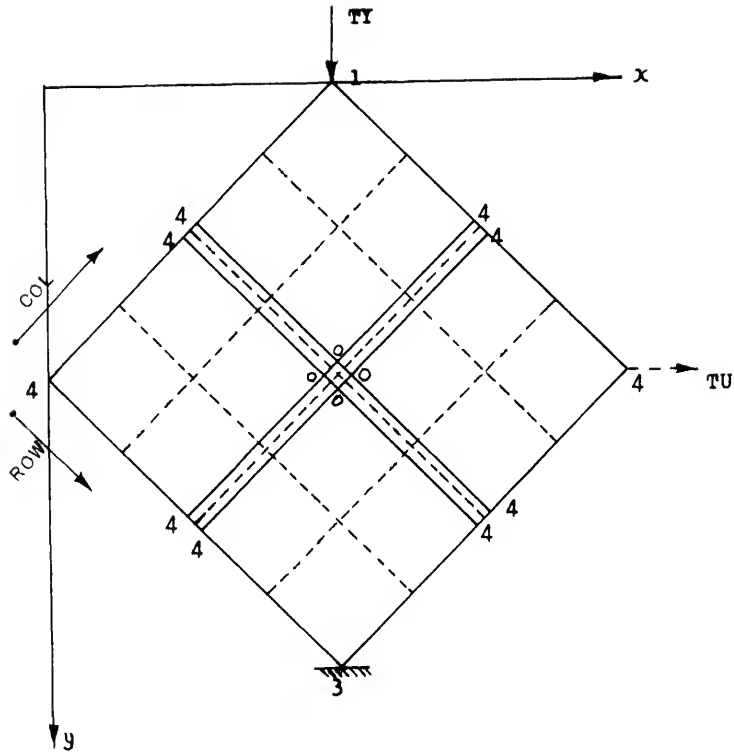


Fig. B.1. Finite element idealization for panel SM.

PLANE STRESS FINITE ELEMENT ANALYSIS

PRIMARY POINTS = A PRIMARY COLUMNS = 4
 PLAS POINTS = 1 C TOTAL COLUMNS = 7
 TOTAL POINTS = 7

PRIMARY TOPOLOGY MATRIX

4 4 4 1
 4 0 0 4
 4 0 0 4
 3 4 4 4

MATRIX NTYPE

3 X 3 GAUSS POINTS = 0
 1 X 3 GAUSS POINTS = 1
 3 X 1 GAUSS POINTS = 2
 SINGLE GAUSS POINT = 3

0 2 0
 1 2 0
 0 2 0

MATRIX MTYPE:

CONCRETE BLOCK = 0
 MORTAR = 1
 STEEL = 3

0 1 0
 1 1 1
 0 0 0

THICKNESS OF ALL ELEMENTS: 1.073000

MIN OF JOINTS TO ML. -45.0000
 MIN OF JOINTS TO ML. 0.0000
 COEFF OF FRICTION 0.6400
 COMPRESSION FORCE REQUIRED TO CONTINUE ITERATION 20.0000
 MIN TOTAL FORCE REQUIRED TO CONTINUE ITERATION 20.0000

F BLOCK 2400000.
 EPOUT 0.
 EPOUT 0.
 EPOUT 0.
 EPOUT 1500000.
 TENSILE STR MORTAR 200.
 TENSILE STR GROUP 0.
 TENSILE STR BLOCK 260.
 STEEL 0.

NO OF PTS OF APPLICATION OF CONC LOAD 1
 MAX NO OF LOAD INCREMENTS: 12
 MAX NO OF ITERATIONS 3

EXPANDED TOPOLOGY MATRIX

INTERNAL POINT
 U GIVEN
 V GIVEN
 U AND V GIVEN
 ONLY T-RAXIONS GIVEN
 EXTERIOR POINT
 INTERIOR NODE VACANCY

444441
 444441
 400004
 400004
 426004
 426004
 450004
 450004
 344444

= 0
 = 1
 = 1
 = 3
 = 4
 = 1
 = 0

X-COORDINATES:

PCW 1	0.0	1.32583	1.37002	1.41421	2.07712	2.74004
PCW 2	0.66291	1.32583	2.03293	2.07712	2.74004	3.40295
PCW 3	1.32583	1.98874	2.65594	2.74004	3.40295	4.06586
PCW 4	1.37002	2.65165	2.74004	2.78423	3.44714	4.11005
PCW 5	1.41421	2.65584	2.78423	2.82842	3.49134	4.15425
PCW 6	2.07712	2.74004	3.44714	3.49134	4.15425	4.61716
PCW 7	2.74004	3.40295	4.11005	4.15425	4.61716	5.48007

Y-COORDINATES:

PCW 1	2.74004	2.07713	1.41421	1.32583	0.66291	-0.00000
PCW 2	3.40295	2.74004	2.07713	1.98874	1.32583	0.66291
PCW 3	4.06587	3.40295	2.74004	2.65165	1.98874	1.32583
PCW 4	4.11006	3.44715	2.78423	2.69584	2.03293	1.37002
PCW 5	4.15425	3.49134	2.82843	2.74004	2.07712	1.41421
PCW 6	4.61716	4.15425	3.49134	3.40295	2.74004	2.07712
PCW 7	5.48008	4.61716	4.15425	4.06586	3.40295	2.74004

IU = GLOBAL ADDRESS OF HORIZONTAL DISPLACEMENT

1	13	21	35	43	57	-3
3	0	40	0	46	0	66
5	15	25	37	47	50	68
7	10	27	30	49	0	70
11	10	31	30	53	60	74
-1	10	33	41	55	63	76

IV = GLOBAL ADDRESS OF VERTICAL DISPLACEMENT

2	14	22	30	44	58	65
4	10	26	38	48	60	69
6	10	28	0	50	0	71
10	18	30	40	52	62	73
12	0	32	42	54	64	75
-2	20	34	42	56	64	77

LOAD INCREMENT NO. 1

BEGINNING OF ITERATION NO: 1

DISPLACEMENT BOUNDARY CONDITIONS

FLAG	KROW	KCOL	N	1PI	1CI	UU	UI	VV	VI
1	1	7	1	0	0	0.0	0.0	0.0	0.0
3	1	7	1	0	0	0.0	0.0	0.0	0.0

TOTAL LOAD AT POINT(1, 7): STAGE-- 1 TX: 0.0 TY: 270.00

LOAD INCREMENT NO. 2

BEGINNING OF ITERATION NO: 1

TOTAL LOAD AT POINT(1, 7): STAGE-- 5 TX: 0.0 TY: 200.00

POINT(4, 3): DEFORMING SHEAR-COMP NO. OF POINTS FAILED SO FAR: 1

BEGINNING OF ITERATION NO: 2

BEGINNING OF ITERATION NO: 3

POINT(1, 1) CRACKED AT 0.10306E 03 DEG NO OF POINTS FAILED SO FAR: 2

POINT(2, 1) CRACKED AT 0.11153E 02 DEG NO OF POINTS FAILED SO FAR: 3

POINT(3, 1) CRACKED AT 0.20943E 02 DEG NO OF POINTS FAILED SO FAR: 4

POINT(3, 2) CRACKED AT 0.42543E 02 DEG NO OF POINTS FAILED SO FAR: 5

POINT(2, 3) CRACKED AT 0.12242E 02 DEG NO OF POINTS FAILED SO FAR: 6

POINT(3, 3) CRACKED AT 0.72100E 02 DEG NO OF POINTS FAILED SO FAR: 7

GAUSS POINT(4, 1) FAILED BY CRUSHING NO. OF POINTS FAILED SO FAR: 8

GAUSS POINT(4, 2) FAILED BY CRUSHING NO. OF POINTS FAILED SO FAR: 9

```

MAX COMP STRAIN AT 4 3 0.01141
GAUSS POINT( 4, 3) FAILED BY CRUSHING
POINT( 5, 1) CRACKED AT 0.593315 02 DEG
NO OF POINTS FAILED SO FAR: 10
POINT( 5, 1) CRACKED AT 0.480606 02 DEG
NO OF POINTS FAILED SO FAR: 11
POINT( 5, 1) CRACKED AT 0.525795 02 DEG
NO OF POINTS FAILED SO FAR: 12
POINT( 5, 1) CRACKED AT 0.252375 02 DEG
NO OF POINTS FAILED SO FAR: 13
POINT( 7, 3) CRACKED AT 0.531375 02 DEG
NO OF POINTS FAILED SO FAR: 14
POINT( 2, 4) CRACKED AT 0.502175 02 DEG
NO OF POINTS FAILED SO FAR: 15
POINT( 3, 4) CRACKED AT 0.518115 01 DEG
NO OF POINTS FAILED SO FAR: 16

GAUSS POINT( 4, 4) FAILED BY CRUSHING
NO OF POINTS FAILED SO FAR: 17
POINT( 5, 4) CRACKED AT 0.558705 02 DEG
NO OF POINTS FAILED SO FAR: 18
POINT( 6, 4) CRACKED AT 0.576145 02 DEG
NO OF POINTS FAILED SO FAR: 19
GAUSS POINT( 4, 5) FAILED BY CRUSHING
NO OF POINTS FAILED SO FAR: 20
POINT( 4, 4) CRACKED AT 0.126415 03 DEG
NO OF POINTS FAILED SO FAR: 21
POINT( 4, 7) DEBONDING: SHEAR-TENSION
NO OF POINTS FAILED SO FAR: 22
POINT( 5, 7) CRACKED AT 0.141285 03 DEG
NO OF POINTS FAILED SO FAR: 23

```

NO OF ITERATIONS: 3

MATRIX NFL: LOAD INCREMENT: 5

ROW 1	2	0	0	0	0	0
ROW 2	2	0	2	0	0	0
ROW 3	2	2	2	0	0	0
ROW 4	100	100	100	100	2	4
ROW 5	2	2	2	0	0	2
ROW 6	2	0	0	2	0	0
ROW 7	0	0	2	0	0	0

MATRIX PRX: LOAD INCREMENT: 5

ROW 1	-4097.19	-3481.64	-4417.24	-459.03	5887.55	0.0	0.0
ROW 2	-8910.01	0.0	-9311.56	0.0	18121.48	0.0	0.0
ROW 3	240882.69	749464.56	322619.75	149877.75	100165.56	206178.75	72940.25
ROW 4	-17618.04	0.0	78933.50	0.0	-73512.88	0.0	12747.78
ROW 5	-259027.38	-750032.91	-278459.44	-150257.38	-136062.56	-206769.38	-64677.05
ROW 6	-9023.27	0.0	-13617.17	0.0	22549.19	0.0	91.06
ROW 7	0.0	4020.08	-2918.79	840.63	7993.42	590.46	227.19

MATRIX RVF: LOAD INCREMENT: 5

ROW 1	1776.12	-3851.87	8626.46	-1982.11	-14318.93	0.0	0.0
ROW 2	9220.16	0.0	31754.10	0.0	-40974.38	0.0	0.0
ROW 3	331274.06	982671.00	367455.00	182717.38	196688.44	224792.13	71086.63
ROW 4	2483.11	0.0	-94242.88	0.0	103744.88	0.0	-11420.46
ROW 5	-323041.19	-980939.19	-415837.63	-181170.94	-106495.44	-225496.44	-79078.19
ROW 6	7163.06	0.0	9410.89	0.0	-16369.16	0.0	-204.89
ROW 7	0.0	2159.57	4002.35	436.05	-5076.25	704.27	166.47

NSTAGE

TU

TV

1	0.18645E-03	0.47517E-03
2	0.18990E-03	0.48297E-03
3	0.18761E-03	0.48157E-03
4	0.18761E-03	0.48157E-03
5	0.18761E-03	0.48157E-03
6	0.18761E-03	0.48157E-03
7	0.18761E-03	0.48157E-03
8	0.18761E-03	0.48157E-03
9	0.18761E-03	0.48157E-03
10	0.18761E-03	0.48157E-03
11	0.18761E-03	0.48157E-03

REFERENCES

1. ACI Committee 442, "Response of Buildings to Lateral Forces," Journal of the American Concrete Institute, Vol. 18, Feb., 1971, pp. 81-106.
2. ACI Committee 531, "Concrete Masonry Structures - Design and Construction," Journal of the American Concrete Institute, Vol. 67, May, 1970, pp. 380-403; and June, 1970, pp. 442-460.
3. ASCE-ACI Task Committee 426, "The Shear Strength of Reinforced Concrete Members," Journal of the Structural Division, ASCE, Vol. 99, No. ST 6, Proc. Paper 9791, June, 1973, pp. 1091-1187.
4. BASE, G. D., "Shearing Tests on Thin Epoxy-resin Joints between Precast Concrete Units," Concrete and Constructional Engineering, London, Vol. LVIII, No. 7, July, 1963, pp. 273-277.
5. BENJAMIN, J. R. and WILLIAMS, H. A., "The Behavior of One-Story Brick Shear Walls," Journal of the Structural Division, ASCE, Vol. 84, No. ST4, Proc. Paper 1723, July, 1958, pp. 1723-1-1723-30.
6. BLUME, J. A. and PROULX, J., Shear in Grouted Brick Masonry Wall Elements, Western Clay Products Association, San Francisco, California, August, 1968.
7. BUYUKOZTURK, O., NILSON, A. H. and SLATE, F. O., "Stress-Strain Response and Fracture of a Model of Concrete in Biaxial Loading," Journal of the American Concrete Institute, Vol. 68, Aug., 1971, pp. 590-599.
8. BUYUKOZTURK, O. and NILSON, A. H., "Finite Element Analysis of a Model of Plain Concrete with Biaxial Loads," Proceedings of the Specialty Conference on Finite Element Method in Civil Engineering, Mc Gill University, Montreal, Canada, June, 1972, pp. 703-728.
9. CARPENTER, J. E., ROLL, F. and ZELMAN, M. I., "Techniques and Materials for Structural Models," Symposium on Models for Concrete Structures, Special Publication 24, American Concrete Institute, Detroit, 1970, pp. 41-63.

References (Continued)

10. CERVENKA, V. and GERSTLE, K. H., "Inelastic Analysis of Reinforced Concrete Panels: Theory," International Association of Bridge and Structural Engineering Publications, Vol. 31-II, 1971, pp. 31-45; and Vol. 32-II, 1972, pp. 25-39.
11. CHOU, P. C. and PAGANO, N. J., Elasticity, D. Van Nostrand Company, Inc., 1967.
12. CONVERSE, F. J., "A Report to the Pacific Coast Building Officials Conference on Tests on Reinforced Concrete Masonry," Building Standards Monthly, Feb., 1946.
13. COPELAND, R. E. and SAXER, E. L., "Tests of Structural Bond of Masonry Mortars to Concrete Block," Journal of the American Concrete Institute, Vol. 61, Nov., 1964, pp. 1411-1452.
14. COULL, A. and SMITH, B. S., "Analysis of Shear Wall Structures," Tall Buildings, Pergamon Press, 1967, pp. 139-155.
15. DESAI, C. S. and ABEL, J. F., Introduction to the Finite Element Method, Van Nostrand Reinhold Company, New York, 1972.
16. DICKEY, W. L. and HARRINGTON, R. W., The Shear Truth about Brick Walls, Western States Clay Products Association, Inc., 1970.
17. FELIPPA, C., "Refined Finite Element Analysis of Linear and Nonlinear Two Dimensional Structures," Ph. D. Dissertation, Dept. of Civil Engineering, University of California, Berkeley, 1966.
18. FISHBURN, C., "Effect of Mortar Properties on Strength of Masonry," Monograph 36, National Bureau of Standards, 1961.
19. FRANKLIN, H. A., "Nonlinear Analysis of Reinforced Concrete Frames and Panels," Ph. D. Dissertation, Dept. of Civil Engineering, University of California, Berkeley, 1970.
20. GENSERT, R. M. and BRETNALL, W. C., "Practical Design of Masonry Buildings," Planning and Design of Tall Buildings, Proceedings, International Conference on Planning and Design of Tall Buildings, Lehigh University, Bethlehem, Pa., Vol. III, pp. 1069-1085.

References (Continued)

21. GIRIJAVALLABHAN, C. V., "Analysis of Shear Walls by Finite Element Method," Proc. of the Symposium on Application of Finite Element Method in Civil Engineering, ASCE, 1969, pp. 631-641.
22. HALLER, P., "Load Capacity of Brick Masonry," Designing, Engineering and Constructing with Masonry Products, Gulf Publishing Company, 1969, pp. 129-149.
23. HAND, F. R., PECKNOLD, D. A. and SCHNOBRICH, W. C., "Nonlinear Layered Analysis of RC Plates and Shells," Journal of the Structural Division, ASCE, Vol. 99, No. ST7, Proc. Paper 9860, July, 1973, pp. 1491-1505.
24. HEDSTROM, R. O., "Load Tests of Patterned Concrete Masonry Walls," Journal of the American Concrete Institute, Vol. 57, April, 1961, pp. 1265-1286.
25. HILSDORF, H. K., "Masonry Materials and Their Physical Properties," Planning and Design of Tall Buildings, Proceedings, International Conference on Planning and Design of Tall Buildings, Lehigh University, Bethlehem, Pa., Vol. III, pp. 981-999.
26. JANNEY, J. R., BREEN, J. E., GREYMAYER, H., LOCKMAN, T. W. and ROCHA, M. "The Use of Models in Structural Engineering," Symposium on Models for Concrete Structures, Special Publication 24, American Concrete Institute, Detroit, 1970, pp. 1-18.
27. JOHNSON, F. B. and MATTHYS, J. H., "Structural Strength of Hollow Clay Tile Assemblages," Journal of the Structural Division, ASCE, Vol. 99, No. ST2, Proc. Paper 9577, February, 1973, pp. 259-275.
28. JOHNSON, F. B. and THOMPSON, J. N., "Development of Diametral Testing Procedures to Provide a Measure of Strength Characteristics of Masonry Assemblages," Designing, Engineering and Constructing with Masonry Products, Gulf Publishing Company, 1969, pp. 51-57.
29. KHAN, F. R., "On Some Special Problems of Analysis and Design of Shear Wall Structures," Tall Buildings, Pergamon Press, 1967, pp. 321-344.
30. KOKINOPOULOS, E., "Experimental Photoelastic Determination of the Stresses and Deformations of Laterally Loaded Shear Walls with Openings," Tall Buildings, Pergamon Press, 1967, pp. 547-563.

References (Continued)

31. KUPFER, H. B., HILSDORF, H. K., and RUSCH, H., "Behavior of Concrete Under Biaxial Stresses," Journal of the American Concrete Institute, Vol. 66, August, 1969, pp. 656-666.
32. KUPFER, H. B., and GERSTLE, K. H., "Behavior of Concrete Under Biaxial Stresses," Journal of the Engineering Mechanics Division, ASCE, Vol. 99, No. EM4, August, 1973, pp. 853-866.
33. LIU, T. C. Y., "Stress-Strain REsponse and Fracture of Concrete in Biaxial Compression," Ph. D. Dissertation, Department of Civil Engineering, Cornell University, Ithaca, N. Y., 1971.
34. LIU, T. C. Y., NILSON, A. H., and SLATE, F. O., "Stress-Strain Response and Fracture of Concrete in Uniaxial and Biaxial Compression," Journal of the American Concrete Institute, Vol. 69, May, 1972, pp. 291-295.
35. LIU, T. C. Y., NILSON, A. H., and SLATE, F. O., "Biaxial Stress-Strain Relations for Concrete," Journal of the Structural Division, ASCE, Vol. 98, No. ST5, Proc. Paper 8905, May, 1972, pp. 1025-1034.
36. MALLET, R. J., "Structural Behavior of Masonry Elements," Planning and Design of Tall Buildings, Proceedings, International Conference on Planning and Design of Tall Buildings, Lehigh University, Bethlehem, Pa., August, 1972, pp. 1001-1034.
37. MARCAL, P. V., "Finite Element Analysis with Material Nonlinearities-Theory and Practice," Proceedings of the Specialty Conference on Finite Element Method in Civil Engineering, Mc Gill University, Montreal, Canada, June, 1972, pp. 35-70.
38. MATTOCK, A. H., "Structural Model Testing-Theory and Applications," Development Department Bulletin D-56, Portland Cement Association, Skokie, Illinois, Sept., 1962.
39. MELI, R. P., and REYES, A. G., "Propiedades Mecanicas de la Mamposteria," Instituto de Ingenieria, Informe No. 288, Universidad Nacional Autonoma de Mexico, July, 1971.

References (Continued)

40. MIRZA, S. M., WHITE, R. N., and ROLL, F., "Materials for Structural Models," Preprints of the Symposium on Models for Concrete Structures, The Annual Convention of the American Concrete Institute, Dallas, Texas, March, 1972, pp. 19-112.
41. National Concrete Masonry Association, "Load-Bearing Block in High Rise Buildings," NCMA TEK 7a, National Concrete Masonry Association, Arlington, Va., 1968.
42. POLYAKOV, S. V., "Some Investigations of the Problem of the Strength of Elements of Buildings Subjected to Horizontal Loads," Tall Buildings, Pergamon Press, 1967, pp. 465-479.
43. RICHART, F. E., MOORMAN, R. R., and WOODWORTH, P. M., "Strength and Stability of Concrete Masonry Walls," Engineering Experiment Station Bulletin No. 251, University of Illinois, July, 1932.
44. SAHLIN, S., Structural Masonry, Prentice-Hall, Inc., Englewood Cliffs, New Jersey, 1971.
45. SCHNEIDER, R. R., "Summary Reports of Lateral Load Tests on Reinforced Grouted Masonry Shear Walls," University of Southern California Engineering Center, Report No. 70-101, 1959, pp. 1-47.
46. SCHNEIDER, R. R., Shear in Concrete Masonry Piers, Masonry Research of Los Angeles, Los Angeles, California.
47. SCORDELIS, A. C., "Finite Element Analysis of Reinforced Concrete Structures," Proceedings of the Specialty Conference on Finite Element Method in Civil Engineering, June, 1972, Mc Gill University, Montreal, Canada, pp. 71-103.
48. SCRIVENER, J. C., "Static Racking Tests on Concrete Masonry Walls," Designing, Engineering and Constructing with Masonry Products, Gulf Publishing Company, 1969, pp. 185-191.
49. SELF, M. W., "The Structural Properties of Load-Bearing Concrete Masonry," Research Report, EIES Project D-622, Engineering and Industrial Experiment Station, University of Florida, March, 1974, pp. 45-48.

References (Continued)

50. SINHA, B. P., and HENDRY, A. W., "Racking Tests on Storey Height Shear Wall Structures with Openings Subjected to Precompression," Designing, Engineering and Constructing with Masonry Products, Gulf Publishing Company, 1969, pp. 192-199.
51. SMITH, B. S., CARTER, C., and CHOUDHURY, J. R., "The Diagonal Tensile Strength of Brickwork," The Structural Engineer, London, Vol. 48, June, 1970, pp. 219-225.
52. SUIDAN, M., and SCHNOBRICH, W. C., "Finite Element Analysis of Reinforced Concrete," Journal of the Structural Division, ASCE, Vol. 99, No. ST10, Proc. Paper 10081, October, 1973, pp. 2109-2122.
53. YUZUGULLU, O., and SCHNOBRICH, W. C., "A Numerical Procedure for the Determination of the Behavior of a Shear Wall-Frame System," Journal of the American Concrete Institute, Vol. 70, July, 1973, pp. 474-479.
54. ZIA, P., WHITE, R. N., and VAN HORN, D. A., "Principles of Model Analysis," Symposium on Models for Concrete Structures, Special Publication 24, American Concrete Institute, Detroit, 1970, pp. 19-39.
55. ZIENKIEWICZ, O. C., The Finite Element Method in Engineering Science, McGraw-Hill Publishing Company Limited, London, 1971.
56. ZIENKIEWICZ, O. C., and IRONS, B. M., "Isoparametric Elements," Finite Element Techniques in Structural Mechanics, Southampton University Press, 1970, pp. 283-298.
57. ZIENKIEWICZ, O. C., VALLIAPPAN, S., and KING, I. P., "Elasto-plastic Solutions of Engineering Problems - Initial Stress Finite Element Method," International Journal of Numerical Methods in Engineering, Vol. 1 No. 1, Jan.-Mar., 1969, pp. 75-100.

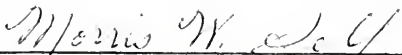
BIOGRAPHICAL SKETCH

Krishnaiyer Balachandran was born on February 9, 1942, in Thanjavur, Tamilnadu, India. He graduated from Kalyanasundaram High School at Thanjavur, in 1956. After completing his pre-university course at the Rajah Serfoji College, Thanjavur, in 1958, he joined the A. C. College of Engineering, University of Madras, Karaikudi, Tamilnadu, India. In 1963, he received the degree of Bachelor of Engineering with a major in Civil Engineering. From June, 1963, to August, 1965, he was employed as a Junior Engineer in the Marine Works Circle of the Public Works Department of the Government of Madras. In August, 1965, he joined the Indian Institute of Science, Bangalore, India, for his graduate studies and received the degree of Master of Engineering with a major in Structural Engineering. In August, 1967, he joined the faculty of Civil Engineering at the PSG College of Technology, University of Madras, Coimbatore, Tamilnadu, India. Till March, 1970, he taught Theory of Structures for undergraduates and Advanced Strength of Materials and Experimental Stress Analysis for first year graduate students.

In the Spring of 1970 he came to the U. S. A., and until the present time he has pursued his doctoral studies at the University of Florida.

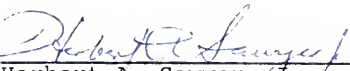
K. Balachandran is married to the former Lalitha Krishnaswamy and they have a one-year-old daughter, Priya. He is a member of the American Concrete Institute.

I certify that I have read this study and that in my opinion it conforms to acceptable standards of scholarly presentation and is fully adequate, in scope and quality, as a dissertation for the degree of Doctor of Philosophy.




Morris W. Self, Chairman
Professor of Civil Engineering

I certify that I have read this study and that in my opinion it conforms to acceptable standards of scholarly presentation and is fully adequate, in scope and quality, as a dissertation for the degree of Doctor of Philosophy.



Herbert A. Sawyer, Jr.
Professor of Civil Engineering


I certify that I have read this study and that in my opinion it conforms to acceptable standards of scholarly presentation and is fully adequate, in scope and quality, as a dissertation for the degree of Doctor of Philosophy.



C. S. Hartley
Associate Professor
Materials Science Engineering

This dissertation was submitted to the Graduate Faculty of the College of Engineering and to the Graduate Council, and was accepted as partial fulfillment of the requirements for the degree of Doctor of Philosophy.

August, 1974



Dean, College of Engineering

Dean, Graduate School



UNIVERSITY OF FLORIDA



3 1262 08666 210 2